

**STUDY OF LIGHT WEIGHT, HIGH STRENGTH, MULTIFUNCTIONAL COMPOSITE
MATERIAL: ALUMINUM REINFORCED WITH AIB₂ PARTICLES**

By

Ulises Barajas Valdes

Dissertation submitted in partial fulfillment of the requirements for the degree of

**DOCTOR OF PHILOSOPHY
IN
CIVIL ENGINEERING**

UNIVERSITY OF PUERTO RICO
MAYAGÜEZ CAMPUS
2017

Approved by:

Luis E. Suárez Colche, Ph.D.
Member, Graduate Committee

Date

Ricardo R. López Rodríguez, Ph.D.
Member, Graduate Committee

Date

Genock Portela, Ph.D.
Member, Graduate Committee

Date

O. Marcelo Suárez, Ph.D.
President, Graduate Committee

Date

Rafael A. Rodríguez Solís, Ph.D.
Representative, Graduate Studies

Date

Ismael Pagán Trinidad, MSCE
Chairperson, Department of Civil Engineering
and Surveying

Date

Copyright © by
ULISES BARAJAS VALDES
2017

Dedicated to:

God, thanks to him I came here finish with a doctorate's degree.

My wife Amáralis Zoé and daughter Erin Zoé, who support me with their love, patience and encouragement... I love them!!!

My parents, Hernando and Alix María, they made who I am.

And my brothers Janet, Hernando, Sandra Milena and Ildemar... they always be there...

ABSTRACT

Aluminum, its alloys and composites are widely used in many modern life applications, such as microelectromechanical systems. In this research, an aluminum matrix composite reinforced with AlB_2 particles was studied in bulk and in thin films. Bulk samples were manufactured by centrifugal casting the composite with different levels of boron forming AlB_2 particles. The effect of embedded particles on the aluminum matrix was evaluated using Brinell hardness and nanoindentation. Brinell hardness increased from 250 MPa to 450 MPa as a result of particle content. The nanoindentation technique showed that the mechanical improvement is a result of the combined action between the two phases present. Thin films were made from pure aluminum and the Al-4wt. %B (Al-4B) composite using sputtering magnetron by radio frequency at different discharge power on glass substrates and silicon wafers (100). Nanoindentation revealed a higher modulus of elasticity, hardness and adhesion in the Al-4B films. The surface morphology of the films was studied using atomic force microscopy. The surface of the aluminum films presented a greater roughness and grain size with respect to the composite films. Additionally, in composite films the hillock formation was significantly reduced. The structural evaluation of the material via x-ray diffraction exposed in the aluminum samples a larger lattice strain. In addition, temperature effects were studied in samples deposited at 200 watts of sputtering power via hot stage tests using nanoindentation and x-ray diffraction. The materials exhibited softening by heating effect that expands the structure reducing mechanical properties. Additionally, the samples presented material annealing as result of the temperature cycle used in the tests. This was reflected in the mechanical behavior and the crystal structure.

RESUMEN

El aluminio, sus aleaciones y compuestos son extensamente utilizados en muchas aplicaciones de la vida moderna, como los sistemas micro-electromecánicos. En esta investigación, un compuesto de matriz de aluminio reforzado con partículas de AlB_2 fue estudiado a granel y en películas delgadas. Las muestras a granel fueron fabricadas por medio de fundición centrífuga para diferentes niveles de boro formando partículas de AlB_2 . El efecto de las partículas en la matriz de aluminio fue evaluado usando la dureza Brinell y nanoindentación. La dureza Brinell aumento de 250 MPa a 450 MPa como resultado del contenido de partículas. La técnica de nanoindentación demostró que el mejoramiento mecánico fue resultado de la acción combinada entre las dos fases presentes. Las películas delgadas fueron fabricadas con aluminio puro y el compuesto Al-4wt %B (Al-4B) vía pulverización catódica con magnetos usando radio frecuencia a diferentes potencias de descarga sobre sustratos de vidrio y obleas de silicio (100). La nanoindentación reveló un mayor módulo de elasticidad, dureza y adhesión en las películas de Al-4B. La morfología de la superficie de las películas fue estudiada usando un microscopio de fuerza atómica. La superficie de las películas de aluminio presentó una mayor rugosidad y tamaño de grano con respecto a las películas compuestas. Adicionalmente, en las películas compuestas la formación de montículos se redujo significativamente. La evaluación estructural del material por medio de la difracción por rayos X expuso en las muestras de aluminio mayor deformación estructural del material. También, los efectos de temperatura fueron estudiados en las muestras depositadas a 200 watts de potencia de pulverización a partir de ensayos en fase caliente usando nanoindentación y difracción de rayos X. Los materiales

exhibieron ablandamiento por efecto del calor que expande la estructura del cristal reduciendo las propiedades mecánicas. Adicionalmente, el material de las muestras presentó recocido por el ciclo de temperatura usado en las pruebas, lo cual se vio reflejado en el comportamiento mecánico y en la deformación de la estructura del material.

ACKNOWLEDGEMENTS

First of all, I would like to sincerely thank Professor O. Marcelo Suárez by the confidence given to carrying out this research, for his advice, support, and knowledge... Now it has become a reality. I would also like to thank the members of the postgraduate committee, Dr. Ricardo López Rodríguez, Dr. Genock Portela, Dr. Luis E. Suárez and Dr. Rafael Rodríguez Solís.

I am grateful to Professor Arturo Hernández who provided us access to his XRD laboratory and to his graduate student Rodinsón R. Arrieta Pérez of the Department of Chemical Engineering.

The author would also like to thank the invaluable assistance of the technical personnel of the University of Puerto Rico-Mayagüez Materials Laboratories: Boris Rentería and Carlos Rivera and administrative staff Myriam Padilla, Adelaida Rivera, and Norma Gómez. To our research group (les inútiles) I am in debt for their support and collaboration upon this joint task.

Finally, I want to thank the National Science Foundation under grants N° 0619349 and 0922994 (MRI Program), and 0833112 and 1345156 (CREST Program) and, to Departments of Civil Engineering and surveying and General Engineering of University of Puerto Rico. These entities in one way or another financially supported to this research work.

CONTENTS

| | |
|--|------|
| ABSTRACT | ii |
| RESUMEN | v |
| ACKNOWLEDGEMENTS | vii |
| CONTENTS | viii |
| FIGURES | x |
| TABLES | xiv |
| ABBREVIATIONS | xv |
| SYMBOLS | xvi |
| 1 INTRODUCTION | 1 |
| 1.1 Literature Review | 1 |
| 1.1.1 Functionally Graded Materials (FGMs) | 1 |
| 1.1.2 Mechanical Properties Studies via Nanoindentation in FGMs | 4 |
| 1.1.3 Thin Films Studies | 5 |
| 1.1.4 Ancillary Research with Further Discussion of Pertinent Literature | 7 |
| 1.1.5 Aluminum Thin Film Issues | 8 |
| 2 OBJECTIVES | 12 |
| 2.1 General Objective | 12 |
| 2.2 Specific Objectives | 12 |
| 3 THEORETICAL BACKGROUND | 14 |
| 3.1 Metal Matrix Composites | 14 |
| 3.1.1 Aluminum Matrix Composite (AMC) | 14 |
| 3.2 Thin Films Coating | 16 |
| 3.2.1 General Sputtering Process | 16 |
| 3.2.2 Magnetron Sputtering | 18 |
| 3.3 Material Characterization | 18 |
| 3.3.1 Mechanical Properties | 18 |
| 3.3.2 Structural Evaluation | 30 |
| 4 EXPERIMENTAL PROCEDURE | 32 |
| 4.1 Phase I (Bulk Samples study) | 32 |
| 4.1.1 Characterization Segment | 33 |

| | | |
|---------|--|-----|
| 4.2 | Phase II (Thin Films Study)..... | 34 |
| 4.2.1 | Characterization Segment | 35 |
| 5 | RESULTS AND DISCUSSIONS | 39 |
| 5.1 | Bulk Samples Study..... | 39 |
| 5.1.1 | Microstructure Analysis..... | 39 |
| 5.1.2 | Mechanical Property | 42 |
| 5.1.3 | Centrifugal and Gravity Casting Analysis..... | 43 |
| 5.1.4 | Nano-mechanical Properties | 46 |
| 5.2 | Thin Films Study | 54 |
| 5.2.1 | Profilometry Analysis (film thickness) | 54 |
| 5.2.2 | Mechanical Characterization: nanoindentation | 61 |
| 5.2.3 | Surface Morphology | 76 |
| 5.2.3.1 | Roughness Study | 76 |
| 5.2.3.2 | Hillock Formation | 83 |
| 5.2.3.3 | Average Grain Size..... | 86 |
| 5.2.3.4 | Summary | 89 |
| 5.2.4 | Structural Evaluation | 92 |
| 5.2.4.1 | Summary | 97 |
| 5.2.5 | Study of Temperature Effect..... | 97 |
| 5.2.5.1 | Mechanical Properties | 98 |
| 5.2.5.2 | Structural Evaluation..... | 107 |
| 5.2.5.3 | Summary | 110 |
| 6 | CONCLUSIONS..... | 112 |
| 7 | FUTURE WORK | 115 |
| 8 | REFERENCES | 116 |
| | Appendix A..... | 128 |
| | Appendix B..... | 129 |
| | Appendix C..... | 131 |
| | Appendix D..... | 133 |

FIGURES

| | | |
|-------------|--|----|
| Figure 3.1 | AlB ₂ hp3 crystal structure | 16 |
| Figure 3.2 | Sputtering process schematic of events by the ion impact based in Figure 31.1 by Aufderheide [55]. | 17 |
| Figure 3.3 | Sputtering assembly schematic based in Figure 31.2 by Aufderheide [55]. | 17 |
| Figure 3.4 | a) Load versus displacement curve, and b) nanoindentation upon loading and unloading [57], [59]. | 20 |
| Figure 3.5 | Based on schematic of the Hay-Crawford methodology: a) column effect in the indentation, and b) parallel and series spring system [63]. | 21 |
| Figure 3.6 | a) Nanoindenter G200 system; b) samples tray, and c) sample disk. | 23 |
| Figure 3.7 | Sketch of scratch test with the stylus tip based in Benjamin and Weaver [70]. | 24 |
| Figure 3.8 | Schematic scratch testing over film. | 26 |
| Figure 3.9 | Scratch graphic results from <i>NanoSuite</i> ® software controller of the G200 nanoindenter. | 27 |
| Figure 3.10 | Outline of the proposal for the adhesion strength calculation with the scratch technique: a) scratch and, b) forces and stress diagram. | 28 |
| Figure 3.11 | Schematic of the wear analysis with the scratch technique via nanoindentation: a ramp load scratch test. | 30 |
| Figure 4.1 | Sketch of graphite mold and the cavity necessary for casting the target specimens. | 32 |
| Figure 4.2 | a) Three sputtering guns, b) sputtering system, and c) target erosion. | 34 |
| Figure 4.3 | Sketch of substrates with vacuum tape: a) silicon wafer and, b) glass slide. | 35 |
| Figure 5.1 | Characteristic peak in the Al-xB castings. | 40 |
| Figure 5.2 | Micrographic image of Al-4B composite sample. | 40 |
| Figure 5.3 | Al-5wt.%B microstructure and AlB ₂ particle orientation planes (Reprinted from ref [13] by permission). | 41 |
| Figure 5.4 | Particle distribution within bulk samples: a) Al-1B, b) Al-2B, c) Al-3B and, d) Al-4B. | 42 |
| Figure 5.5 | Increasing boron levels raise the Brinell hardness (BH). | 43 |
| Figure 5.6 | Analysis using ImageJ: a) original picture, and b) processed image. | 43 |
| Figure 5.7 | Porosity and Rockwell superficial hardness. | 44 |
| Figure 5.8 | Mold section and the material entrance chamber: a) gravity casting, and b) centrifugal casting. | 45 |
| Figure 5.9 | Rockwell hardness (RH) analysis: a) section sample and, b) results hardness in normalized distance. | 45 |
| Figure 5.10 | Elastic modulus and (left column) and indentation micrographs (right column) on bulk samples: a) Al-1wt.%B, b) Al-2wt.%B, c) Al-3wt.%B and, d) Al-4wt.%B. | 48 |

| | |
|--|----|
| Figure 5.11 Evaluated nanohardness in bulk samples: a) Al-1wt.%B, b) Al-2wt.%B, c) Al-3wt.%B and, d) Al-4wt.%B..... | 49 |
| Figure 5.12 Elastic modulus (left) and indentations micrograph (right) in Al-1wt.%B (Al-1B) around of particles group..... | 50 |
| Figure 5.13 Nanoindentation results of particle cluster analysis in an Al-1B sample... | 52 |
| Figure 5.14 Mapping of the elastic modulus in composite samples: a) Al-1wt. %B, b) Al-2wt. %B, c) Al-3wt. %B and, d) Al-4wt. %B..... | 53 |
| Figure 5.15 Profilometry in Al-4wt.%B sample..... | 55 |
| Figure 5.16 Thickness as a function of sputtering power..... | 57 |
| Figure 5.17 Film growth types: a) layer (Frank- Van der Mayer); b) island (Volmer-Weber; c) Stranski-Krastanov [32]..... | 58 |
| Figure 5.18 Contour plots of film thickness in aluminum over glass slide deposited at: a) 100, b) 130, c) 160 and, d) 200 watts of sputtering power..... | 59 |
| Figure 5.19 Contour plots of film thickness in aluminum over silicon wafer deposited at: a) 100, b) 130, c) 160 and, d) 200 watts of sputtering power..... | 59 |
| Figure 5.20 Contour plots of film thickness in Al-4B over glass slide deposited at: a) 100, b) 130, c) 160 and, d) 200 watts of sputtering power..... | 60 |
| Figure 5.21 Contour plots of film thickness in Al-4B over silicon wafer deposited at: a) 100, b) 130, c) 160 and, d) 200 watts of sputtering power..... | 60 |
| Figure 5.22 Characteristic nanoindentation curve: a) aluminum and, b) Al-4B film samples..... | 61 |
| Figure 5.23 Elastic moduli in Al-4B films sputtered at 200 watts on: a) silicon wafer and, b) glass slide..... | 63 |
| Figure 5.24 Elastic moduli in aluminum films sputtered at 200 watts on: a) silicon wafer and, b) glass slide..... | 63 |
| Figure 5.25 Hardness of Al-4B films sputtered at 200 watts on: a) silicon wafer and, b) glass slide..... | 64 |
| Figure 5.26 Hardness of aluminum films sputtered at 200 watts on: a) silicon wafer and, b) glass slide..... | 64 |
| Figure 5.27 Average elastic modulus: a) Al-4B film and, b) aluminum film..... | 65 |
| Figure 5.28 Average hardness at the nanoscale: a) Al-4B film and, b) aluminum film..... | 66 |
| Figure 5.29 Scratch test results of Al-4B sputtered onto silicon wafer at: a) 100, b) 130, c) 160 and, d) 200 watts..... | 67 |
| Figure 5.30 Scratch test results for Al-4B film sputtered onto glass slide at: a) 100, b) 130, c) 160 and d) 200 watts..... | 68 |
| Figure 5.31 Scratch test results for aluminum film sputtered onto silicon wafer at: a) 100, b) 130, c) 160 and d) 200 watts..... | 68 |
| Figure 5.32 Scratch results for aluminum film sputtered onto glass slide at: a) 100, b) 130, c) 160 and d) 200 watts..... | 69 |
| Figure 5.33 Al-4B film surface scratched over: a) silicon wafer and, b) glass slide..... | 70 |

| | |
|---|----|
| Figure 5.34 Aluminum film surface scratched over: a) silicon wafer and, b) glass slide. | 70 |
| Figure 5.35 Detail at the section intermediate of scratched track for: a) Al-4B film and, b) aluminum film. | 70 |
| Figure 5.36 Elastic recovery area in scratch test. | 71 |
| Figure 5.37 Elastic recovery results in Al-4B and aluminum films sputtered in: a) silicon wafer and, b) glass slide substrates. | 72 |
| Figure 5.38 Friction coefficient (left) and adhesion strength (right) in film samples sputtered for both substrate. | 73 |
| Figure 5.39 SEM micrographs in scratched end for: a) Al-4B film and, b) aluminum film. | 74 |
| Figure 5.40 Wear volume in film samples. | 75 |
| Figure 5.41 Average RMS roughness in the film material. | 78 |
| Figure 5.42 RMS roughness: a) Al-4B films and, b) aluminum films deposited on glass slide. | 79 |
| Figure 5.43 RMS roughness: a) Al-4B films and, b) aluminum films deposited on silicon wafer. | 79 |
| Figure 5.44 AFM images of aluminum film fabricated to 130 watts. | 80 |
| Figure 5.45 AFM images of Al-4B film fabricated to 130 watts. | 80 |
| Figure 5.46 RMS roughness results in a) Al-4B and, b) aluminum film as function scan area. | 82 |
| Figure 5.47 Aluminum film surface for a) 100 nm and, b) 500 nm of thickness | 83 |
| Figure 5.48 Al-4B film surface for a) 100 nm and, b) 500 nm of thickness | 83 |
| Figure 5.49 Hillock growth at the aluminum films for sputtering power of: a) 100, b) 130, c) 160 and, d) 200 watts. | 84 |
| Figure 5.50 Suppression of growth hillock in Al-4B films for sputtering power of: a) 100, b) 130, c) 160 and, d) 200 watts. | 85 |
| Figure 5.51 High hillock in the samples. | 86 |
| Figure 5.52 Aluminum films grain boundary outline for each sputtering power a) 100 W, b) 130 W, c) 160 W and, d) 200 W. | 87 |
| Figure 5.53 Al-4B films grain boundary outline for each sputtering power a) 100 W, b) 130 W, c) 160 W and, d) 200 W. | 87 |
| Figure 5.54 Box and whisker plot sketch. | 88 |
| Figure 5.55 Box plots of film grain size. | 89 |
| Figure 5.56 X-ray pattern of aluminum films deposited on: a) glass slide and, b) silicon wafer substrates. | 93 |
| Figure 5.57 X-ray patterns of Al-4B films deposited on: a) glass slide and, b) silicon wafer substrates. | 94 |
| Figure 5.58 Pure aluminum x-ray pattern. | 95 |
| Figure 5.59 Lattice parameter a as function of sputtering power. | 97 |

| | |
|---|-----|
| Figure 5.60 Characteristic nanoindentation curve at 28°C in: a) Al-4B and, b) aluminum film samples. | 100 |
| Figure 5.61 Characteristic nanoindentation curve at 180°C in: a) Al-4B and, b) aluminum film samples. | 100 |
| Figure 5.62 Characteristic nanoindentation curve at 28°C after heating cycle: a) Al-4B and, b) aluminum film samples. | 100 |
| Figure 5.63 Temperature effects in elastic modulus to nanoscale on: a) Al-4B and, b) aluminum films. | 102 |
| Figure 5.64 Characteristic normalized nanoindentation curve at 28°C in: a) Al-4B and, b) aluminum film samples. | 104 |
| Figure 5.65 Characteristic normalized nanoindentation curve at 180°C in: a) Al-4B and, b) aluminum film sample | 104 |
| Figure 5.66 Characteristic normalized nanoindentation curve after heating cycle (at 28°C): a) Al-4B and, b) aluminum film samples. | 104 |
| Figure 5.67 Relative elastic recovery for the temperature extreme points. | 105 |
| Figure 5.68 Temperature effect on the hardness measured via nanoindentation. | 106 |
| Figure 5.69 In-situ high temperature x-ray diffraction pattern of the samples: a) Al-4B and, b) aluminum | 109 |
| Figure 5.70 Film lattice parameter (<i>a</i>) at different temperatures. | 110 |

TABLES

| | | |
|------------|---|-----|
| Table 4.1 | Centrifugal casting parameters..... | 32 |
| Table 4.2 | Composition chart samples by weight..... | 33 |
| Table 4.3 | CSM method parameters..... | 34 |
| Table 4.4 | CSM parameters used in the thin film method..... | 36 |
| Table 4.5 | Parameters for the ramp load scratch using lateral force..... | 36 |
| Table 4.6 | Parameters for the ramp load scratch using lateral force for the wear study. | 37 |
| Table 4.7 | Hot stage parameter test..... | 38 |
| Table 4.8 | Frame stiffness correction..... | 38 |
| Table 5.1 | Summary thickness with aluminum..... | 57 |
| Table 5.2 | Summary thickness with Al-4B..... | 57 |
| Table 5.3 | RMS roughness summary of Al-4B films..... | 77 |
| Table 5.4 | RMS roughness summary of Al films..... | 78 |
| Table 5.5 | RMS roughness summary..... | 82 |
| Table 5.6 | z-range at samples..... | 86 |
| Table 5.7 | Average grain size results..... | 87 |
| Table 5.8 | Lattice parameters measured in the sputtered films..... | 95 |
| Table 5.9 | Summary average results of load and displacement measured on the heated samples using the G200 nanoindenter..... | 101 |
| Table 5.10 | Mechanical properties measured in the sputtered films subjected to heating cycle by nanoindentation..... | 102 |
| Table 5.11 | Lattice parameters measured in the sputtered films for the heating cycle at HT-XRD..... | 109 |

ABBREVIATIONS

| | |
|---|------------------|
| Aluminum matrix composite | AMC |
| Functionally graded material | FGM |
| Scanning electron microscope | SEM |
| Aluminum diboride | AlB ₂ |
| Metal matrix composite | MMC |
| Al-4wt.%B composite | Al-4B |
| Silicon wafer | SW |
| Glass Slide | GS |
| Continuous Stiffness Measurement | CSM |
| High temperature x-ray diffraction | HT-XRD |
| Hot stage hardness and modulus | HS-HM |
| Joint Committee on Powder Diffraction Standards | JCPDS |
| Microelectromechanical systems | MEMs |
| Radio frequency | RF |
| Atomic force microscopy | AFM |
| Root mean square | RMS |

SYMBOLS

| | |
|---|-----------|
| Effective elastic modulus | E_{eff} |
| Elastic Modulus of diamond tip | E_i |
| Poisson ratio of diamond tip | ν_i |
| Indentation load peak | P_{max} |
| Contact area | A_c |
| Unloading stiffness | S |
| Poisson' ratio | ν |
| Depth contact | h_c |
| Adhesion strength | τ |
| Friction coefficient | μ |
| Lateral load | F_L |
| Normal load | F_N |
| Wear | W |
| Area cross section of the groove | A |
| Distance traveled the tip upon scratch test, interplanar distance | d |
| Yield pressure | Y_p |
| Deposition rate | d_r |
| Sputtering yield | S |
| Apparent modulus | E_a |
| Film modulus | E_f |
| Lattice parameter | a |

1 INTRODUCTION

Aluminum is a versatile structural material with many modern applications including home appliances, microdevices, transportation (land, sea and air) industry and commerce. Due to its excellent properties, aluminum has been also proposed as an interconnector layer in microelectromechanical systems (MEMs).

Moreover, AlB_2 particles embedded in an aluminum matrix modify and enhance numerous properties in the final multifunctional composite material. Most of these functionalized properties are the direct result of the interface between the matrix and the reinforcements. As a consequence, the interface and the surrounding phase or phases can be critically affected by residual stresses, over-stresses, and thermal stresses that cause changes in the matrix properties and the overall behavior of the composite material.

1.1 Literature Review

1.1.1 Functionally Graded Materials (FGMs)

Aluminum is the second metallic element most abundant on Earth and advances in the science and engineering of materials thrust the production and applications of this material. Among some important characteristics of aluminum and its alloys there are their workability, adjustable strength, ductility, low density, the low cost, recyclability, among others. These features make this type of material ideal for structural, architectural, marine, aerospace and automotive applications.

A composite material is a mixture of two or more different chemical materials with distinct interface. In particular, one kind of aluminum matrix composites (AMC) is that involving AlB_2 (aluminum diboride) reinforcement particles. The reinforcing particles are used to improve the AMC mechanical strength and elastic modulus [1]. For instance, in a composite made of Al-Cu-B, Calderón found that AlB_2 particles decreased the ductility and increased the tensile strength of the material [2].

The AMCs can be turned into functionally graded materials (FGMs) by centrifugal casting. This casting process generates particle segregation by centrifugal forces as a result of the density difference between the liquid matrix and the solid particles upon processing. In 1991, Fukui presented a mathematical model to describe the gradient of ceramic particles distribution as a function of the centrifugal force and volume fraction [3]. The material used was plaster mixed with powdered corundum (Al_2O_3). This is possible because FGMs are non-homogeneous materials with gradual changes in the microstructure, which results in a gradient of properties [4]. Moreover, processing factors such as the melting temperature, the speed of rotation and the mold temperature in the manufacturing of these materials influence their properties [5]. To this purpose, Kang and Rohatgi studied one-dimensional heat transfer analysis upon centrifugal casting of an aluminum/copper alloy with Al_2O_3 , SiC_p , and graphite particles. A numerical model of the particles dispersion was used including the variation of volume fraction in radial form. Melgarejo et al. analyzed an Al-Mg-B alloy fabricated by centrifugal casting bearing varying boron level (1, 2, 3 to 4 weight percent) and were able to produce particles segregation at radial distance along the casting [6]. Subsequently the hardness testing (Rockwell and Vickers) a gradual hardness

increases in the radial direction proportional to the AlB_2 volume fraction. A similar work was completed by Adelakin and Suárez, who found the formation of two types of ceramic particles in the composite of Al-Mg-B (AlB_2 and AlB_{12}) [7]. The results also showed higher hardness along consistently with the amount of particles segregated radially.

Another study of metal matrix composites with reinforcement particles of SiC exhibited FGMs properties by means of centrifugal casting [8]. This performance was reflected in the variation of Brinell hardness results in the samples of 20%SiC_p/Al alloy. There was an increase in hardness proportional to the amount of SiC particles segregated in the external zone.

Friction and wear resistance properties also have been the object of several studies in the FGMs. Gomes et al. worked on a homogeneous matrix composite reinforced with 20%SiC particles in volume, where the samples were melted in a high frequency induction furnace and cast via centrifugal casting [9]. Tribological experiments were performed using a pin-on-disk apparatus without lubrication, at a constant sliding speed of 0.5m/s, and a normal load of 5N. They computed the wear coefficient as $K=V/(W \cdot x)$, where V is the wear volume taking into account the density of material; W is the normal force, and x is the sliding distance. The friction coefficient (f) is the ratio between the friction force, which was assessed by a bending type force transducer, and the normal force value. The results showed a wearing effect greater in the homogeneous material composite than the samples that were centrifugally cast. Additionally, Melgarejo et al. and Watanabe et al. in their corresponding research efforts included wear tests [6], [10]. The tests showed gradual variability in different areas of the castings.

1.1.2 Mechanical Properties Studies via Nanoindentation in FGMs

More recently Ramos et al. studied an Al-Si matrix reinforced with particles of AlB_2 and AlB_{12} [11]. They studied the materials hardness at the macro, micro- and nanoscales. Their results demonstrated a different hardness behavior at those scales due to the matrix/particle relationship. Other nanoindentation study on an Al-Li 8090 alloy reinforced with 15 vol. % SiC particles determined the Young's modulus and hardness at the metal matrix and ceramic reinforced (SiC); in this case, the hardness measure in the reinforced matrix was around 20% higher than in unreinforced Al-Li alloy [12]. It is apparent then that the particle-matrix interaction is fundamental for understanding the behavior of metal matrix composite materials. For instance, a study by Melgarejo et al included this interaction in a functionally graded composite with an aluminum matrix containing AlB_2 particles [13]. In this research, nanoindentation loads between 4 to 8 mN, were applied on individual particles with sizes between 3 and 10 μm . The results demonstrated the effect of particle size influence on pushed-in particles into the softer matrix; using strain gradient plasticity theory the authors explained the size dependence of the *push-in* force.

Residual stresses in composite materials are another area of study developed thanks to nanoindentation. The residual stresses can be generated during the cooling process caused by differential thermal expansion between the particle and the surrounding metal matrix. Olivas et al. worked on aluminum matrix composite reinforced with SiC particles and found that the tensile biaxial residual stress in aluminum increased with the particle volume fraction [14]. For a composite containing 30 vol.% SiC_p , the residual

stress obtained in the aluminum was of 268.8 MPa. This value is low compared with the yield strength (390 MPa) of the unreinforced aluminum matrix 2080.

The aforementioned studies provided evidence to the reinforcement particle efficacy within an aluminum matrix, justifying the production of these composite materials with improved performance and mechanical properties. Additionally, it is apparent that the centrifugal casting method ensures segregation of reinforcement particles in the casting.

Hence, this research in its first instance aims to study and characterize of a composite aluminum matrix reinforced with AlB_2 particles and fabricated via centrifugal casting. This casting method permits the fabrication of a composite bearing a gradient of denser particles, which segregates in the aluminum melt toward the outside of the casting, as a result of centrifugal forces.

1.1.3 Thin Films Studies

In 2002, Farooq and Lee presented a work on the optimization of the sputtering process for the fabrication of composite thin films [15]. The materials used in the experiments were aluminum, nickel, vanadium in metallic thin films and dielectric material (SiO_2 and Al_2O_3) over glass substrate. The results demonstrated that the sputtering rate increases with increasing chamber pressure and with the deposition current.

Jeong et al. studied the effects of the sputtering parameters on the structural, electrical, and optical properties of undoped and aluminum-doped ZnO thin films on glass substrates [16]. The tests showed that increasing the Al content (0 to 4 wt.%) reduces

the resistivity from $5.0 \cdot 10^{-1} \Omega \cdot \text{cm}$ to $9.8 \cdot 10^{-2} \Omega \cdot \text{cm}$ while resistivity also increases with rising of temperature of substrate.

In another research a nanocomposite made of aluminum magnesium boride thin films was prepared on Si (100) substrates by Wu et al. with a three targets magnetron sputtering [17]. They observed that boron content influenced the films properties. The maximum hardness of the thin film (approximately 31 GPa) was obtained with 65 at% boron. Also, the low roughness (0.5 nm) proved that this deposition technique is a promising method to fabrication Al-Mg-B thin films.

Ramos and Suárez characterized Al-B-Si thin films deposited on glass slides and a silicon wafer substrate, using direct current (DC) via magnetron sputtering [18]. The deposition targets were produced by centrifugal casting. This processing method allowed obtaining a FGM constituted by an aluminum matrix containing boron forming AlB_2 and AlB_{12} particles as reinforcements. This study evinced that the thin film with best quality (low roughness) was produced using maximum power (450 watts) and the silicon substrate. Additionally, mechanical properties such as hardness, elastic modulus and adhesion were higher in the thin films produced with FGM targets compared to a pure aluminum target.

Bilayer thin films have also been object of studies via nanoindentation. In thin films of tantalum and copper deposited on thermally oxidized silica via magnetron sputtering, the hardness and elastic modulus were determined using nanoindentation [19]. The results demonstrated an apparent dependence of hardness on the copper layer that decreased with an increase of thickness, whereas the elastic modulus did not. In a

particular case in monolayer metallic thin film on silicon substrate using a conventional evaporation system this dependence between the roughness results and the thickness of thin film is apparent [20]. This explains why the substrate (metal or silicon) and deposition method affects the surface roughness of thin films.

1.1.4 Ancillary Research with Further Discussion of Pertinent Literature

In composite materials bearing a metal matrix with reinforcement particles important local effects can occur between the constituents. The edge effect is considered where elastic discontinuity occurs in a study by Jakes and Stone, and Jakes et al an [21], [22]. They developed a model to eliminate (or correct for) artifacts in the load-depth data caused by very heterogeneous phase distributions. The artifacts upon nanoindentation tests can generate false results that reflect a credible trend of some properties as a function of the position. This can be understood and corrected in terms of structural compliance, C_s , which is independent of the size of the indent.

Additionally, specialized scratch studies of thin films have been developed via nanoindentation. For instance, copper thin films were studied by Beegan et al. who measured the film hardness using the continuous stiffness method and low loads during the scratch; then they compared their results with the hardness calculated by conventional nanoindentation [23]. Their results determined that the hardness decreased with the thickness of the film. Other materials such as SiO_2 , SiC, Ni-P and Au have been studied using this scratch method [24]. This research revealed that SiC film presented scratch resistance compared with the other materials. Moreover, Bhattacharyya and Mishra worked on Si-C-N thin films fabricated via RF magnetron

sputtering [25]. During nanoscratching experiments they observed that the films failure mechanism changed from cohesive failure at lower loads to adhesive failure at higher loads.

Additionally, the temperature effects have also been studied via nanoindentation. A study of the microscopic superelastic behavior of thin-film NiTi by instrumented indentation at different temperatures revealed that the load-depth curves showed microscopic superelastic behavior above the final transformation temperature of austenite A_f [26]. This indentation-induced superelasticity exists at temperatures about 100°C above A_f . A probable cause for this effect is the high hydrostatic pressure under the indenters, which raises the transformational temperature.

Finally, it should be noted that some models have been developed to complement the experimental data. For instance, Muir Wood and Clyne used a nickel-titanium shape memory alloy that was subjected to nanoindentation over a temperature range up to 200°C (martensitic transformation) [27]. The resulting load-displacement data showed the onset of the superelastic deformation mechanics in the material. This interpretation was assisted by finite element simulation of the evolving strain field upon indentation, with or without the superelastic deformation mechanism being operative.

1.1.5 Aluminum Thin Film Issues

Microelectromechanical systems (MEMs) use aluminum as layer interconnector for its low resistivity, ease of deposition, and the dry etching availability. Also, it does not contaminate with Si and has excellent adhesion to dielectrics. Unfortunately, it presents issues of electromigration and hillock formation on thin films.

Solid state electromigration is defined as the loss of material in a solid (mass transport) by effects of a current density that flows through a conductor [28]. Failures by electromigration in high power devices and integrated circuits have been reported for the last decades. Black, in a study on open circuit failure in these devices generated by the current flow in aluminum films, observed that the failure time depended on the aluminum crystallite size of film when the current density was varied [29]. Another study analyzed the damages that caused the electromigration in bamboo aluminum interconnects in tests conducted with different current densities (0.04 to 5MA/cm²) and temperature (200°C to 250°C) [30]. Witt found in images taken via scanning electron microscope (SEM) damages such as voids, hillocks, and passivation cracking in the samples. In addition, this problem has been evaluated by finite element models. In a simulation of solder joints in nanoelectronics, Basaran and Lin revealed the influence of crowding current and the effects of thickness in the failure in flip chip microelectronics [31]. Results of the tests and simulations showed the effect of eliminating or reducing the current crowding in the failure time of the solder joints with current densities below $0.6 \cdot 10^4 \text{ A/cm}^2$.

Another detrimental phenomenon occurring during deposition of aluminum films is the hillock growth. The formation of hillocks in the aluminum films is the result of stresses relaxation of the film material [32], or due to stresses related to the difference in the coefficients of thermal expansion among material and substrate carrying the material to the surface [33], [34]. This later explanation could be discarded since upon sputtering the films only experience a slight warming.

In this respect a study of thin films fabricated by evaporation examined the thickness and annealing effects on the hillock size at the films [35]. Using SEM they revealed the dependence of hillock size and depression on both processing parameters. Similarly Bordo and Rubahn used electron beam evaporation to fabricate aluminum films on unheated silicon, glass or mica substrates [36]. They found that high rates deposition (1 nm/s - 2 nm/s) affected the hillock generation. In another study on hillock suppression Onishi et al. deposited thin films using an Al-Nd alloy target using a magnetron sputtering with direct current. The characterization results showed as the neodymium (Nd) content between 2.0 to 6.0 at.% in alloy target suppressed the hillock formation [37]. In another study on Al-Cu alloy applications in microelectromechanical systems (MEMs) the hillock on thin films was analyzed using atomic force microscope (AFM) [38]. AFM images displayed hillock suppression due to the copper content in the alloy.

The cited literature discusses the sputtering method as a deposition technique of aluminum alloys or aluminum composites for manufacturing thin films on different kinds of substrates. Characterization results in these composite films showed higher hardness and elastic modulus, low roughness surface and hillock suppression, in contrast to aluminum films.

Based on previous investigations and on the work by Ramos and Suárez who fabricated thin films by magnetron sputtering from a monolithic composite target (Al-Si-B) [18], we propose to study thin films deposited via magnetron sputtering using as target an aluminum matrix composite reinforced with AlB_2 particles. Our goal has been to assess how this composite and the sputtering parameters affecting the material when it is

deposited as thin film. Consequently, this material could be proposed as an alternative to pure aluminum used in microelectromechanical systems (MEMs).

2 OBJECTIVES

2.1 General Objective

To study a lightweight, high strength, multifunctional Al/AlB₂ composite material at the macroscale (bulk samples) and the nanoscale (thin films), prepared by centrifugal casting and radio frequency magnetron sputtering, respectively.

2.2 Specific Objectives

The research work will focus on the following specific objectives:

- Fabricate via centrifugal casting both target and samples for thin film deposition and materials characterization, respectively.
- Characterize the material properties of bulk Al/AlB₂ samples and the effects of the particle concentration using the following techniques:
 - X-ray diffraction and optical microscopy
 - Brinell hardness as mechanical characterization at the macroscale
 - Instrumented nanoindentation as mechanical characterization at the nanoscale
- Produce via a magnetron sputtering unit using radio frequency thin films of monolayer and multilayer samples over glass slide and silicon wafer substrates.
- Characterize thin film samples using the following techniques:
 - Profilometry for film thickness measurements

- Instrumented nanoindentation for mechanical characterization
- Atomic force microscopy, and x-ray diffraction for surface morphology and structural evaluation, correspondingly

3 THEORETICAL BACKGROUND

3.1 Metal Matrix Composites

A metal matrix composite (MMC) is formulated with materials of different nature (chemical and physical). Essentially, the material has one constituent in larger proportion, i.e. the metallic matrix, whereas the other, the dispersed one, acts as reinforcement. In MMCs such reinforcement improves the properties of the matrix that is generally a lightweight and ductile metal [39], [1], [2]. In both, continuous reinforcing elements (fibers) or discontinuous ones (particles, short fibers, whiskers, platelets), the matrix/reinforcement bonding is fundamental in the mechanical behavior of the material [1], [40], [41].

Since the 1960s MMCs have been developed and became relevant for applications in the automotive and aerospace industries as well as for electronics and commercial products [39], [40], [42]. For such applications, upon MMC fabrication it is important to consider the ductility, density, and thermal expansion of the matrix along with the stiffness, hardness, and low thermal expansion coefficient of the reinforcement [39]. Accordingly, materials such as titanium, magnesium, copper, iron and particularly aluminum have been studied to promote the use of these composites in diverse industries [39], [40], [42].

3.1.1 Aluminum Matrix Composite (AMC)

Pure aluminum has important properties such as low theoretical density (2.698 g/cm^3), high electrical conductivity ($2.63 \mu\Omega\cdot\text{cm}$), wide range of ductility (depending on prior plastic deformation or alloying elements), and low melting point (660°C), which make

the metal an appealing material for metal matrix composites [43], [44]. Among the reinforcement materials for aluminum or aluminum alloys are SiC, Al₂O₃, B (pure or as a compound), ZrO₂ and C (as graphite or nanotubes). In some fabrication processes the molten metal reacts with an additive and forms the particles, which reinforce the composite matrix after solidification [39], [41].

One can consider Al-B alloys as an aluminum matrix composite that contains AlB₂ particles [45]. In its production a tetrafluoroborate salt (KBF₄) chemically reacts with molten aluminum releasing boron atoms that then combines with surrounding aluminum atoms to form aluminum borides [46]. Another processing method to produce Al-B alloys with AlB₂ particles was investigated by Birol with a mixture of aluminum (5 g) and KBF₄ (1.8 g) prepared by ball milling [47]. He found that at 490°C KBF₄ began to react with aluminum in the blend, at lower temperature than the melting point of aluminum (660°C). The AlB₂ phase was identified by x-ray diffraction and via optical micrographs.

Aluminum diboride AlB₂ possesses a hexagonal closed packed hp3 crystal structure [46], [48]–[50], where lattice parameter $a = 3.0054$ nm and lattice parameter $c = 3.2576$ nm (Figure 3.10). These values were provided from powder diffraction standard pattern JCPDS 39-1483. The aluminum atoms are located in the basal planes (A) and the boron atoms (B) in the horizontal central plane with a stacking sequence ABABABABA (Figure 3.1). The particles have density of 3.1 g/cm³ and a melting point of 1,655°C [51]. The literature reported values of 250.2 GPa for the elastic modulus (E) and 0.274 to 0.29 for the Poisson' ratio (ν) [48], [52].

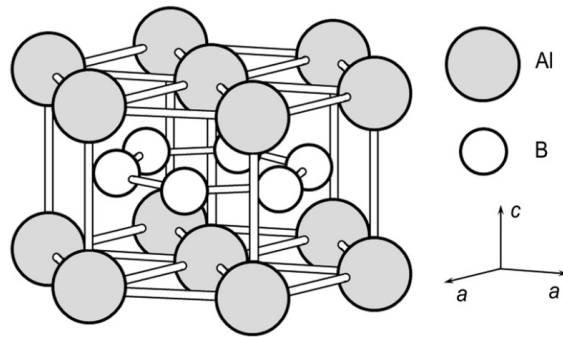


Figure 3.1 AlB₂ hp3 crystal structure

3.2 Thin Films Coating

Layered composite materials can also be produced via sputtering at the submicron and nanoscale. This technique is used to generate thin films for conductors, resistors, capacitors, transparent conductors and as electrodes for LCDs, touch panels, other display devices, and solar cells.

3.2.1 General Sputtering Process

Sputtering is a momentum transfer process caused by gas ions (normally Ar⁺) in plasma produced by an electric field in a vacuum chamber. These incident ions are accelerated by the electric field towards a cathode with sufficient energy for dislodging the atoms of the cathode surface or material target (Figure 3.2). These *tooled out* atoms acquire enough energy to reach a substrate and adhere to it to form the film [32], [53]–[55].

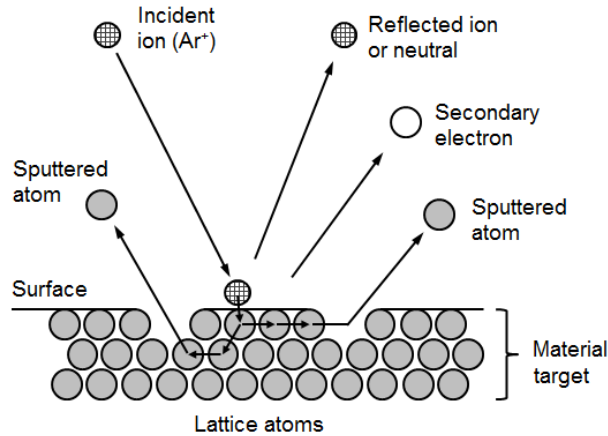


Figure 3.2 Sputtering process schematic of events by the ion impact based in Figure 31.1 by Aufderheide [55].

A simple schematic configuration to represent sputtering is shown in Figure 3.3. The vacuum chamber is equipped with a target (cathode), which is the source of the material to be deposited, and a substrate to be coated (anode).

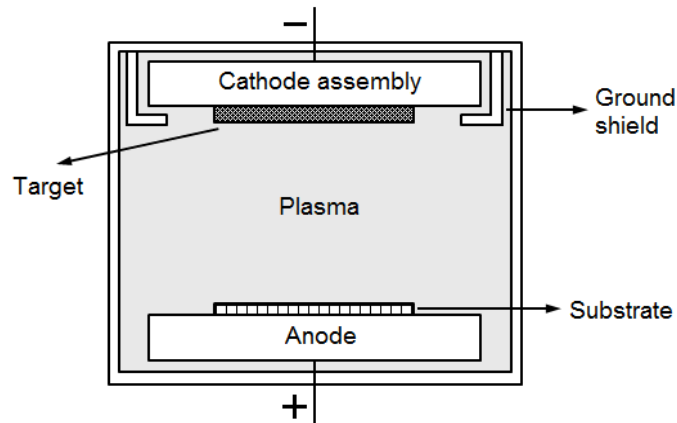


Figure 3.3 Sputtering assembly schematic based in Figure 31.2 by Aufderheide [55].

The sputtering process is carried out under vacuum ($\sim 10^{-3}$ torr) so as to prevent the contamination of the thin films caused by impurities or residual gas.

The sputter has almost no restrictions in terms of the target materials for deposition. For pure metals, direct current (DC) is used as the power supply while dielectrics and

semiconductor materials require a radio frequency (RF) power source. This RF sputtering setting can also be used in conductor materials (metallic target) [32], [53]–[55].

3.2.2 Magnetron Sputtering

Magnetron sputtering is a type of sputtering system that uses a magnetically enhanced cathode/anode. The magnetic field functions as an electron trap that, in conjunction with the cathode surface, confines the $E \times B$ (electric field strength \times magnetic flux density) electron drift currents to a closed-loop path on the target surface. The magnetic confinement near the target results in higher achievable current densities at lower pressures (10^{-3} to 10^{-2} torr), nearly independent of voltage. This system produces higher deposition rate with lower electron bombardment of the substrate and therefore low heating [32], [53]–[55].

Factors affecting the deposition rate are: a) the power density on the target; b) the erosion area; c) the distance to the substrate, d) the target material, e) the sputter yield and; d) the gas pressure. A disadvantage of the magnetic field-assisted sputtering is that the erosion of the material is not uniform and there is a great waste of material. This is so because the sputtering is more intense where the magnetic field lines are parallel to the cathode surface [32], [53]–[55].

3.3 Material Characterization

3.3.1 Mechanical Properties

The superficial hardness can be determined by using Rockwell or Brinell tests. Generally this bulk property is defined “as the ability of a material to resist permanent

indentation or deformation when in contact with an indenter under load” [56]. The indentation into the sample surface is produced in a universal Rockwell tester that uses a vertical force and standard steel ball indenter. The Brinell hardness (MPa) can then be determined with equation 3-1.

$$HB = \frac{L}{\frac{\pi \cdot D}{2} \cdot (D - \sqrt{D^2 - d^2})} \quad (3-1)$$

where L is the load in newton's, D is the ball diameter in mm, and d is the diameter of the indentation in mm, measured with a microscope. The superficial Rockwell is based on the ASTM E 18-16 standard.

Oliver and Pharr developed a new technique for the determination of hardness and elastic modulus at the nanoscale in bulk samples and thin films [57]. The values are obtained based on measures of load and displacement upon indentation experiments. Figure 3.4 shows a schematic load versus displacement curve and a sketch of the indentation used for calculating the hardness (equation 3-2) and elastic modulus (equation 3-3) in the film:

$$H = \frac{P_{max}}{A_c} \quad (3-2)$$

$$\frac{1}{E_{eff}} = \frac{(1 - \nu^2)}{E} + \frac{(1 - \nu_i^2)}{E_i} \quad (3-3)$$

where P_{max} is the indentation load peak, A_c is the contact area between the indenter and the sample as function of h_c (equation 3-6), ν is the Poisson's ratio of the material, E_i

and ν_i are the elastic modulus and Poisson's ratio of the indenter (diamond), and E_{eff} is the effective elastic modulus, calculated via equation 3-4:

$$E_{eff} = \frac{1}{\beta} \cdot \frac{\sqrt{\pi}}{2} \cdot \frac{S}{\sqrt{A_c}} \quad (3-4)$$

where S is the unloading stiffness (Figure 3.4a) determined in the unloading curve, A_c is the contact area between tip and specimen, and β is a correction factor that depends on the tip geometry. In particular, for a Berkovich indenter the A_c is calculated with equation 3-5 [58], where C is an empirical constant of 150nm or less for a total depth indentation h less than 2 μm .

$$A_c = 24.56 \cdot h_c^2 + C \cdot h_c \quad (3-5)$$

$$h_c = h - 0.75 \cdot \frac{P_{max}}{S} \quad (3-6)$$

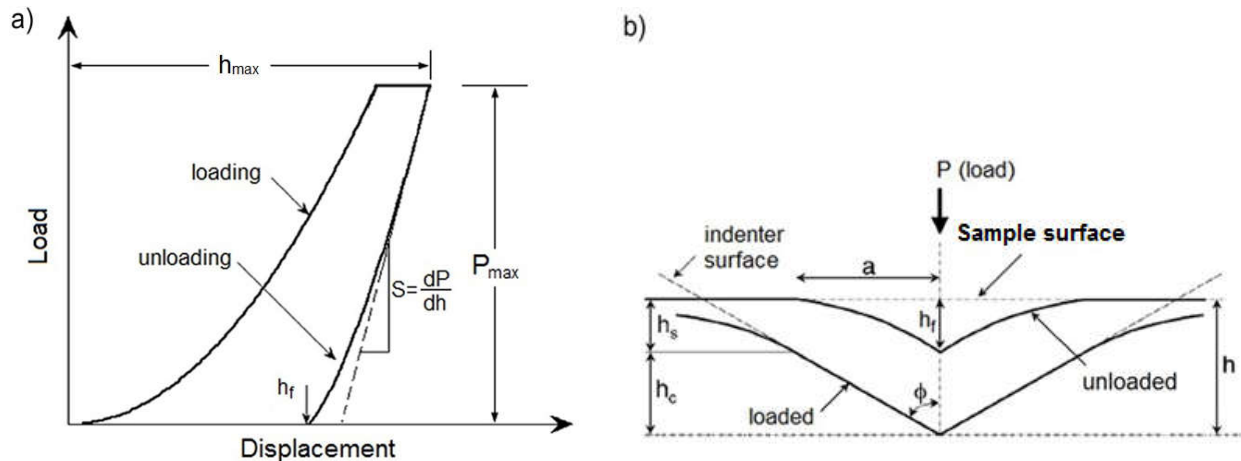


Figure 3.4 a) Load versus displacement curve, and b) nanoindentation upon loading and unloading [57], [59].

This technique was refined in 2004 by the same authors who developed the method of continuous stiffness measurement (CMS) [60]. In this method continuous measurement of the stiffness on the sample is possible via small dynamic oscillations during the application of the indenting force.

Other studies focused on the determination of the mechanical properties of thin films without the influence of the substrate since different substrates can affect the results obtained by nanoindentation, a problem found in the literature [60]–[62]. In 2011, Hay and Crawford [63] developed a model based on the methodology of Rar et al. [64] to eliminate this artifact.

Figure 3.5 shows a schematic of this model representing the film/substrate system (Figure 3.5a) as a spring system in series and parallel (Figure 3.5b). The stiffness for each spring is provided by the film stiffness, substrate nature and the stiffness of the film lateral support that buttresses the column of width $2a$ underneath the indenter (Figure 3.5a), respectively.

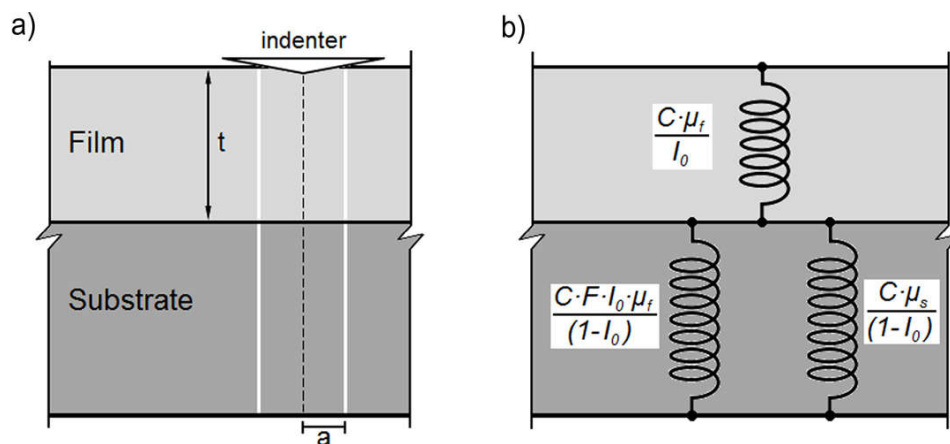


Figure 3.5 Based on schematic of the Hay-Crawford methodology: a) column effect in the indentation, and b) parallel and series spring system [63].

The solution for film/substrate system is given by the equation 3-7:

$$\frac{1}{\mu_a} = (1 - I_0) \cdot \frac{1}{\mu_s + F \cdot I_0 \cdot \mu_f} + I_0 \cdot \frac{1}{\mu_f} \quad (3-7)$$

The I_0 , F , μ_a , μ_f , and μ_s terms are the weighting function, an empirical constant, the apparent shear modulus of the system, and the shear modulus of film and substrate, respectively. Using the quadratic solution for μ_f of the equation 3-8, the result is:

$$\mu_f = \frac{-B + \sqrt{B^2 - 4 \cdot A \cdot C}}{2 \cdot A}$$

where:

$$\begin{aligned} A &= F \cdot I_0 \\ B &= \mu_s - (F \cdot I_0^2 - I_0 + 1) \cdot \mu_a \\ C &= -I_0 \cdot \mu_a \cdot \mu_s \end{aligned} \quad (3-8)$$

where μ_s is obtained in terms of the substrate properties, as the elastic modulus and Poisson's ratio with the well-known equation 3-9:

$$E = 2 \cdot \mu \cdot (1 + \nu) \quad (3-9)$$

The apparent shear modulus, μ_a , is calculated applying the Oliver and Pharr methodology [57], but the solution also requires of an apparent Poisson's ratio ν_a . This value is defined according equation 3-10 [65]:

$$\nu_a = 1 - \left[\frac{(1 - \nu_s) \cdot (1 - \nu_f)}{1 - (1 - I_1) \cdot \nu_f - I_1 \cdot \nu_s} \right] \quad (3-10)$$

In this expression the I_1 term is another weighting function. I_1 and I_0 consider the film thickness (t). The Poisson's ratio and the contact radius (a) for the film-substrate

transition of shear modulus are also present [66]. These functions are obtained according to equations 3-11 and 3-12:

$$I_1 = \frac{2}{\pi} \cdot \arctan\left(\frac{t}{a}\right) + \frac{t/a}{\pi} \cdot \ln\left(\frac{1 + \left(\frac{t}{a}\right)^2}{\left(\frac{t}{a}\right)^2}\right) \quad (3-11)$$

$$I_0 = \frac{2}{\pi} \cdot \arctan\left(\frac{t}{a}\right) + \frac{1}{2 \cdot \pi \cdot (1 - \nu_a)} \cdot \left[(1 - 2 \cdot \nu_a) \cdot \frac{t}{a} \cdot \ln\left(\frac{1 + \left(\frac{t}{a}\right)^2}{\left(\frac{t}{a}\right)^2}\right) - \frac{t/a}{1 + \left(\frac{t}{a}\right)^2} \right] \quad (3-12)$$

Finally, the film elastic modulus is determined with the shear modulus (μ_f) and ν_a (equation 3-10):

$$E_f = 2 \cdot \mu_f \cdot (1 + \nu_f) \quad (3-13)$$

The nanoindentation instruments, such as the G200 Agilent Nanoindenter (Figure 3.6) use the Oliver and Pharr [57], [59] and Hay et al [63] methodologies for determining the elastic modulus and hardness at the nanoscale.

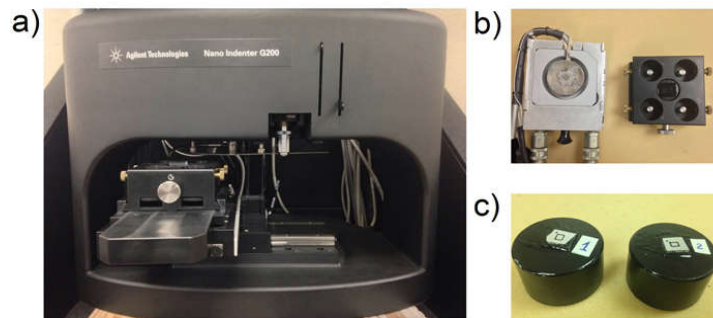


Figure 3.6 a) Nanoindenter G200 system; b) samples tray, and c) sample disk.

Further, the adhesion strength, the friction coefficient, and the wear resistance are other properties of interest in the study of thin films.

The adhesion strength term is defined as the bond existing between the contact surfaces of two materials via mechanical scratch action and is the stress required for separating the film material from its substrate. The methods used for quantifying this property can be qualitative, quantitative, destructive, non-destructive, mechanical, and non-mechanical, among other methods [67]. Benjamin and Weaver in 1960 used the micro-scratch technique with a stylus tip to determine the adhesion strength in terms of the shearing stress (τ) [67], [68], [69], [70]. They used the forces and stresses diagram in Figure 3.7 to obtain the equation 3-13. This expression defines the shearing stress (τ) as a function of the vertical critical load (W_{cr}), the contact radius (a), and the stylus radius tip (R).

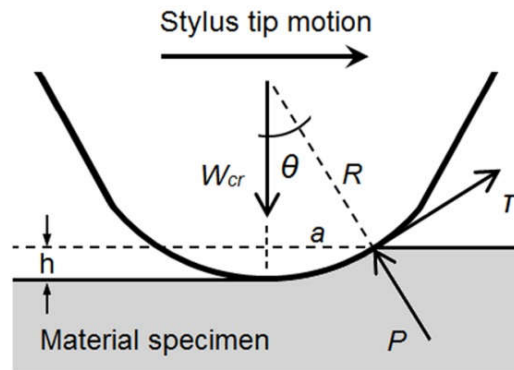


Figure 3.7 Sketch of scratch test with the stylus tip based in Benjamin and Weaver [70].

$$\tau = \frac{W_{cr}}{\pi \cdot a \cdot R} \cdot \left(\frac{a}{\sqrt{R^2 + a^2}} \right) \quad (3-14)$$

In 1987 Burnett and Rickerby and then in 1991 Bull and Rickerby while studying the adhesion strength analysis considered the effects of field flow stress on the surface, the friction between tip and material, and the internal stresses occurring during the scratched test [70]–[72]. Under these conditions, they determined a relationship that linked the adhesion work (W_{ad}) with the critical normal load (W_{cr}), which resulted in equation 3-15.

$$W_{cr} = \frac{\pi \cdot a^2}{2} \cdot \left(\frac{2 \cdot E \cdot W_{ad}}{t} \right)^{\frac{1}{2}} \quad (3-15)$$

where E is the elastic modulus and t is thickness of the film. W_{ad} value is determined of a W_{cr} versus $a^2/t^{1/2}$ plot where the slope of the graphic is $0.5 \cdot \pi \cdot \sqrt{(2 \cdot E \cdot W_{ad}/t)}$. This methodology has difficulty in the accuracy of the critical load (W_{cr}).

By nanoindentation it is also possible to determine the adhesion strength in coating. In this test, the critical load that produces the film fracture is obtained from various indentations with different loads. The minimum load that causes the material fracture defines the film adhesion [24], [72]. Later on, with advances in technology, nanoscaled scratch tests were developed. The nanoindenter apparatus was able to measure the horizontal and vertical force at different times during the scratch test. Figure 3.8 illustrates a scratch test. The test applies a gradual load from zero to a maximum value at the scratched end and it creates a track on the surface by material removal.

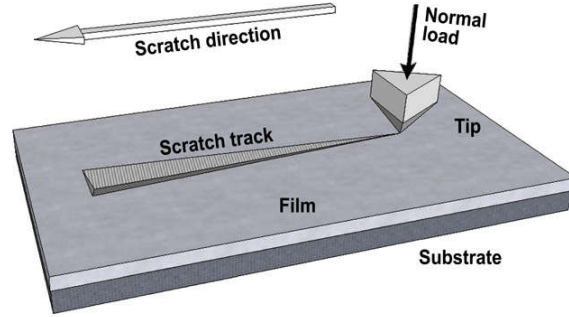


Figure 3.8 Schematic scratch testing over film.

The nanoscratch technique provided researchers with the possibility of determining the friction coefficient of the film material and the interface with the substrate. The friction coefficient value (μ) is calculated as the ratio between the lateral load (F_L) divided by the normal load (F_N) at the depth of interest (equation 3-16). This definition has been commonly applied in tribological studies conducted via nanoindentation as a measure of the adhesion of thin films [73]–[77].

$$\mu = \frac{F_L}{F_N}. \quad (3-16)$$

Other authors indicated that the friction coefficient (μ) in the sliding surface comprises the components such as deformation asperity (μ_d), adhesion (μ_a) and plowing (μ_p) [56], [78]–[84]. A nanotribological study over amorphous carbon thin films found that the differences in this coefficient could have been effects of adhesion and plowing [81], [85]. Therefore, they expressed μ as the sum of the contributions of μ_a and μ_p . The adhesion term can then be calculated with equation 3-17:

$$\mu_a = \frac{A \cdot \tau}{L}. \quad (3-17)$$

where A is the contact area, L the normal load and τ shear strength on the contact surface, and for the plowing (μ_p) used an expression defined for Komvopoulos in 1991 [86]. Experimentally they observed the changes in the friction coefficient and its dependence on the scratch load. The plowing friction (μ_p) is an effect of the hard asperities and the wear particles trapped on the sliding surfaces [78]–[80], [87], [88]. This component may be neglected provided that one of the contact surfaces be very hard; this would prevent wear particles from being entrapped in this surface during the test [56], [79].

The G200 nanoindenter apparatus (Figure 3.6) uses the NanoSuite® software as a controller. The software controls the ramp-load scratch test, records the depth data, the scratched distance and the horizontal or lateral loading for each increase of vertical load. The test consists of three tracks: first the tip makes a scanning line of the surface on the test area (surface topography); then the scratch is completed (scratch curve); and finally, the tip carries out another scanning line of the scratch (residual deformation). These three tracks are identified in Figure 3.9.

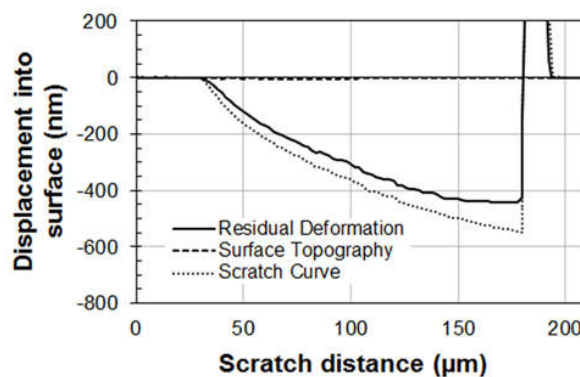


Figure 3.9 Scratch graphic results from *NanoSuite*® software controller of the G200 nanoindenter.

The theories and methodologies previously presented are directed toward defining an expression for adhesion as a stress or as a function of the friction coefficient in the material or in the interface with the substrate via a scratch test. Based on these methodologies and using the load ramp technique via nanoindentation we decided to generate an alternative expression for the adhesion strength.

Our analysis proposes the use of the horizontal and vertical force measured with the nanoindenter in scratch testing and the Berkovich tip geometry with face forward motion (Figure 3.10). The proposal is based on shearing stress methodology by Benjamin Weaver [89], [72] but using the resultant force acting in the scratch test and the contact area. In addition, this analysis disregards the plowing effect in the adhesion strength assuming that the surface hardness of the tip does not permit the entrapment of wear particles, which could be insignificant [56], [79].

The adhesion strength (τ) would be defined as the stress that produces the release of the material sample gliding on the tip face as a result of the acting forces.

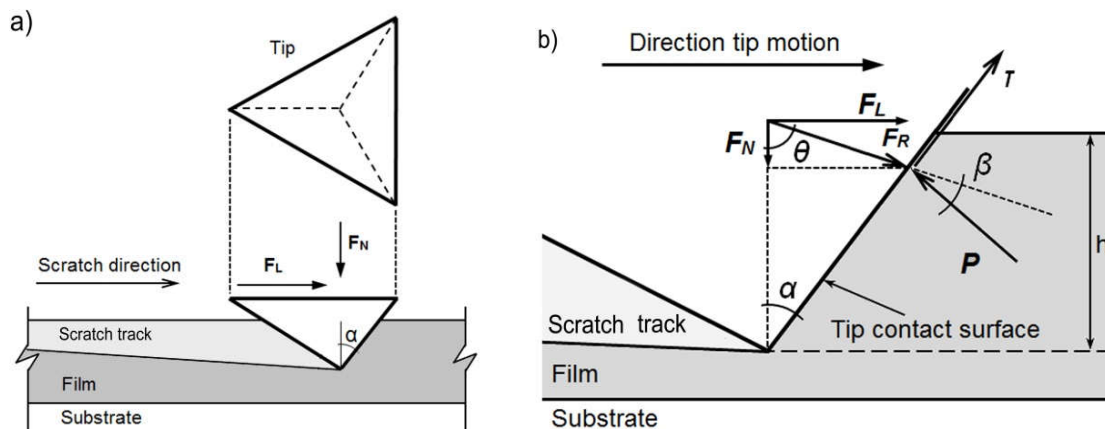


Figure 3.10 Outline of the proposal for the adhesion strength calculation with the scratch technique: a) scratch and, b) forces and stress diagram.

In the sketch of Figure 3.10b, the adhesion strength (τ) is given by equation 3-18 (see Appendix B):

$$\tau = \frac{\sqrt{3} \cdot F_R \cdot \cos \beta \cdot \cos \alpha}{3 \cdot h^2 \cdot \tan^2 \alpha} \quad (3-18)$$

where F_R is the resultant between the lateral (F_L) and normal (F_N) force measured in the test; h is the analysis depth point and β is calculated with equation 3-19:

$$\beta = \alpha + \theta - 90 \quad (3-19)$$

Here θ is the angle between the F_L and F_N force and α , the angle of the face tip inclination (65.27°). Also, if one decides only to solve using α angle, the adhesion strength would be equal to equation 3-20 (see Appendix C):

$$\tau = \frac{\sqrt{3} \cdot (F_T \cdot \cos \alpha + F_N \cdot \sin \alpha) \cdot \cos \alpha}{3 \cdot h^2 \cdot \tan^2 \alpha} \quad (3-20)$$

Additionally, in tribology the wear resistance analysis measures the amount of material removed or displaced (by mechanical action) from a body to another one [90], [91]. In wear analysis some scratch tests are: the pin-on-disk (macro scale) based with the ASTM G99-17, scratch tests tipped stylus (micro scale) from the ASTM G171-03(2009)e2 and ramped load via nanoindentation (nano-scale) [92]. The removed volume or wear is determined by the equation 3-21, where W is the volume of removed material, A is the cross section of the groove that leaves the tip in the material and d , the distance traveled the tip upon testing [91].

$$W = A \cdot d \quad (3-21)$$

For our study and based on the above methodologies, we selected a wear analysis via the ramp-load scratch test using the G200 nanoindenter. The material removed upon the scratch test was calculated from the sketch shown in Figure 3.11 and from which the equation 3-22 was derived:

$$W = \left(\frac{2 \cdot A_{sc} \cdot h \cdot \sin \alpha}{3 \cdot \tan 30^\circ} \right) \quad (3-22)$$

where A_{sc} is the area over the line of the scratch curve (Figure 3.11), h is the maximum depth of penetration, and α is an angle that depends on the geometry of the original Berkovich tip (65.033°) [92].

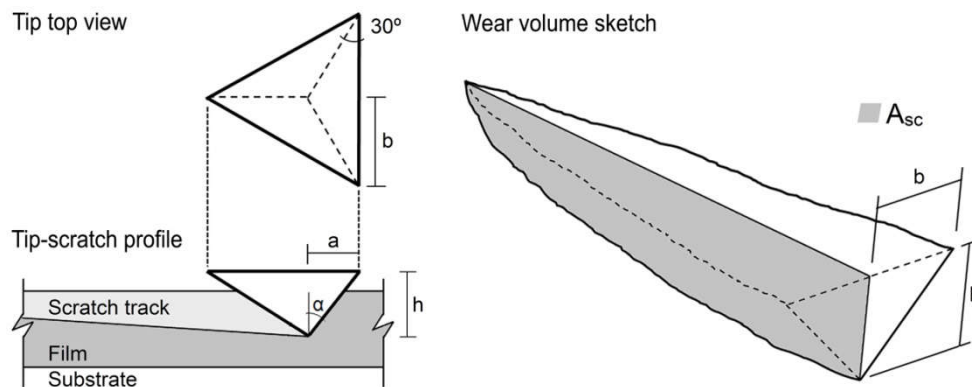


Figure 3.11 Schematic of the wear analysis with the scratch technique via nanoindentation: a ramp load scratch test.

3.3.2 Structural Evaluation

The structural evaluation of the bulk and film materials was completed using an x-ray diffraction unit. In general, this method uses the detection of x-ray diffracted by the

specimen's crystallographic as an incident x-ray beam irradiates the sample. The results are plotted as a spectrum of x-ray intensity versus diffraction angle (2θ). The crystallographic parameters of the materials were computed using the Bragg's law (equation 3-23):

$$\lambda = 2 d_{hkl} \sin \theta \quad (3-23)$$

where λ is the wavelength of the x-ray, i.e. $\text{CuK}\alpha$ (0.154059 nm), d_{hkl} is the interplanar distance and θ is half the angle between the diffracted beam and the original beam. Besides, the lattice parameter a can be calculated for a cubic crystal according to equation 3-24.

$$d_{hkl} = \frac{a}{h^2 + k^2 + l^2} \quad (3-24)$$

where h , k and l are the Miller indices of the planes separated by d_{hkl} . The 2θ angle position is determined from the centroid method of the peak described in appendix D of this thesis [93].

4 EXPERIMENTAL PROCEDURE

4.1 Phase I (Bulk Samples study)

This stage corresponds to the production of deposition targets and samples made of an aluminum-boron master alloy (Al-5wt.% B) using centrifugal casting. To prepare the targets a graphite mold was fabricated to obtain samples of 2.54 mm in radius r , and 2.54 mm in height h , as schematically indicated in Figure 4.1.

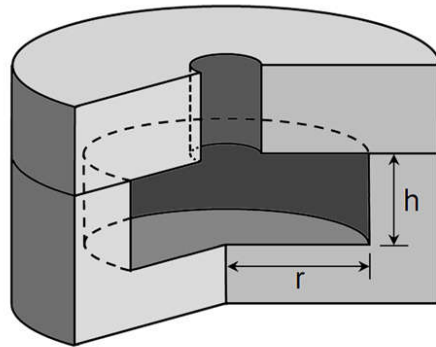


Figure 4.1 Sketch of graphite mold and the cavity necessary for casting the target specimens.

The parameters for the samples production by centrifugal casting process are shown in Table 4.1 and are based on a prior research of an aluminum-silicon-boron composite conducted by Ramos [11].

Table 4.1 Centrifugal casting parameters.

| | |
|--|---------|
| Melting temperature of the aluminum matrix | 650°C |
| Preheated transfer scoop temperature | 400°C |
| Rotation velocity | 350 rpm |
| Preheated mold temperature | 400°C |
| Centrifugation time | 10 min. |

Table 4.2 presents the composition of samples by weight percent content of boron, as well as the specimen name and the amount of material used for casting..

Table 4.2 Composition chart samples by weight.

| Name | Alloy composition | Mass of master alloy Al-5wt.% B (g) | Pure aluminum (g) | Total mass (g) |
|-------|-------------------|-------------------------------------|-------------------|----------------|
| Al-1B | Al-1wt.%B | 44 | 176 | 220 |
| Al-2B | Al-2wt.%B | 88 | 132 | 220 |
| Al-3B | Al-3wt.%B | 132 | 88 | 220 |
| Al-4B | Al-4wt.%B | 176 | 44 | 220 |

4.1.1 Characterization Segment

The structural analysis of the bulk samples allows determining the phases present in the material, i.e. the Al/AlB₂ composite. The techniques used in this analysis were: x-ray diffraction (Siemens D500 x-ray diffractometer using a Cu-K α radiation at 40 kV, and 40 mA) for 2 θ range of 30 to 70 degrees and optical microscopy to produce images of the surface of samples using a Nikon Epiphot 2 inverted optical microscope. To this purpose, the bulk samples were ground on 60, 320, 500 and 1200 grit SiC paper and polished with colloidal silica suspension.

The superficial hardness was assessed via a hardness tester (LECO Rockwell LR-50) using a load of 147 N (15 kgf) and steel ball indenter of 1.588 mm (1/16") in diameter. The Brinell hardness scale was used to report this mechanical property. In addition, a porosity and Rockwell hardness study (ASTM E 18-16) was conducted in the Al-4wt.% B sample to study the centrifugal force effects upon casting.

At the nanoscale, the elastic modulus (E) and hardness (H) were measured with a G200 Agilent Nanoindenter (Figure 3.6) furnished with a Berkovich diamond indenter of 0.01 μ m tip radius. The study included indentations on the matrix, particles, matrix/particles interface to analyze the subsequent interaction in the samples of Table 4.2 (micron- or

submicron size). The method used for this purpose was the continuous stiffness measurement (CSM) using the parameters listed in Table 4.3.

Table 4.3 CSM method parameters.

| | |
|---|----------------------|
| Strain rate | 0.05 s ⁻¹ |
| Frequency | 45 Hz |
| Harmonic displacement | 1 nm |
| Poisson's ratio of the matrix (ν_m) | 0.33 |
| Poisson's ratio of the particle (ν_p) | 0.274 |
| Depth limit | 250 - 400 nm |

4.2 Phase II (Thin Films Study)

The thin film samples were produced via a magnetron sputtering unit using radio frequency. Figure 4.2 shows the magnetron sputtering (AJA International, Inc. ORION-5-HV sputtering system), which was used in films deposition. The system is furnished with three magnetron sputter guns used in direct current (DC) or radio frequency (RF) mode. There are about 10 cm distance in the chamber between substrate and the target guns, whereas the substrate rotation can reach 40 rpm.

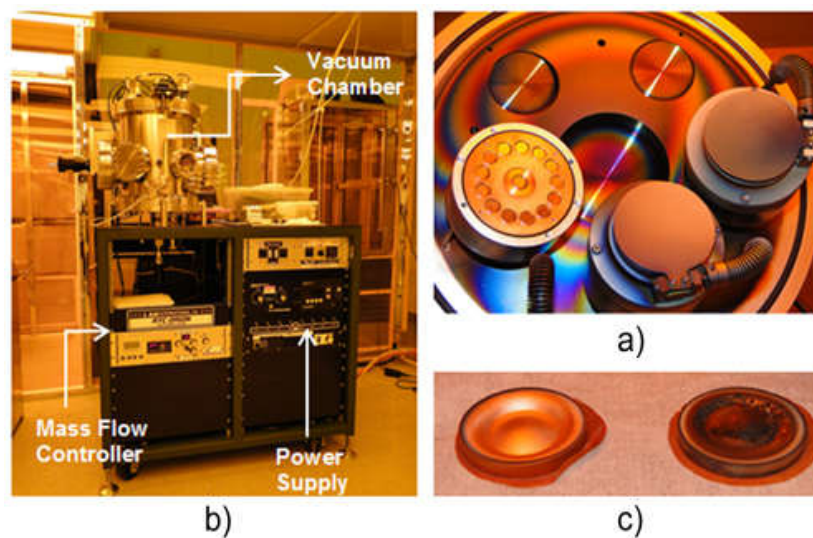


Figure 4.2 a) Three sputtering guns, b) sputtering system, and c) target erosion.

The sputtering was carried out with an argon mass flow of 0.0128 L/min and at a pressure of 2 mTorr in the vacuum chamber; the settings were based in the sputtering of Al-Si-B composite developed by Ramos and Suárez [18].

The set films were manufactured using a deposition time of 120 minutes and a film thickness of approximately 500 nm. Simultaneously, the parameters such as the sputtering power (100, 130, 160 and 200 watts), deposition material (pure aluminum and an aluminum matrix reinforced with AlB_2 particles) and the substrate (glass and single crystal silicon) were varied upon the fabrication to study their effects on the film material.

4.2.1 Characterization Segment

Characterization of the films permitted assessing the film thickness, mechanical properties, surface morphology and crystal structure as functions of the fabrication parameters.

The film thickness was measured with a P6 Profiler from KLA-Tencor. The substrates were prepared with vacuum tape stripes, as shown in Figure 4.3. After sputtering, this tape was removed leaving a deposited material free zone on the substrate.

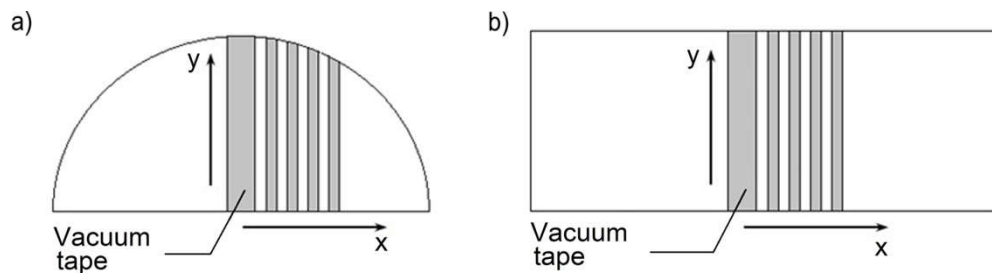


Figure 4.3 Sketch of substrates with vacuum tape: a) silicon wafer and, b) glass slide.

The film elastic modulus and hardness were assessed via nanoindentation using continuous stiffness measurement for thin films method (CSM). The tests were conducted up to 50% of film thickness and in an array of twenty indentations separated by 25 μm . The method was carried out following the parameters in Table 4.4

Table 4.4 CSM parameters used in the thin film method.

| | |
|--|----------------------|
| Strain rate | 0.05 s ⁻¹ |
| Frequency | 45 Hz |
| Harmonic displacement | 1 nm |
| Poisson's ratio of the films (ν_f) | 0.33 |
| Poisson's ratio of the silicon wafer (ν_s) | 0.20 |
| Young's modulus of the silicon wafer | 170.52 GPa |
| Poisson's ratio of the glass slide (ν_s) | 0.24 |
| Young's modulus of the glass slide | 71.261 GPa |
| Depth limit | 50% |

Also, the friction coefficient and the adhesion strength between the film and its substrate were evaluated through the ramp load scratch method using the lateral force value. This method was executed by the G200 nanoindenter (Figure 3.6) using the parameters provided in Table 4.5. The measures were obtained considering the film thickness as a benchmark. In addition, the scratch data allowed completing a wear study with the parameters of table 4.6.

Table 4.5 Parameters for the ramp load scratch using lateral force.

| | |
|--------------------|--------------------|
| Length | 150 μm |
| Scratch velocity | 20 $\mu\text{m/s}$ |
| Maximum load | 30 mN |
| Post/pre length | 20% |
| Profiling load | 50 μN |
| Profiling velocity | 10 $\mu\text{m/s}$ |

Table 4.6 Parameters for the ramp load scratch using lateral force for the wear study.

| | |
|--------------------|--------------------|
| Length | 150 μm |
| Scratch velocity | 20 $\mu\text{m/s}$ |
| Maximum load | 10 mN |
| Post/pre length | 20% |
| Profiling load | 50 μN |
| Profiling velocity | 10 $\mu\text{m/s}$ |

The film morphology analysis included the surface roughness, grain size and hillock growth. The images of the topography of samples were captured by an atomic force microscope (AFM-Veeco, Model di CPII AP0100, operating in no contact mode). AFM images were acquired by scanning onto the surface with a sharp probe that monitored and assembled the tip/sample interactions to generate an image. In other words, each image is created by quantifying the forces between the probe (cantilever tip) and the sample surface. The film surface areas scanned were 625, 100, 25, 9, and 2.25 μm^2 . Afterwards the images were examined using the SPIP[®] software from Image Metrology.

The crystal structure of the films material was evaluated from the diffraction patterns obtained in a Rigaku ULTIMA III diffractometer with cross beam, optics and a Cu $K\alpha$ target operating at 40 kV and 44 mA for 2θ range of 30 to 70 degrees and a wavelength of 0.15418 nm.

Since in many applications these films are exposed to high temperature [94], it is mandatory to study the mechanical properties as a function of temperature. Therefore, nanoindentation experiments on a hot stage were performed on the aluminum and Al-4B film deposited over silicon wafer at a sputter power of 200 watts. The method used in test was the hot stage hardness and modulus (HS-HM) executed with the parameters

of Table 4.7. Both hardness and elastic modulus were determined at an approximate depth of 300 nm as the film were at 28°, 75°, 100°, 150°, and 180°C. Subsequently, at room temperature when the sample was cooled.

Before the experimentation, the equipment was calibrated via the frame-stiffness calibration method for a given temperature range in the reference sample (fused silica). Then, test results were adjusted by means of a graphical method to produce the frame-stiffness correction values (Table 4.8). Additionally, the film crystal structure was studied via in-situ high temperature X-ray diffraction (HT-XRD) technique from Rigaku ULTIMA III machine using Reactor X module, at temperatures of 28°, 200°, and 400°C. Then at room temperature (28°C) after the heating cycle.

Table 4.7 Hot stage parameter test.

| | |
|----------------------|--------|
| Percent to unload | 90% |
| Peak hold time | 1s |
| Time to load | 1s |
| Allowable drift rate | 5 nm/s |

Table 4.8 Frame stiffness correction.

| Temperature (°C) | Frame stiffness correction |
|------------------|----------------------------|
| 28 | 1500000 |
| 75 | 700000 |
| 100 | 500000 |
| 150 | 20000000 |
| 180 | 1000000 |

5 RESULTS AND DISCUSSIONS

5.1 Bulk Samples Study

The aim in this section was to study in the bulk samples the distribution of the reinforcing particles (AlB_2) in the aluminum matrix upon fabrication. It also sought to discover how this distribution affected the mechanical properties of the material as a function of the amount of reinforcement.

The as-centrifuged samples had the chemical compositions indicated in Table 4.2. In these specimens, the microstructure was analyzed using x-ray diffraction and optical microscopy, whereas some mechanical properties were assessed via hardness test (macroscale) and nanoindentation (nanoscale).

5.1.1 Microstructure Analysis

The resulting XRD patterns of the samples are presented in Figure 5.1, which includes the crystallographic planes of the constituents of the material. The peak at $2\theta = 34.51^\circ$ reveals the AlB_2 particles presence according to the crystallographic plane (100), which matches the $2\theta = 34.41^\circ$ angle defined by the AlB_2 powder diffraction (JCPDS 39-1483). Similar results were found in master alloys studies [95], [46] and in an Al-B-Si composite that likewise reported the presence of AlB_2 phase for 2θ angle of 34.414° [18].

Furthermore, in this same figure two main peaks can be identified at 38.565° and 44.816° . They matched with the aluminum phase according to the powder diffraction standard JCPDS 04-0787 for the crystallographic planes (111) and (200), respectively.

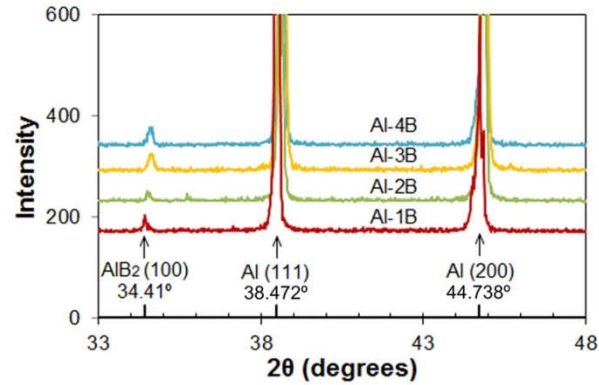


Figure 5.1 Characteristic peak in the Al-xB castings.

Figure 5.2 displays the microstructure of Al-4wt. %B composite (Al-4B). In this picture, the magnified section presents rectangular and hexagonal shape of the particles embedded in the aluminum matrix. As previously mentioned, the AlB₂ particles have an hp3 crystal structure (section 3.1.1) and the different observed shapes are likely due to different sections of the hexagonal structure (Figure 3.1). Similar AlB₂ shapes in optical microscopy were reported in other studies [6], [13], [46], [50], [96] .

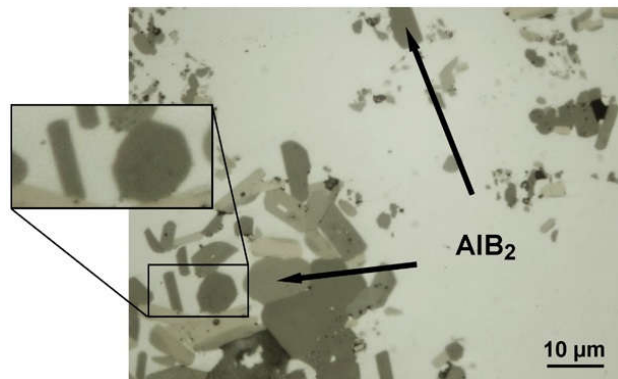


Figure 5.2 Micrographic image of Al-4B composite sample.

Therefore, the shape of the particles in the microstructure depends on the exposed crystallographic plane section, which resulted from the metallographic preparation of the specimen [13]. In effect, Melgarejo et al. graphically explained the possible AlB₂

particles shape in the microstructure of an Al-B composite according to the crystallographic plane orientation, as shown in Figure 5.3. The particle section may be hexagonal for a $\phi = 0^\circ$, rectangular for a $\phi = 90^\circ$ and intermediate shapes for other angles.

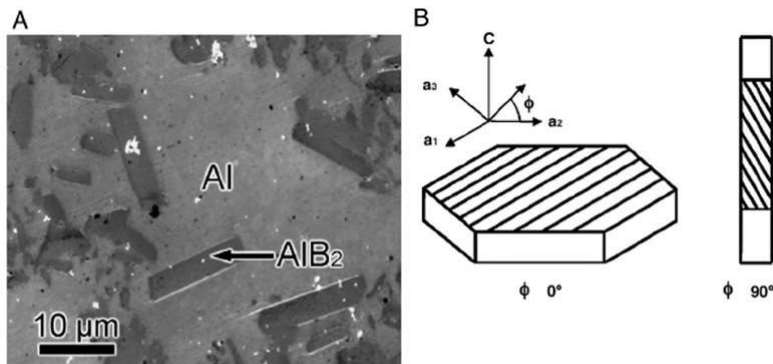


Fig. 1 – Microstructure of Al/AlB₂ composite and crystal structure of its reinforcement particle: (A) SEM image of the microstructure of a Al-5 wt.%B master alloy; (B) crystal structure of the AlB₂ particle oriented $\Phi=0^\circ$ (hexagonal face of a particle with the c-axis perpendicular to the particle surface) and $\Phi=90^\circ$ (rectangular particle with a c-axis parallel to the sample surface).

Figure 5.3 Al-5wt.%B microstructure and AlB₂ particle orientation planes (Reprinted from ref [13] by permission)

Moreover, the microstructure was analyzed with an 10x objective lens in order to have a general overview. Figure 5.4 shows the microstructure of samples obtained from the outer zone of the centrifuged castings. In these images, the pores (black dots), particle cluster (gray dots) and the matrix (background) can be readily identified. Also, the pictures reveal that the particle amount in each sample is directly related to the boron content in the composite, as expected (Table 4.2). For instance, the microstructure of Al-4B sample presents greater presence of particles in the matrix (Figure 5.4d). As mentioned, the boron percent depends linearly on the amount of AlB₂ particles [6].

In addition, the images show a proper dispersion of AlB₂ particles in the aluminum matrix. All things considered, the results of XRD, optical microscopy and cited literature

corroborated that Al-xB composites contain AlB_2 particle reinforcements embedded in the aluminum matrix; this means that no other boride phase formed upon processing.

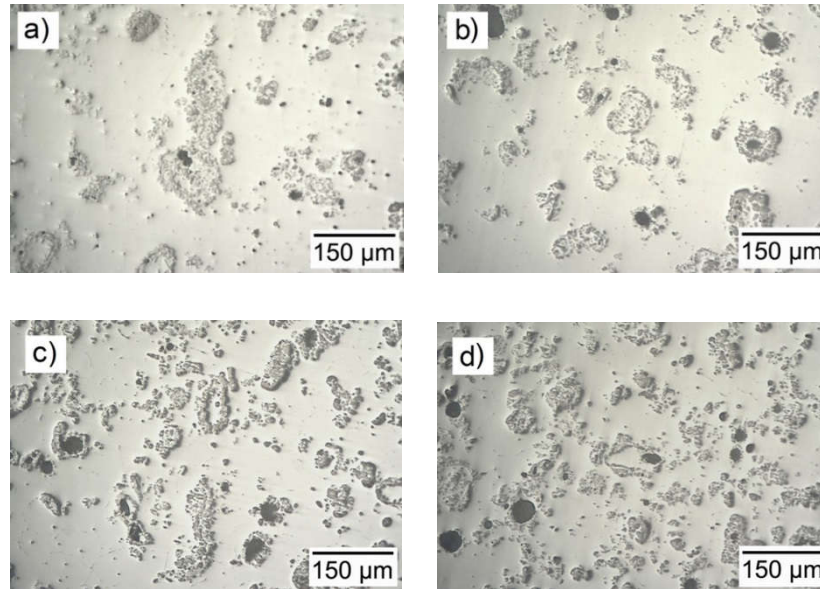


Figure 5.4 Particle distribution within bulk samples: a) Al-1B, b) Al-2B, c) Al-3B and, d) Al-4B.

5.1.2 Mechanical Property

Brinell hardness (HB) values were calculated using equation 3-1. The hardness results are shown graphically in Figure 5.5 as a function of boron weight percent (Table 4.2). In this figure, the hardness rises with increasing boron content in the casting, as a result of reinforcement particles present in the material (Figure 5.2). Hence, these results demonstrated the effect that the particles have in the mechanical behavior of the composite [1], [41]. It is well known that the hardening effect of the particles in the matrix is due to the interaction between both phases in the composite [2], [39], [97].

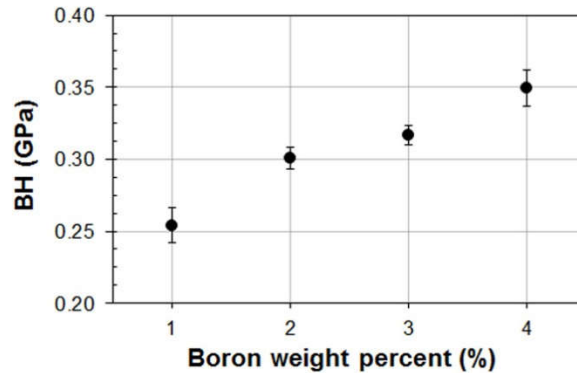


Figure 5.5 Increasing boron levels raise the Brinell hardness (BH).

5.1.3 Centrifugal and Gravity Casting Analysis

In this section, the Al-4wt.% B composition was selected to study the effects of type casting in the cast material. The porosity and hardness were analyzed in the manufactured samples via gravity casting and centrifugal casting.

The porosity was determined using a micrograph image analysis using ImageJ public software on pictures taken with an invert optical microscope (Nikon Epiphot 2) and Rockwell hardness was evaluated considering the ASTM E 18-16.

Figure 5.6 shows an example of a micrographic picture analysis before and after processing. The software calculates the black area percentage (Figure 5.6b) and the porosity result is the difference between this value and the total area of the image.

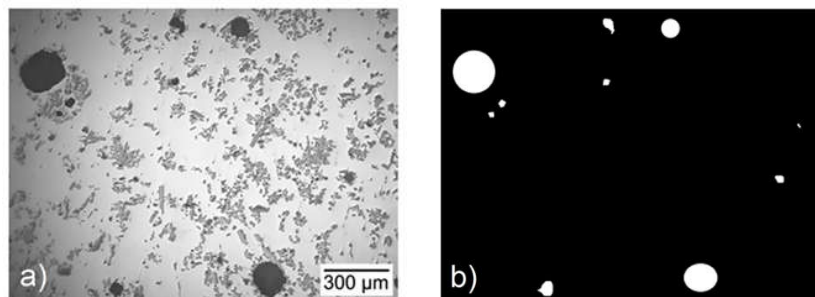


Figure 5.6 Analysis using ImageJ: a) original picture, and b) processed image.

The results of porosity and Rockwell superficial hardness (RH) were compared in the same graph (Figure 5.7). One can observe that centrifugal casting helped reduce the porosity in the microstructure, which is reflected in the overall RH results when compared to the gravity casting process. Fewer pores generate larger resistance to indentation upon hardness testing. We attribute the pores to gas or air entrapment mostly upon fabrication of the master alloys; they may also be due to shrinkage during solidification [98]. Therefore, these defects in the microstructure (pores) may affect the mechanical behavior of material, because they would favor failure [99], [100].

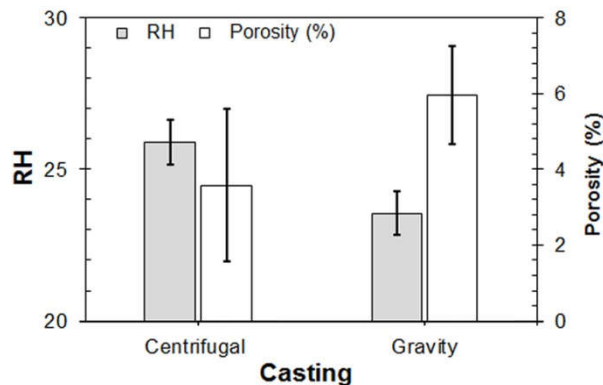


Figure 5.7 Porosity and Rockwell superficial hardness.

The lower porosity observed in the centrifuged sample was likely caused by the speed at which the material enters the mold and ejects the air in the chamber quickly avoiding that air stays trapped in the cast as well as the centrifugal forces acting preferentially on the more dense (liquid) phase (compared to the gas filled pores). Furthermore, in the centrifugal casting the molten material enters and fills the chamber via a spiral motion before solidifying (Figure 5.8b). Hence, this phenomenon is also reducing the voids (pores) in the material due to the stirring generated. However, when there is high stirring, it facilitates the entrapment of air or gas in the casting [99].

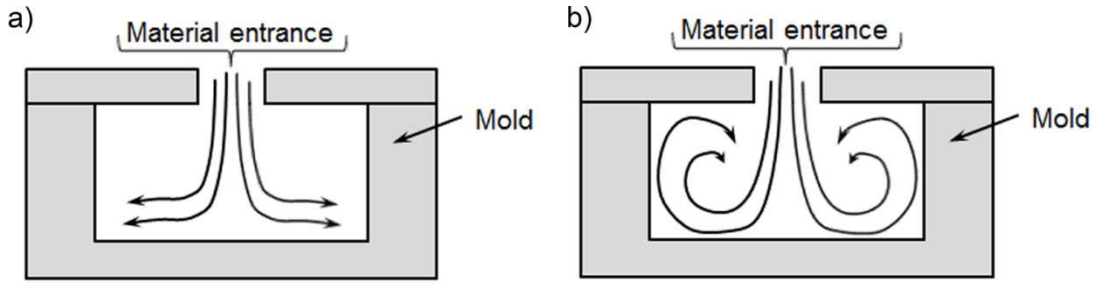


Figure 5.8 Mold section and the material entrance chamber: a) gravity casting, and b) centrifugal casting.

Additionally, this behavior was analyzed via a hardness mapping in three sections along the main axis in the casting pieces (Figure 4.1). Figure 5.9a shows a sketch of how each centrifuged ingot was sectioned for the three analysis distances (normalized); Figure 5.9b depicts the hardness results at those distances. The changes in RH along those sections are the result of the particle segregation caused by the centrifugal force and the density difference between the liquid matrix and particle; this produces a functionally graded material (FGM) [4], [51], [3]. This same behavior (FGM) was found in aluminum matrix composites produced via centrifugal casting [7], [6], [10], [101]. Therefore, both the lower porosity and increasing particle segregation produces a strength gradient in the same direction as the centrifugal force.

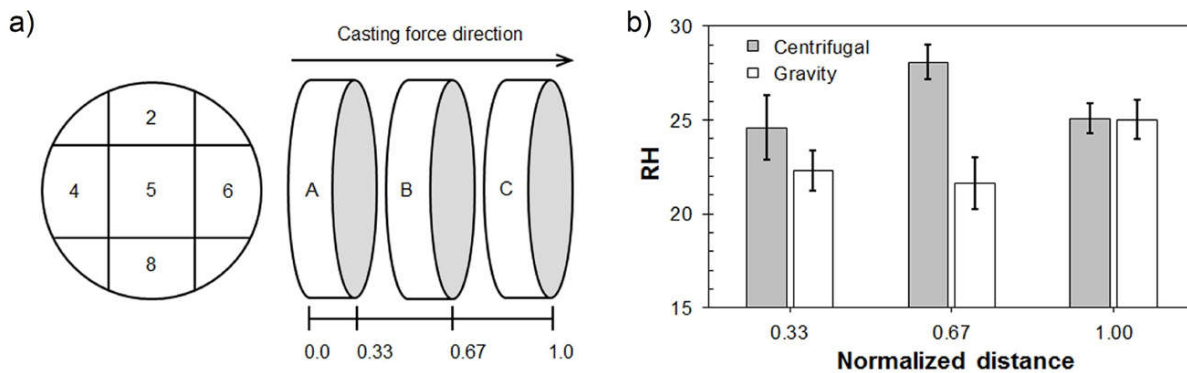


Figure 5.9 Rockwell hardness (RH) analysis: a) section sample and, b) results hardness in normalized distance.

5.1.4 Nano-mechanical Properties

The effect of the AlB_2 particles within the aluminum matrix was studied in Al-B composites via nanoindentation for better understanding of the mechanism of improvement of mechanical properties at the macro-scale [1], [2], [41]. The elastic modulus and hardness were determined with the continuous stiffness measurement method (CSM) conducted into specific areas of the composite microstructure. The samples were analyzed starting an array of fifteen separate indentations of 10 microns, as seen in the micrographs in Figure 5.10.

Figures 5.10 and 5.11 present the nanoindentation measurements as a function of the indentation depth (displacement from the surface) for the studied compositions (Table 4.2). In these figures, we have been able to identify three different mechanical behaviors in the microstructure of the samples which are related to the matrix and the AlB_2 particles as well as one intermediate behavior (transition). In the latter, the penetrator could have impacted a particle that was under the metal surface, which may have caused this irregular behavior.

The results in the matrix were determined at a depth of 100 nm, because from this depth the CMS method began to generate consistent, reliable data (Figure 5.10 and 5.11); it presented similar values for both the elastic modulus and hardness for each studied composition (80 GPa and 0.70 GPa, respectively). Therefore, these findings demonstrate that the boron content in the samples did not affect the aluminum matrix mechanical properties, which was somewhat unexpected. In effect, some authors had indicated by theoretical means, that the particles in any order can harden and

strengthen the metal matrix as a result of the increased dislocation densities caused by the difference in thermal expansion coefficients of the constituents when the material is fabricated. This could generate residual stresses or stress concentration in and nearby the interface [102], [103]. Additionally, studies of aluminum matrix composites (Al-Mg-B, Al-SiC) using micro-indentation tests found this same tendency with respect to matrix hardening as a function of the volume fraction of particles in the material [104], [6]. Also, via the nanoindentation technique Rodriguez et al. who studied a matrix of 8090 Al-Li reinforced with SiC particles observed that the hardness in the metal matrix was larger in this composite compared to unreinforced material [12]. Similarly, via nano-mechanical characterization in an Al-Si-B composite, Ramos and Suárez found similar results in the hardening of the aluminum matrix [18]. They attributed this effect to the particles and to the eutectic silicon present in the composite. However, in these works, the methods used for determining the hardness took into account the maximum load applied during the test. This means that these methods did not consider the possible presence of particles below the indentation, which can generate a resistance that increased the matrix hardness. Chawla and Chawla illustrated this with a finite elements model of an indentation made on a homogeneous material and in a composite. Their findings revealed that in the composite model, the particles present underneath the indenter induced less deformation upon the indentation [41].

Considering this finding, the transition behavior of the elastic modulus and hardness of the samples, observed graphically is consistent with the response of the material due to these particles that likely are found underneath or around a given indentation (Figure 5.10 and 5.11).

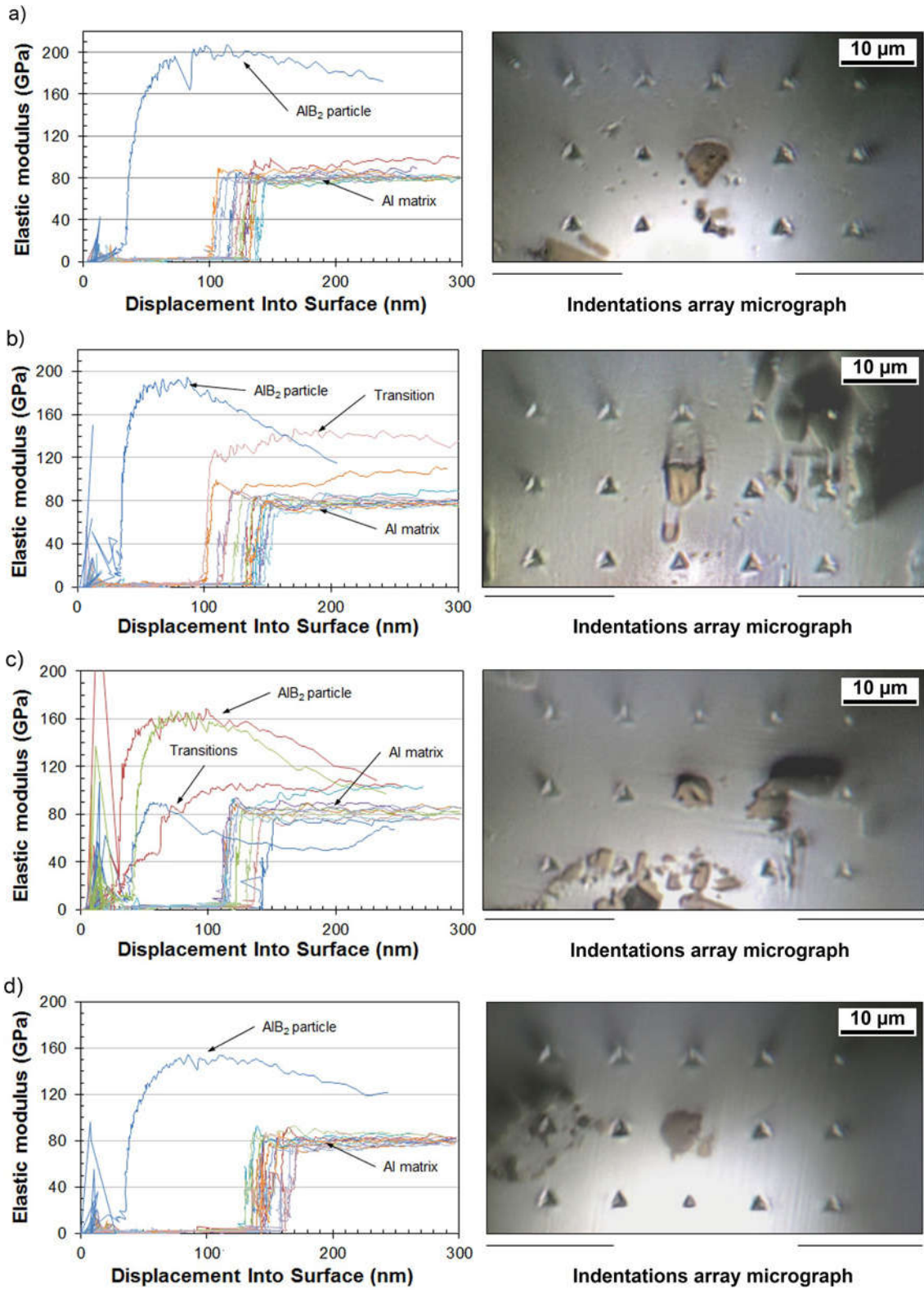


Figure 5.10 Elastic modulus and (left column) and indentation micrographs (right column) on bulk samples: a) Al-1wt.%B, b) Al-2wt.%B, c) Al-3wt.%B and, d) Al-4wt.%B.

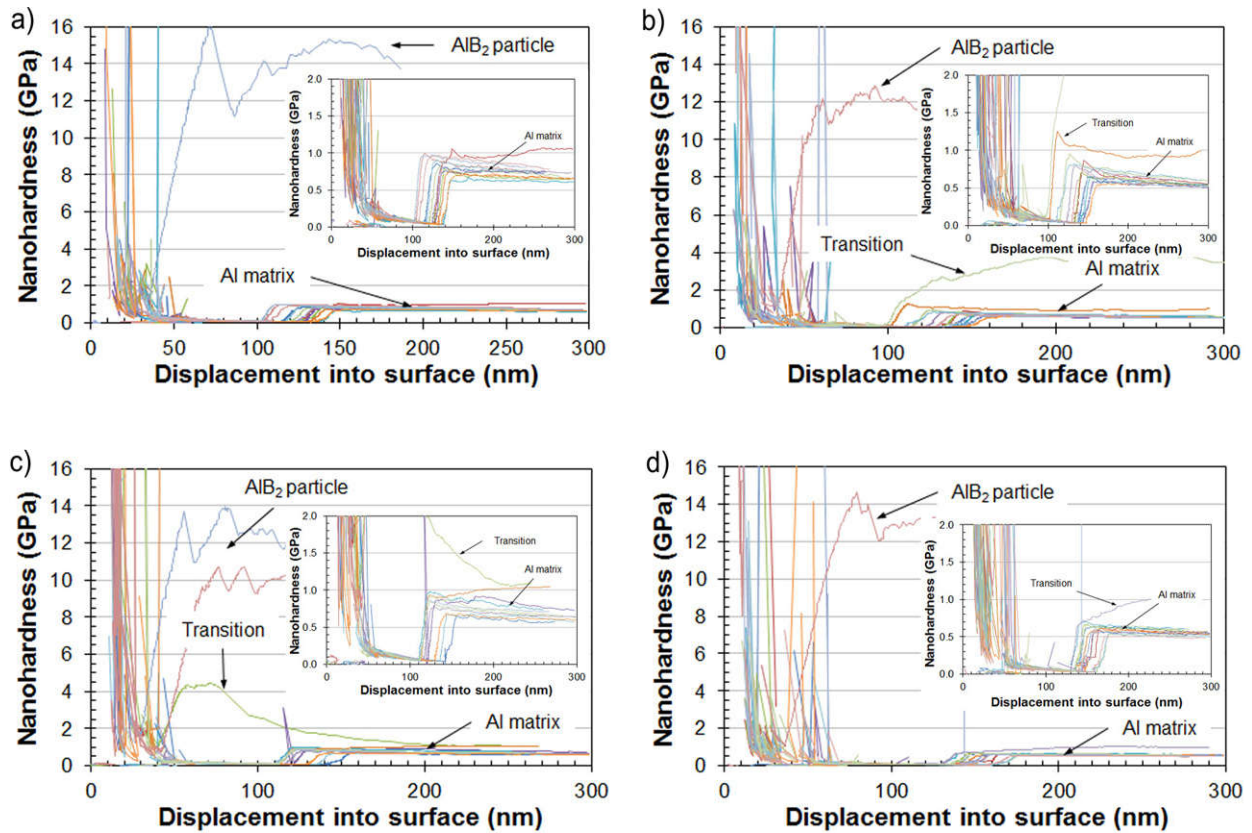


Figure 5.11 Evaluated nanoindentation in bulk samples: a) Al-1wt.%B, b) Al-2wt.%B, c) Al-3wt.%B and, d) Al-4wt.%B.

As a consequence of these results, other set of indentations were carried out over a particle cluster in the Al-1B sample seeking to reveal whether the mechanical behavior varied around those particles. The elastic modulus results and the indentation micrograph can be seen in Figure 5.12. In this figure, once again the same three behaviors were detected (matrix, particle and transition). Therefore, the indentations were labeled and some of these were selected to perform an individual discussion of each behavior, as follows:

In the matrix case, the indentations 04, 15 and 23 that are relatively close to the particles were selected for further analysis (Figure 5.12). The elastic modulus measured

was approximately 80 GPa (Figure 5.13a) and maximum applied indentation load was 2.2 mN (Figure 5.13b). Again, the result of elastic modulus in the metal matrix of this sample showed no change and was similar to the results shown in Figure 5.10 for the studied compositions.

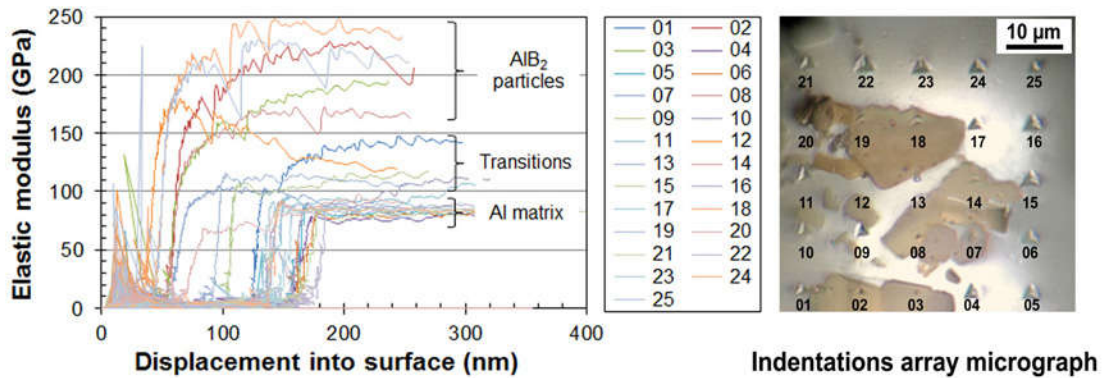


Figure 5.12 Elastic modulus (left) and indentations micrograph (right) in Al-1wt.%B (Al-1B) around of particles group.

Now, the transition behavior is depicted in the indents labeled with numbers 01, 10 and 13. In these indents, the elastic modulus value is zero at the beginning of the test, and later, the nanoindenter records a value at 90 nm, as can be seen in Figure 5.13a. However, this value throughout the test is not constant, because it depends on the homogeneity of the material below or around the indenter tip in the tested area. In the case of the indent 10, the elastic modulus is constant for the 150 - 200 nm range as in the matrix (80 GPa); then it grows to 115 GPa. At higher than 200 nm depth, the indenter tip perhaps entered in contact with one side of the particle, which resulted in a change in the response of material during the indentation; at that moment the material ceases to be homogeneous. One must also recall that the properties obtained via nanoindentation depend on the contact area between the material and the tip (Section 3.3.1). Yuan et al. reported this kind of contact between the tip and a particle in the

indentation by observing the load-displacement curve, as it presented a slope change in the loading stage at the end of the test [105]. At the contact point the indenter instrument increased the load to overcome the resistance of the heterogeneity of the material thus reducing the depth of indentation compared to the matrix.

For the indentation number 13, the result is similar to the constant behavior in the matrix, although the value of the elastic modulus was approximately 120 GPa. In the micrograph, it is apparent that this indentation lied in the matrix/particle interface (Figure 5.12). In this situation, the particle and the matrix maintained their integrity in the deformations fields (composite action), consequently this increases the material strength. Namely, the magnitude of the displacement of the constituent phases of the composite was the same, which contributed locally on the displacement resistance when it was pressed by the indenter tip [41]. Hence, the load transfer between particle and matrix is optimal.

Finally, we studied the behavior defined by the indent number 19, which corresponded to an indentation on a reinforcing particle (Figure 5.12). The property measurement started after 50 nm of depth at 160 GPa and grows nonlinearly to a value of about 230 GPa, as shown in Figure 5.13a. The maximum elastic modulus obtained in the AlB_2 particle is lower than the 250 GPa value reported by the literature [48], [52], because in this case the measured property is relative to the matrix/particle system (composite) and it is not the result of a pure material. In Figure 5.13b, curve 19 has three steps in which the load remains relatively constant, but the depth of the indentation in the sample continues to increase. Interestingly, in those steps the elastic modulus drops sharply and then grows towards the value measured via a continuous testing without steps

(Figure 5.13a). The steps found in the load curve may be caused by the loss of support at the interface due to slipping between the matrix and the particle by the effect of the shear stresses generated at the matrix/particle interface that caused the pushing-in of particle into matrix. This phenomenon was researched by Mahato et al. in an Al-Si alloy reinforced with silicon particles via micro-indentation [106]. Experimentally they observed that the plasticity in the contact area during the indentation is more critical in the larger particles by the surface to volume ratio with respect to the buried particle depth in the matrix, which facilitates the sinking. Likewise, Melgarejo et al. studied this phenomenon in an Al-B composite via nanoindentation using the strain gradient plasticity theory. In this case the experimental methodology used was by cycle load control with 4 load segments on different AlB₂ particle sizes, embedded in the aluminum matrix [13]. The theory allowed them to determine the yield pressure (Y_p) in the area below the particle surrounded by the matrix. The Y_p findings found were larger in small particles in contrast to larger particles. Accordingly, the small particles have a greater resistance to sinking (push-in) into the matrix, as revealed by the experimental results.

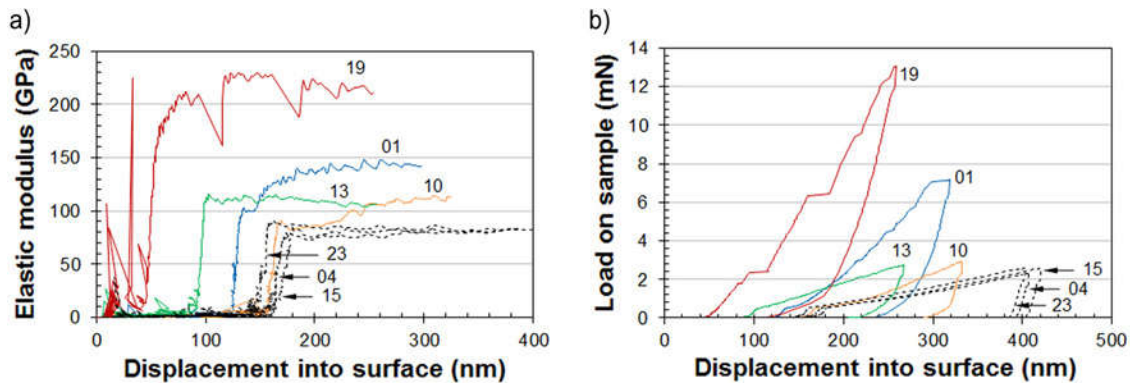


Figure 5.13 Nanoindentation results of particle cluster analysis in an Al-1B sample.

After having discussed the different mechanical behaviors found in the composite by the CSM method and compared it with the literature we produced a three-dimensional model (using Matlab) of the experimental elastic modulus results to survey the material performance in the studied area. Figure 5.14 shows the elastic modulus distribution for each composition where we can identify the matrix (blue), the particle (red) and matrix/particle interface (color gradient) according to the experimental results.

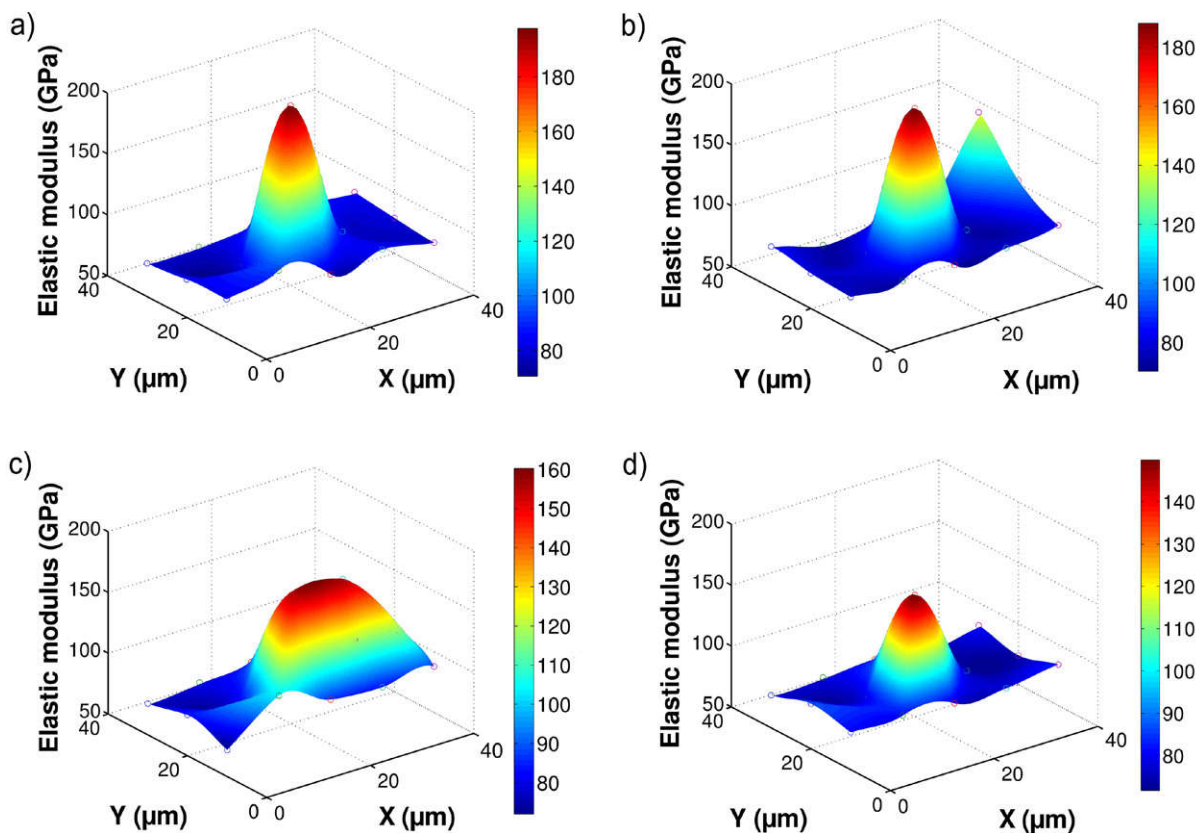


Figure 5.14 Mapping of the elastic modulus in composite samples: a) Al-1wt. %B, b) Al-2wt. %B, c) Al-3wt. %B and, d) Al-4wt. %B.

In summary, the continuous stiffness measurement via nanoindentation permitted us to determine that the properties of the pure Al matrix in this composite have not been affected by the particle amount, contrary to what the literature previously stated [11], [12]. Furthermore, with our methodology we observed that the properties are changing

as the indentation is in progress as a result of particles within the matrix or on the sides of the indenter tip [13], [41], [105], [106]. The findings and the Matlab simulation helped us to understand via local behavior study in the microstructure that the overall response of Al-B material to macro-scale by mechanical testing is directly related to the matrix/particle interaction [2], [39], [97].

5.2 Thin Films Study

The study of thin films focused on the Al-4wt. %B (Al-4B) composite as deposition material, since this one, as shown in the previous section, presented the best mechanical and microstructural performance in bulk samples.

The thin films were manufactured using magnetron sputtering where the film thickness, mechanical properties, morphology and crystal structure were studied using several characterization techniques. The analyses centered on the effects of deposition time, sputtering power, material and the substrate nature.

5.2.1 Profilometry Analysis (film thickness)

The films thicknesses were measured on samples deposited to a sputtering time of 120 minutes, four sputtering power levels (100, 130, 160 and 200 watts) and two substrates: glass slide (GS) and silicon wafer (SW). Figure 5.15 shows the result of the profile measured using the KLA-Tencor profiler on a sample prepared according to section 4.22. In this figure, the observed groove depth (between 1000 and 500 nm in the Y axis) determines the film thickness. In addition, the two peaks seen in the figure occurred upon lifting the material when the vacuum tape was removed from the sample after film sputtering.

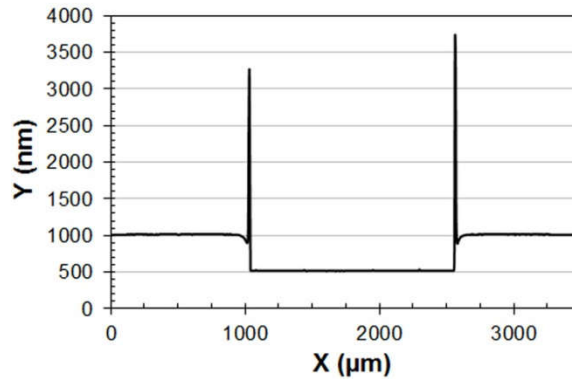


Figure 5.15 Profilometry in Al-4wt.%B sample.

The profilometry results are summarized in Tables 5.1 and 5.2, and plotted as a function of the sputtering power in Figure 5.16. This figure demonstrates how the film thickness increases with sputtering power in the two studied materials. Also, the aluminum films turned out thicker than films manufactured with the Al-4B composite for similar deposition parameters. In addition, in this same figure one can observe that the aluminum curves identified as Al(GS) and Al(SW) tend to overlap, i.e. the film thickness was not affected by the substrate nature. This reveals that between the material and substrate a repulsion phenomenon was not present to affect the film growth [107], [108], [32], [89]. Likewise this occurred in the Al-4B films.

The observed difference between the thickness of the aluminum films and the Al-4B films can be attributed to the deposition rate (d_r) of the target material, which in turn is linked to the sputtering yield (S). This sputtering yield is defined as the quantity of ejected atoms per ions incident of the plasma (Ar^+). Incident ions change with the sputtering power according to the literature [53]–[55], [109], [32]. The aluminum is a soft material and the literature has reported that its sputtering yield is high when compared to other materials [53], [55], [110]. Hence, the lowest d_r values calculated for the composite target (Al-4B) showed that atoms ejection is more difficult (Tables 5.1 and

5.2), because bonds are stiffer than in aluminum (hardness results in section 5.1.2). Moreover, this composite, being a heterogeneous material, may be generating enhanced difference of sputtering yield due to the different nature of aluminum and AlB₂ phases present in the free surface of the target (Figures 5.2 and 5.3). In other words, the sputtering of Al-4B composite perhaps is behaving similarly to the sputtering of alloys, which reduces the amount of sputtered material on the film. In these cases, the material concentration (C) and flow ratio (ψ) depend on the present phases in the surface target and are given by equations 5-1 and 5-2:

$$C_{x,y} = \frac{n_{x,y}}{n} \quad (5-1)$$

$$\frac{\psi_{x,y}}{\psi_{y,x}} = \frac{S_x \cdot C_x}{S_y \cdot C_y} \quad (5-2)$$

where $n_{x,y}$ are atoms number of each phase, n is the sum of the atoms of x and y , S is the sputtering yield and C is the alloying element concentration.

This possible sputtering process was first revealed by Ramos and Suárez via scanning electron microscope (SEM) using a Al-B-Si composite target to sputter thin films using current direct as power source [18]. After several sputtering experiments, they observed the target in a SEM and found that its surface presented larger erosion in the aluminum matrix than in the boride particles as consequence of the sputtering preference due to the sputtering yield difference in the composite material.

In conclusion, the differences found in the film thicknesses of the two study materials in this research have a particular relationship with the material itself.

Table 5.1 Summary thickness with aluminum.

| Substrate | Glass slide (GS) | | | | Silicon wafer (SW) | | | |
|-----------|------------------|-------------------|--------------------|--------------------------|--------------------|-------------------|--------------------|--------------------------|
| | Sputtering power | Average thickness | Standard deviation | Coefficient of Variation | Deposition rate | Average thickness | Standard deviation | Coefficient of Variation |
| (watts) | \bar{t} (nm) | σ | C_V (%) | d_R (nm/s) | \bar{t} (nm) | σ | C_V | d_R (nm/s) |
| 100 | 427.55 | 29.32 | 6.858 | 0.059 | 411.51 | 7.26 | 1.765 | 0.057 |
| 130 | 559.46 | 9.80 | 1.752 | 0.078 | 545.00 | 18.53 | 3.401 | 0.076 |
| 160 | 668.54 | 5.16 | 0.771 | 0.093 | 667.73 | 6.43 | 0.964 | 0.093 |
| 200 | 832.94 | 12.93 | 1.553 | 0.116 | 828.02 | 12.92 | 1.561 | 0.115 |

Table 5.2 Summary thickness with Al-4B.

| Substrate | Glass slide (GS) | | | | Silicon wafer (SW) | | | |
|-----------|------------------|-------------------|--------------------|--------------------------|--------------------|-------------------|--------------------|--------------------------|
| | Sputtering power | Average thickness | Standard deviation | Coefficient of Variation | Deposition rate | Average thickness | Standard deviation | Coefficient of Variation |
| (watts) | \bar{t} (nm) | σ | C_V (%) | d_R (nm/s) | \bar{t} (nm) | σ | C_V (%) | d_R (nm/s) |
| 100 | 358.87 | 31.97 | 8.909 | 0.050 | 357.31 | 7.04 | 1.971 | 0.050 |
| 130 | 477.96 | 05.03 | 1.053 | 0.066 | 480.87 | 9.20 | 1.913 | 0.067 |
| 160 | 600.98 | 28.37 | 4.721 | 0.083 | 604.04 | 3.28 | 0.543 | 0.084 |
| 200 | 737.48 | 04.84 | 0.656 | 0.102 | 741.76 | 4.63 | 0.625 | 0.103 |

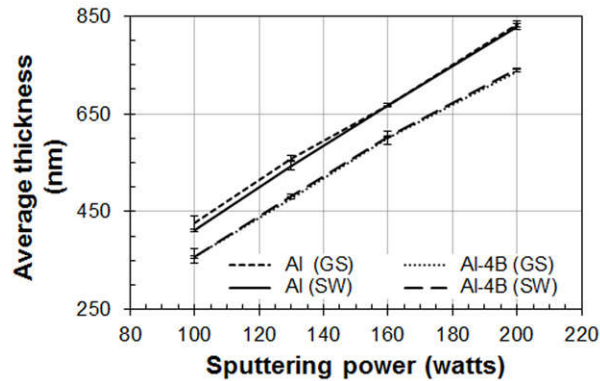


Figure 5.16 Thickness as a function of sputtering power.

Additionally, the variation of the film thickness of each sample on both substrates (glass slide and silicon wafer) was analyzed in a $118.75 \cdot 10^6 \mu\text{m}^2$ to assess the surface evenness because the sputtering process can affect such characteristic of the layer [32], [109]. Hence, the surface thickness of each sample was depicted as level curves

for both materials as a function of the sputtering power and the substrate nature in Figures 5.18 and 5.19 for the aluminum films and Figures 5.20 and 5.21 for the composite (Al-4B). The contour plots show the variability of the thickness surface at the micro scale in the study area.

Accordingly, this variability was analyzed by the coefficient of variation (C_V), which is a dimensionless statistic parameter that allows us to define the homogeneity of a series of data with respect to the mean value and compare it with others [111], [112]. In our case, the film surface uniformity is with respect to thickness. The lower calculated values of C_V in the samples were 0.543 and 0.625 and were obtained in the composite (Al-4B) deposited at 160 and 200 watts, respectively, on a silicon wafer. Regarding this parameter, the lower value would be an indicator of uniformity in the film thickness at this material.

The observed smoothness of the deposited surface (Figure 5.21) can be associated to a progressive growth type Frank-Van der Mayer (Figure 5.17a), which extended up to the macro scale. Growth occurred by layers as a result of the strong bonding between the deposited material and the substrate. Consequently, the substrate and material may be having a better affinity to reduce the interface tension (γ) in the interface (γ_i) reflecting in a uniform growth of the film

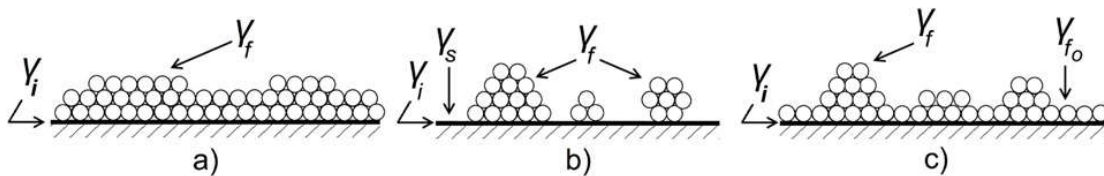


Figure 5.17 Film growth types: a) layer (Frank- Van der Mayer); b) island (Volmer-Weber; c) Stranski-Krastanov [32].

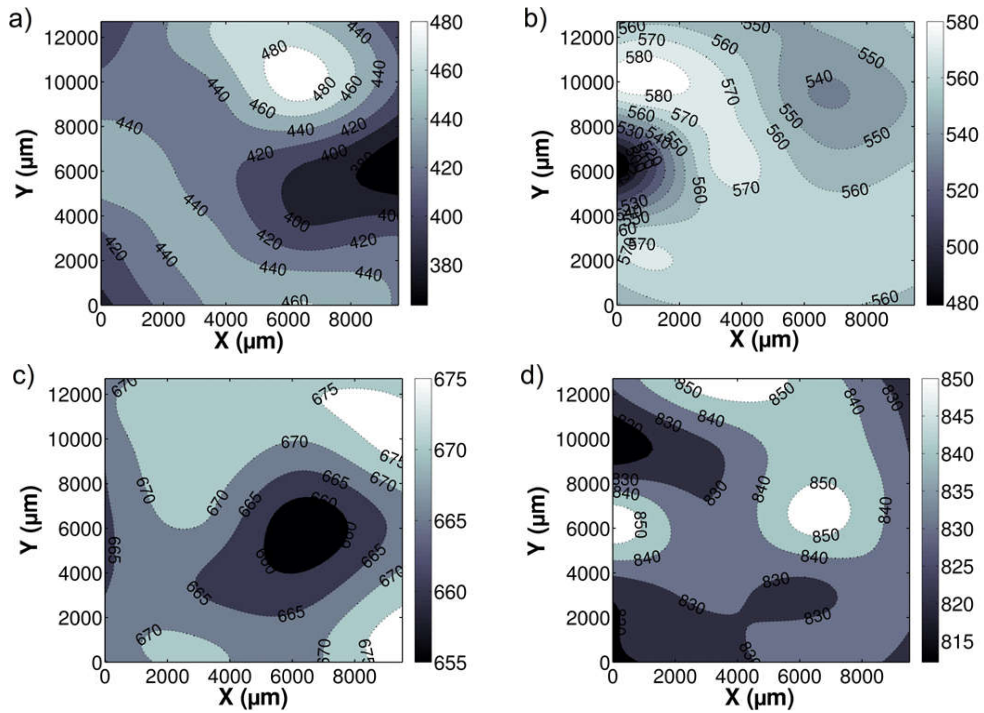


Figure 5.18 Contour plots of film thickness in aluminum over glass slide deposited at: a) 100, b) 130, c) 160 and, d) 200 watts of sputtering power.

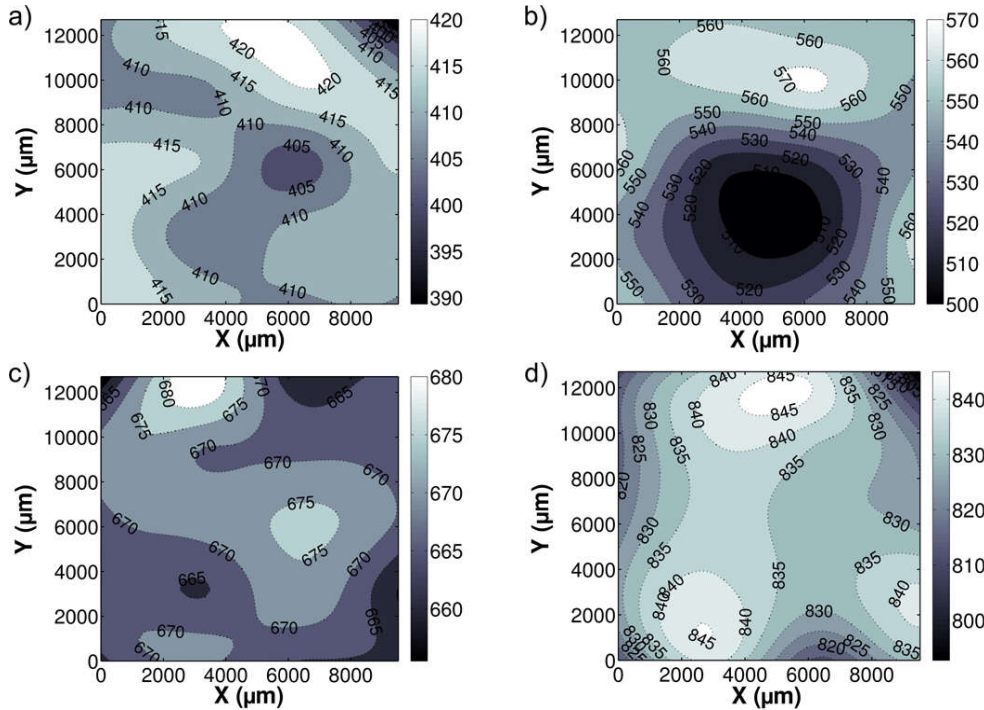


Figure 5.19 Contour plots of film thickness in aluminum over silicon wafer deposited at: a) 100, b) 130, c) 160 and, d) 200 watts of sputtering power.

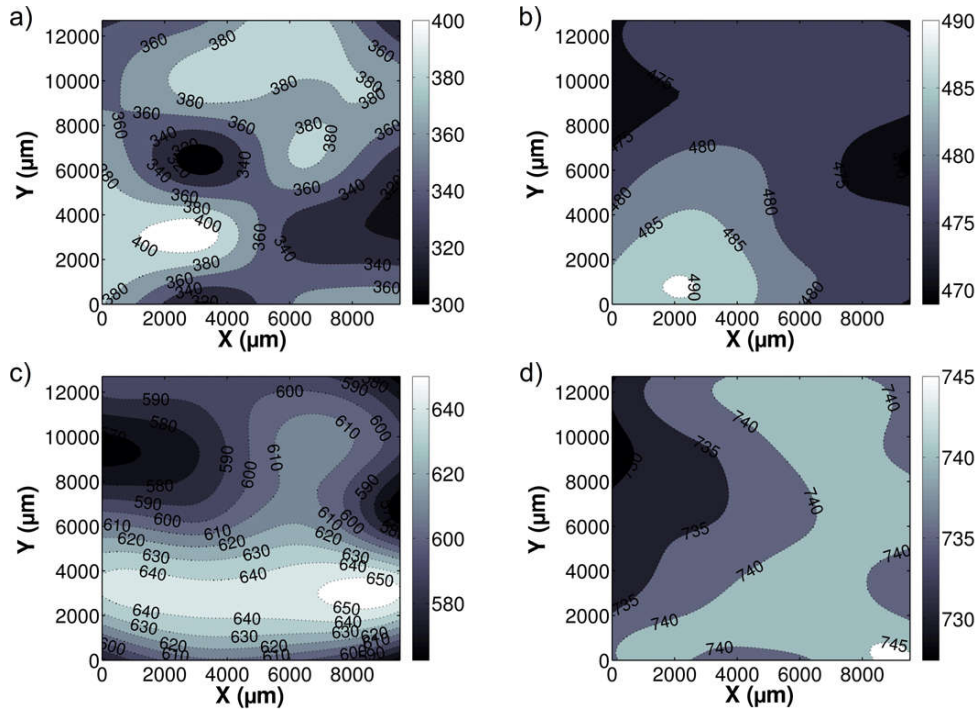


Figure 5.20 Contour plots of film thickness in Al-4B over glass slide deposited at: a) 100, b) 130, c) 160 and, d) 200 watts of sputtering power.

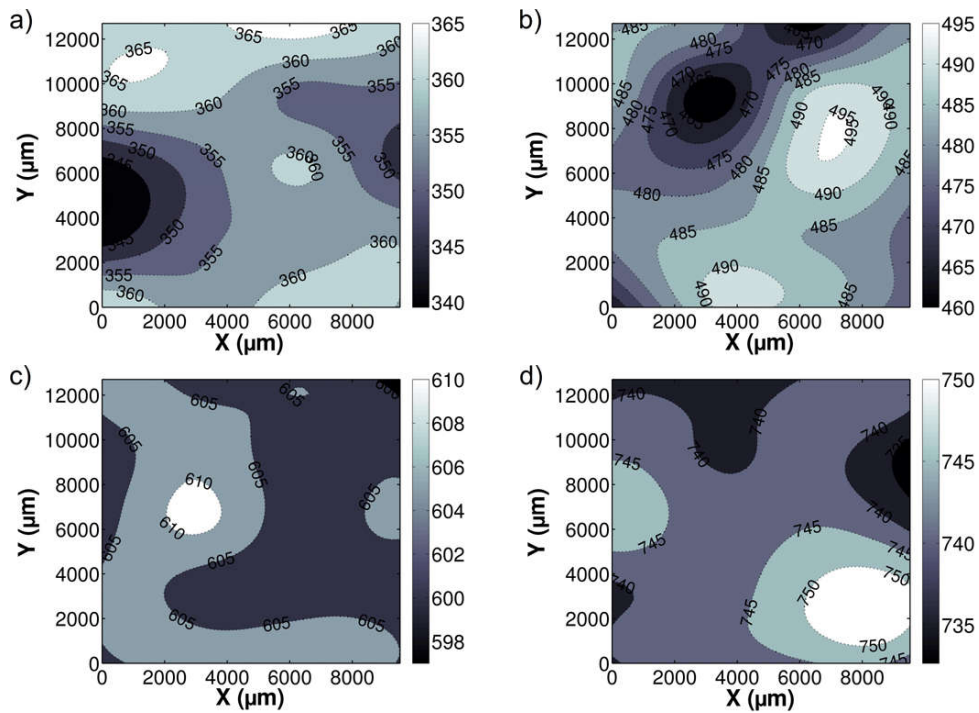


Figure 5.21 Contour plots of film thickness in Al-4B over silicon wafer deposited at: a) 100, b) 130, c) 160 and, d) 200 watts of sputtering power.

5.2.2 Mechanical Characterization: nanoindentation

The elastic modulus and hardness in the Al-4B and aluminum films were determined via nanoindentation by the continuous stiffness measurement method for thin films (CSM). As previously mentioned, the films samples were deposited on silicon wafer and glass slide. Figure 5.22 shows a graph of load versus normalized displacement from the surface in Al-4B and aluminum films. In this graph, the loading phase is the section that has smaller slope and the unloading phase is defined for line that has the steeper slope. The normalized displacement from the surface (%) is the indentation depth divided by the film thickness in each load increment.

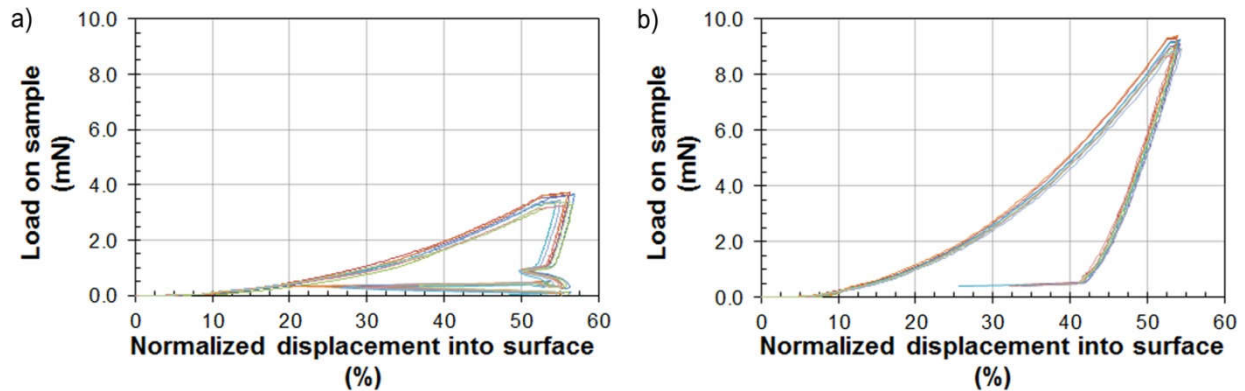


Figure 5.22 Characteristic nanoindentation curve: a) aluminum and, b) Al-4B film samples.

Figure 5.23 and 5.24 present the measured elastic modulus as a function of the normalized indentation depth in the aluminum and Al-4B samples, respectively. These specimens were deposited at a sputtering power of 200 watts on both substrates. The point results were determined by calculating the average in each range at 5% of the normalized displacement in the indentation depth. In these figures, the apparent

modulus (E_a) and film modulus (E_f) raise quickly until 10% of the normalized displacement and then increases moderately. The measurements acquired in this range are unreliable due to artifacts generated by the machinery control system, material surface or the high strain rate on contact [21], [63], [113], [114]. In addition, the error bars are an indicator of data dispersion in this first interval. The apparent modulus (E_a) was determined based on the Oliver and Pharr criteria or standard method, which considers the combined action of film/substrate system [57], [59]. The film modulus (E_f), which is independent of the substrate effects, was calculated using the Hay-Crawford methodology [63].

In Figures 5.23 and 5.24 the moduli vary as a function of the indentation depth caused by the substrate stiffness and the nature of the film material. Phenomena as sink-in or pile-up produce errant values of real contact area in the indentation with increasing depth and, thus, the proximity to the substrate. Sink-in occurs when the film is stiffer than the substrate and it leads to a lower contact area as the pile-up is presented by the crowding of material around the tip which generates a larger area as the film material, which is more compliant than the substrate [23], [60], [115], [116]. With this in mind, Hay and Crawford found lower dispersion in the results between 10 to 20 percent in the indenter penetration/films thickness [63].

Therefore, in the present dissertation and considering the tendency of curves in Figures 5.23 and 5.24, we have defined the 15% - 20% interval of the normalized displacement to show the results.

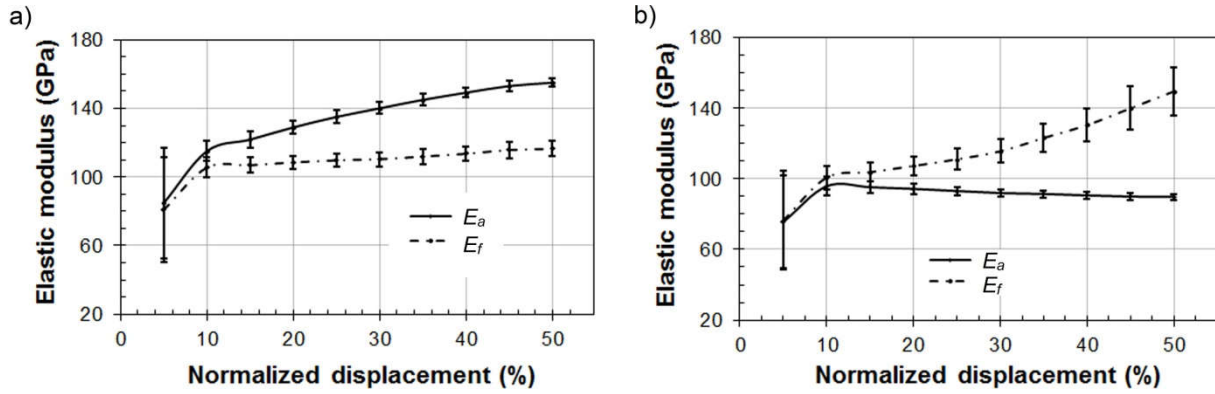


Figure 5.23 Elastic moduli in Al-4B films sputtered at 200 watts on: a) silicon wafer and, b) glass slide.

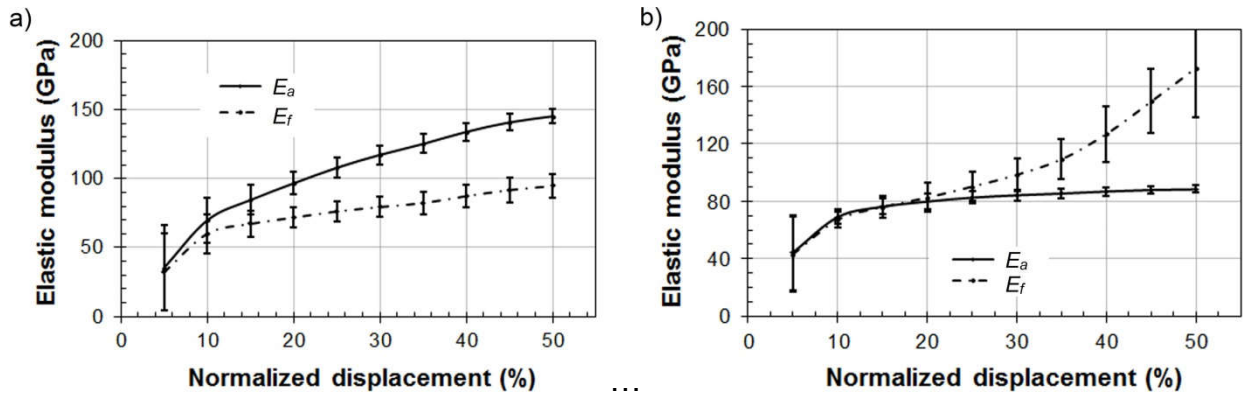


Figure 5.24 Elastic moduli in aluminum films sputtered at 200 watts on: a) silicon wafer and, b) glass slide.

Hardness results of the films are plotted in Figures 5.25 and 5.26 and present only a slight variation as a function of the normalized displacement. This helped us corroborate that the hardness is related with plastic deformation of material in each load step. Just as the elastic modulus, hardness is affected by the substrate effects due the actual contact area in the indentation even when it does not show a drastic change with depth [23], [60], [115], [116].

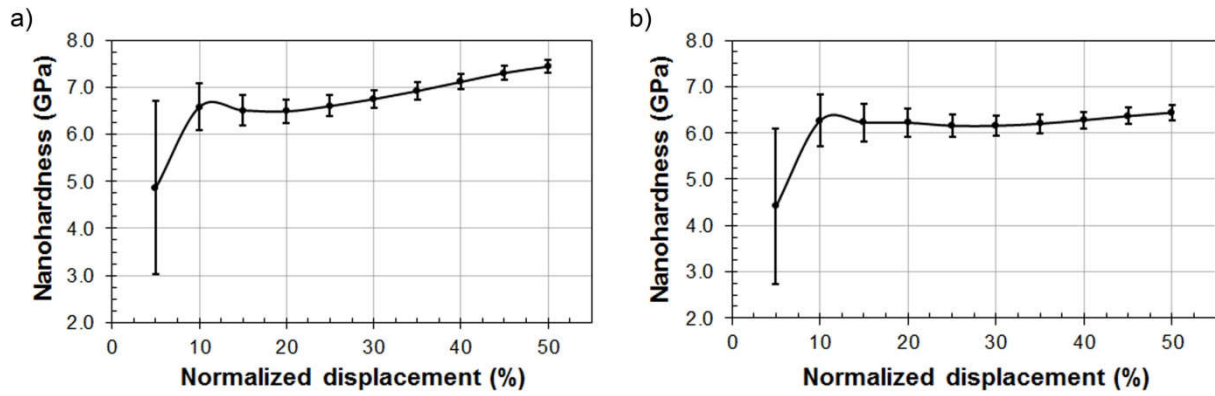


Figure 5.25 Hardness of Al-4B films sputtered at 200 watts on: a) silicon wafer and, b) glass slide.

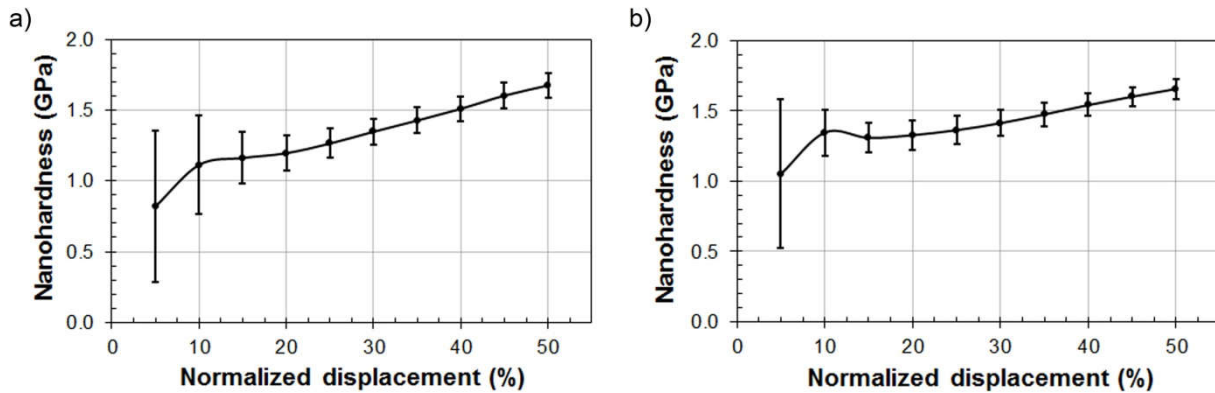


Figure 5.26 Hardness of aluminum films sputtered at 200 watts on: a) silicon wafer and, b) glass slide.

The average of the two mechanical properties measured on the films was evaluated for each level of the sputtering power on both substrate types, i.e. glass and silicon. Figure 5.27 and 5.28 present the elastic modulus and hardness obtained on the aluminum and Al-4B films, respectively. Results reveal that the films fabricated with the composite (Al-4B) target possess more rigidity and hardness than pure aluminum films under the same sputtering conditions. In the Al-4B thin films the elastic modulus and hardness increased slightly with sputtering power on both substrates. The maximum values on

the composite were 107 GPa of elastic modulus and 6.50 GPa of hardness at 200 watts. The aluminum film reached 84 GPa and 1.90 GPa, in modules and hardness, respectively. In section 5.1.2 we have demonstrated that the target made of Al-4B was harder than aluminum due to the reinforcing particles. Similarly, the properties of the target influenced the mechanical properties of the thin films at the nano-scale. When Ramos and Suárez fabricated films with Al-Si-B composite target via magnetron sputtering; they found this same tendency using nanoindentation [18]. Likewise, other researcher showed that the elastic modulus and hardness in films deposited with Al-Cu, Al-Cr-Cu and Al-Ti-Cu alloys were higher due to the presence of inclusions [38].

It should also be noted that in these figures, i.e. Figures 5.27 and 5.28, the difference between the measurements of the elastic modulus and hardness on films deposited on both substrates is not significant. This demonstrates that the CSM method eliminated the substrate effects on these two properties. Therefore, the 15% - 20% range of normalized depth selected previously is evidently appropriate for accurate results.

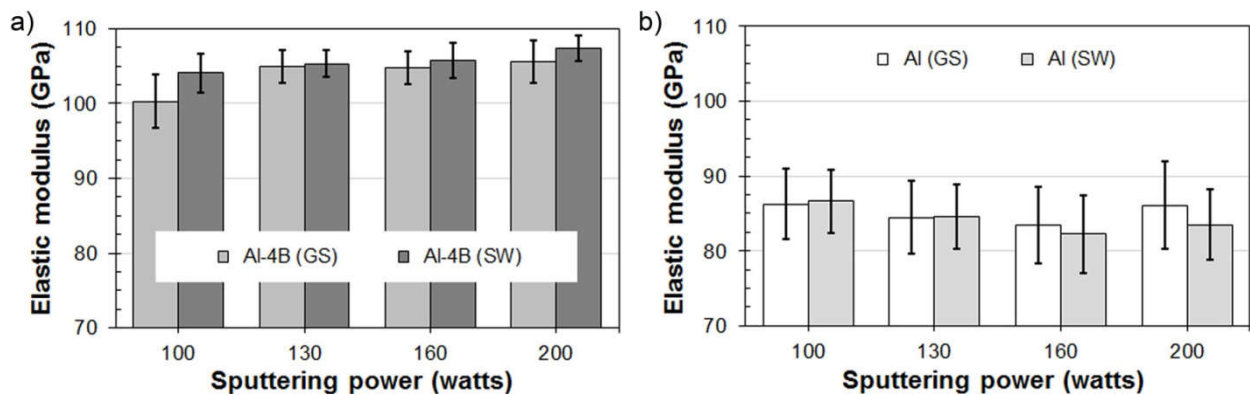


Figure 5.27 Average elastic modulus: a) Al-4B film and, b) aluminum film.

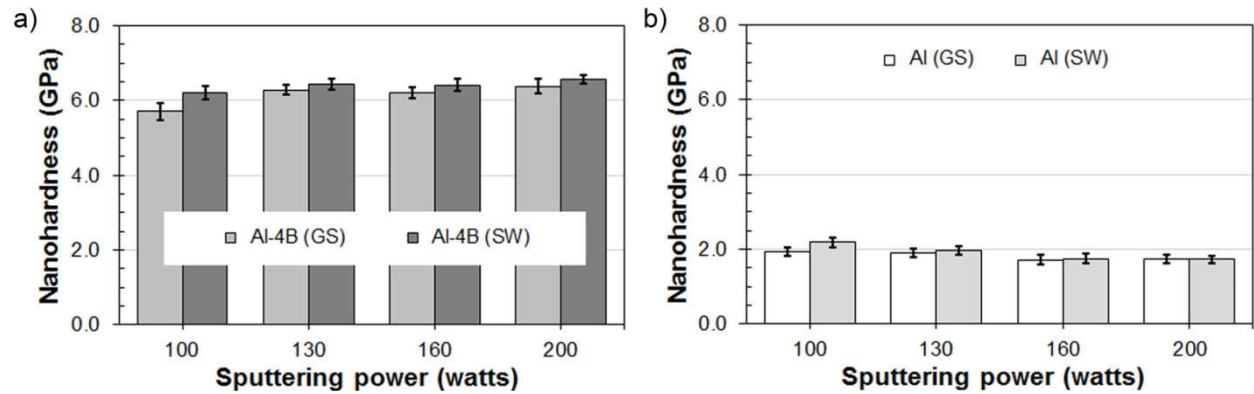


Figure 5.28 Average hardness at the nanoscale: a) Al-4B film and, b) aluminum film.

Another mechanical test available via nanoindentation helped determining the friction coefficient, the adhesion strength, and wear resistance: the ramp load scratch method described in section 3.3.1. Through this study we sought to evaluate the detachment resistance at the film/substrate interface.

Figures 5.29 and 5.30 present a typical scratch curve of displacement from the surface vs scratch distance in Al-4B samples for each sputtering power level; the films had been deposited on a silicon wafer and a glass slide, respectively. Similarly, the results for pure aluminum films are presented in Figures 5.31 and 5.32, which show the surface topography, the scratch curve, and the residual deformation recorded upon the test. Also, in each figure the critical load, i.e. the data point associated with film and substrate interface, was defined (film thickness).

The figures also show two particular features of the film material behavior during the scratch. First, the surface topography (dashed line) of the aluminum films was uneven with respect to the horizontal line for zero displacement from the nominal surface.

Conversely, in the Al-4B films the surface topography (dashed line) was smooth and overlapped with the zero line (baseline). These observations indicated that the films surface can have a high or low roughness, respectively (Figure 5.31 and 5.32). These measurements on the scratch curves; motivated us to use scanning electron microscopy (SEM) to image the samples surface in the scratch area.

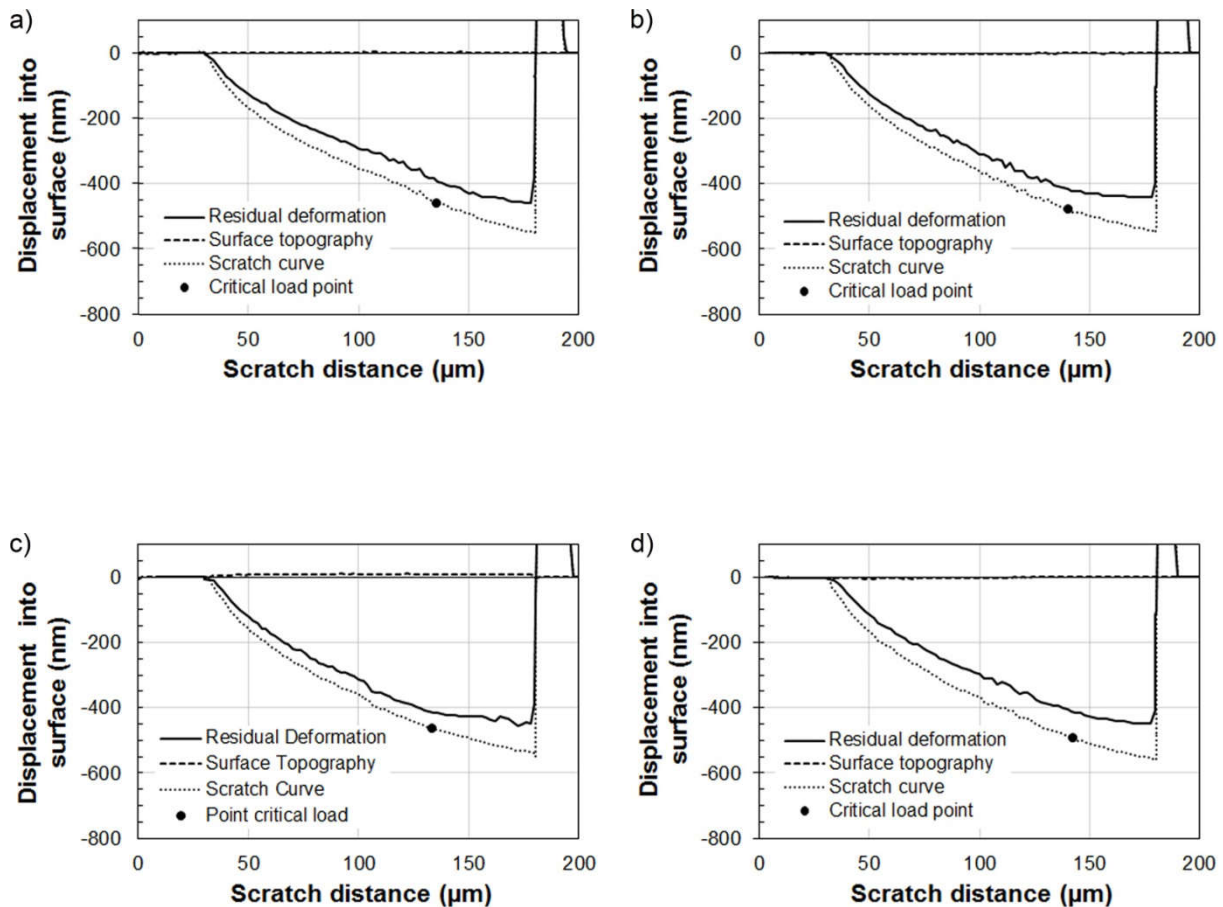


Figure 5.29 Scratch test results of Al-4B sputtered onto silicon wafer at: a) 100, b) 130, c) 160 and, d) 200 watts.

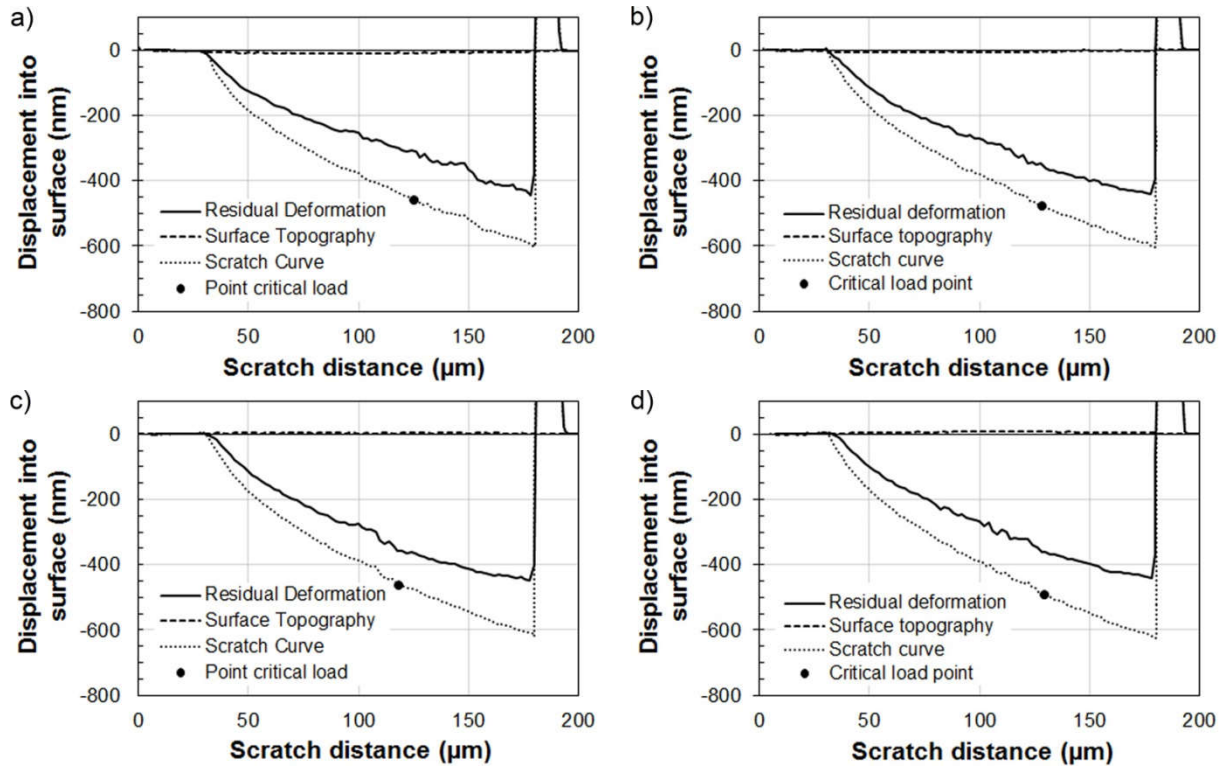


Figure 5.30 Scratch test results for Al-4B film sputtered onto glass slide at: a) 100, b) 130, c) 160 and d) 200 watts.

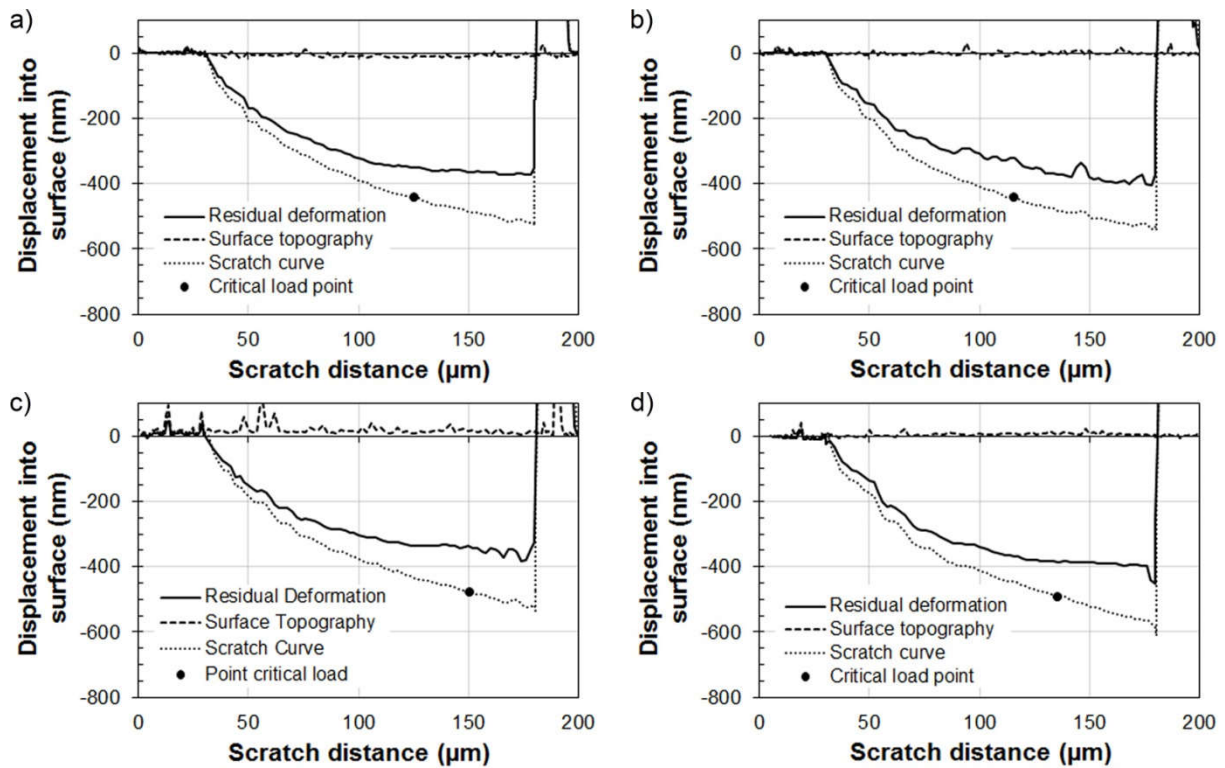


Figure 5.31 Scratch test results for aluminum film sputtered onto silicon wafer at: a) 100, b) 130, c) 160 and d) 200 watts.

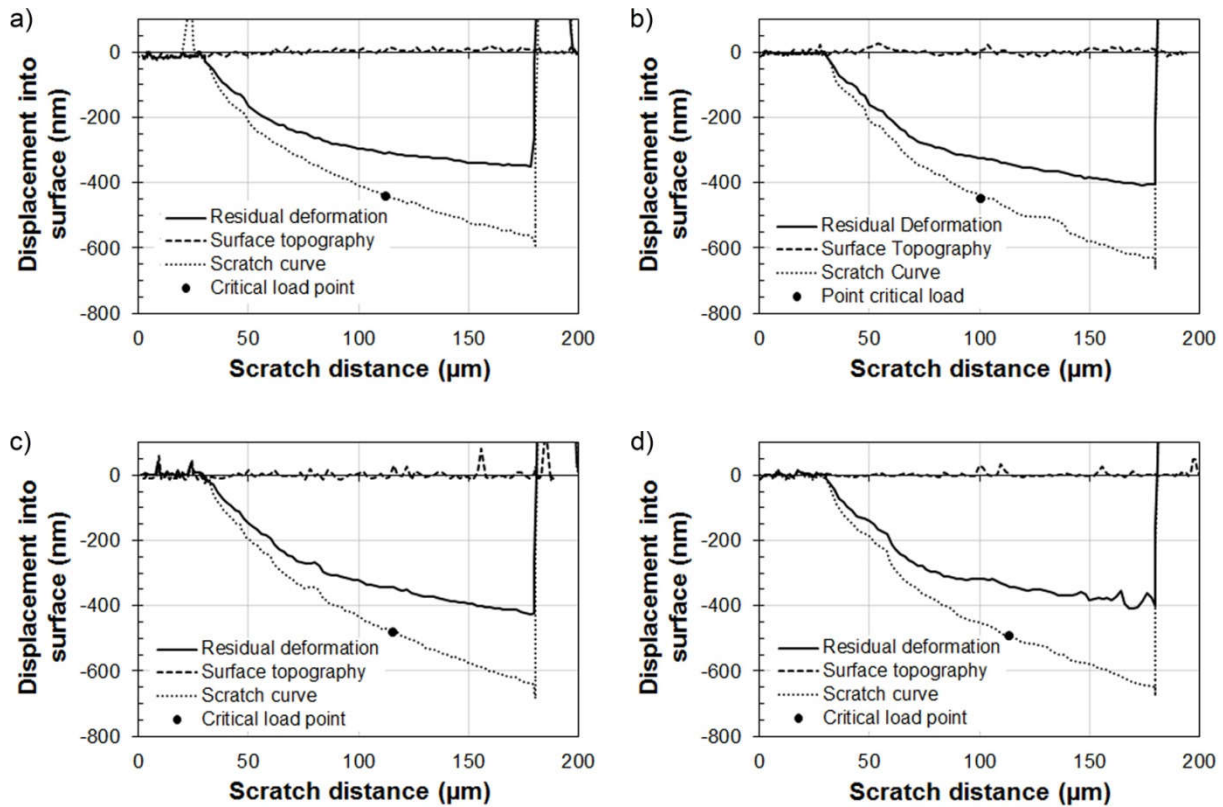


Figure 5.32 Scratch results for aluminum film sputtered onto glass slide at: a) 100, b) 130, c) 160 and d) 200 watts.

Figures 5.33 and 5.34 show the scratch tracks made with the Berkovich diamond tip on the Al-4B and aluminum films, respectively. At first sight, the SEM images did not exhibit significant differences in the material surface for each sample, although in the aluminum specimens small white dots can be recognized (Figure 5.34). To further look at this, another image was taken at higher magnification of the track adjacent zone in both materials (Figure 5.35). The pure aluminum track image clearly shows the surface texture with some bright spots and shapes (Figure 5.35b), while the film of the Al-4B surface is much smoother (Figure 5.35a). This observed feature of the aluminum film surface is associated to grain texture, where the bright dots correspond to the hillock type formation, as previously reported in aluminum films studies [33], [36], [38], [117]–

[120]. Therefore, the unevenness (roughness) recorded in the first track of the scratch tests (surface topography) on the aluminum films is an evidence of these grains and the hillocks of the surface (Figure 5.35b).

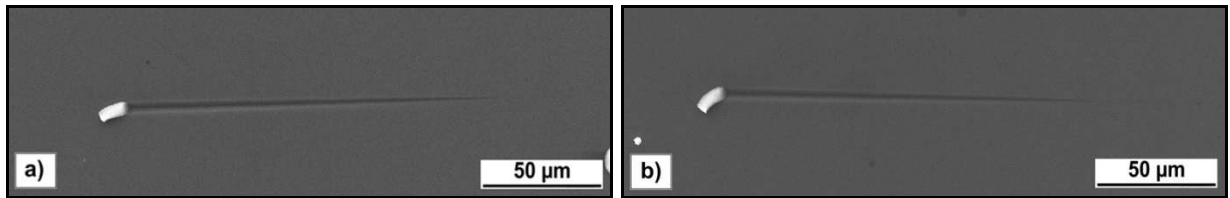


Figure 5.33 Al-4B film surface scratched over: a) silicon wafer and, b) glass slide.

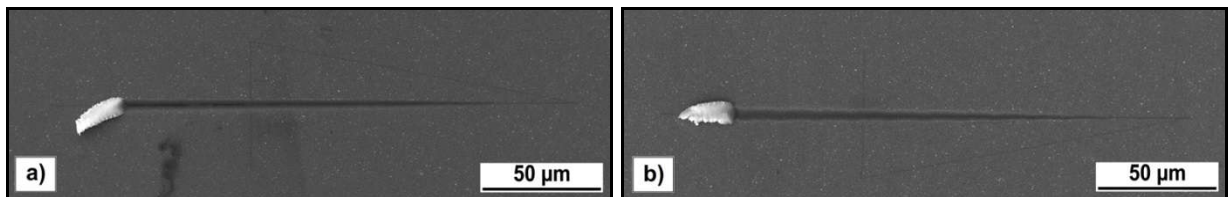


Figure 5.34 Aluminum film surface scratched over: a) silicon wafer and, b) glass slide.

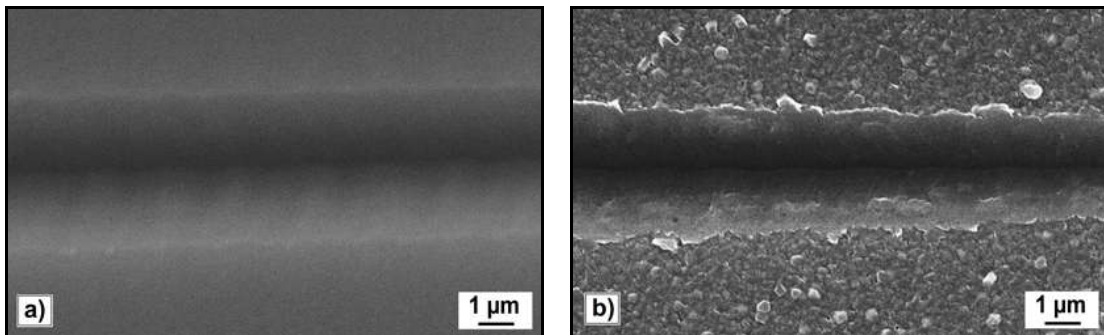


Figure 5.35 Detail at the section intermediate of scratched track for: a) Al-4B film and, b) aluminum film.

Secondly, there is a difference between the corresponding scratch curves and the residual deformations relative to the substrate, as seen in Figures 5.29 to 5.32. This difference was analyzed with the percentage of elastic deformation parameter used in the literature in a scratch testing of low dielectric constant films [121]. With the elastic

deformation parameter the authors measured the plastic deformation resistance of these materials as a result of manufacturing processes, such as polishing.

In our test, the parameter was determined from the difference between the areas on the lines of the scratch curve and the residual deformation calculated until a distance of 75 μm on the horizontal axis (Figures 5.36). This distance was considered in order to remove any elastic recovery effect to the substrate during test post loading [122], [123].

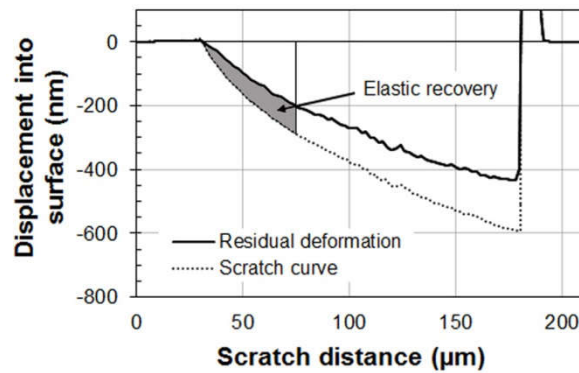


Figure 5.36 Elastic recovery area in scratch test.

Figure 5.37 presents this elastic recovery as a percent of the residual deformation for each substrate. The results reveal that the Al-4B films have larger elastic recovery compared to aluminum films. This observed behavior during the scratch test could be linked to the films' hardness (H) and elastic modulus (as function of effective elastic modulus E_{eff}) [124]. Bao et al. related these properties in a parameter of recovery resistance (R_s) applied to a study of nanoindentation in bulk materials of aluminum, silicon, copper, magnesium and Ti_2SnC [124]. They defined R_s as the ratio between E_{eff}^2 and H , which were determined via load control method in a triboindenter. Their findings showed that materials with a high E_{eff} generate a higher value R_s , which indicates a high plastic deformation, given that E_{eff} is inversely proportional to h_s , i.e. the

elastic displacement at the contact point during indentation [57], [59]. In other words, the recovery resistance (R_s) is a measure of the energy dissipation capacity of the material [124].

Later, this concept (R_s) was introduced in a study of reinforced aluminum films with carbon nanotubes (CNT) using a nano-scratch test [125]. Chen et al. concluded that the coating with a higher amount of CNT presented a higher elastic recovery compared to the reference material, i.e. aluminum. Furthermore, these coatings consistently presented higher elastic modulus and hardness.

Therefore, the above evidence confirms that the resistance to plastic deformation (elastic recovery) found in the Al-4B films is a consequence of hardness and elastic modulus. In summary, these films demonstrated better mechanical performance than the aluminum films upon the CSM tests (Figures 5.27 and 5.28).

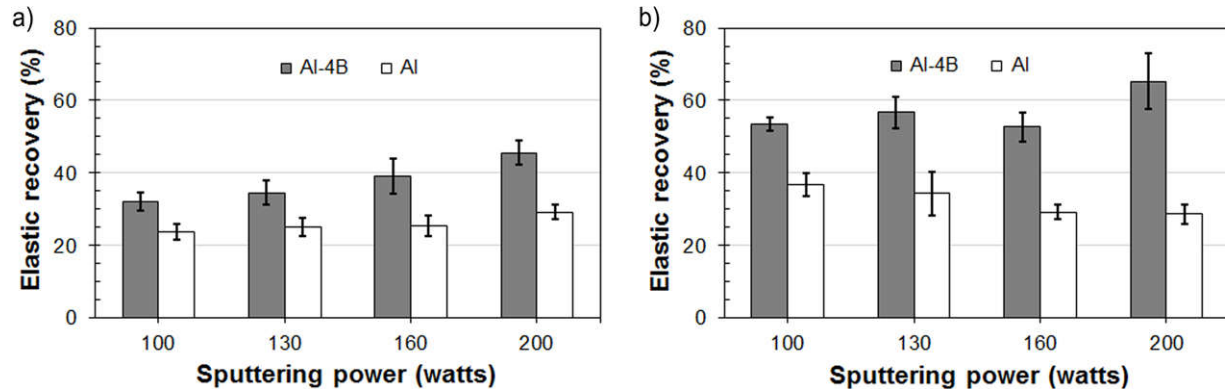


Figure 5.37 Elastic recovery results in Al-4B and aluminum films sputtered in: a) silicon wafer and, b) glass slide substrates.

Following the above analysis, the friction coefficient μ (equation 3-16) and adhesion strength τ (equation 3-18) were calculated in the film/substrate interface, using the film thickness as reference. Figure 5.38 presents the results as a function of the sputtering

power. The friction coefficient μ of each material sputtered onto silicon wafer and glass slide remains approximately equal for each power level (left curve in Figure 5.38). Therefore, we deem sensible to conclude that the friction coefficient is not being affected by the nature of the amorphous glass slide or the crystalline structure of silicon wafer (100) plane. In contrast, the adhesion strength results presented in Figure 5.38 (right) show a difference with respect to the substrate. The difference between both properties can be explained considering that the adhesion strength (τ) uses the magnitude of the resultant force and the β angle obtained from force diagram for the development of equation 3-17 (Appendix C). Furthermore, it should be noted that the substrate stiffness influences the mechanical properties and behavior of the film material at the interface due to composite action [122], [123], [126]–[128]. In our case, the elastic modulus of the glass slide and the silicon wafer measured via nanoindentation were 84 GPa and 170.52 GPa, respectively.

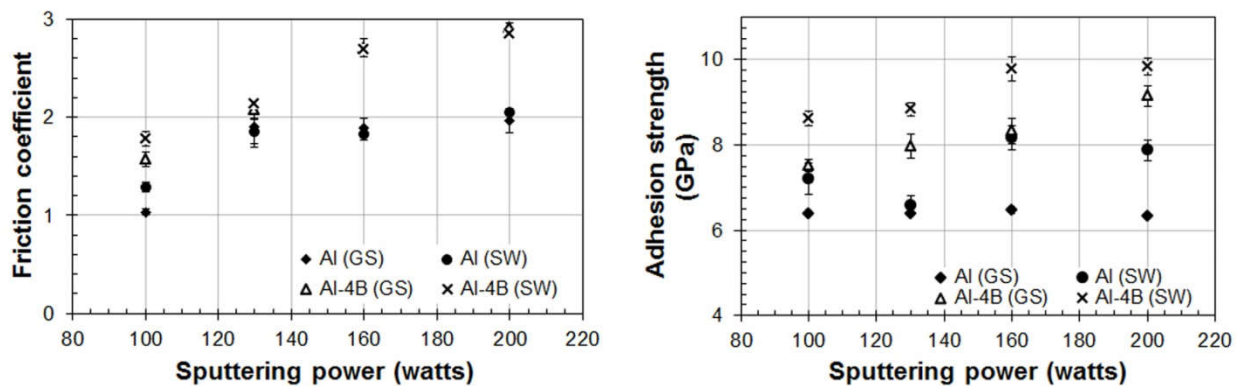


Figure 5.38 Friction coefficient (left) and adhesion strength (right) in film samples sputtered for both substrate.

As mentioned previously, some authors suggested that the friction coefficient and the adhesion strength determined by the wear test would measure the adhesion degree between the substrate and the film [73]–[77], [127]. However, it must be noted that this

result, which depends on the material removal mechanism, can be affected by the nanoindenter's tip geometry, the material, and the tip/material/substrate interaction [90], [91]. In our case, the adhesion analysis, defined in the section 3.44, assumes that there is a shear stress occurring between the attack face of indenter tip and the removed material (Figure 3.20). Considering of this, Figure 5.39 shows two micrographs that were taken of the scratched end upon the scratch test ramp load on the films made of Al-4B and aluminum using SEM. It can be seen that the material is separated in the form of a chip. In abrasive wear, this mechanism is called cutting, which is characteristic of the scratch test of a single cycle conducted on ductile materials [72], [90], [129], [130]. This led us to conclude that our methodology could be considered suitable alternative for determining the adhesion strength (τ) at the nano-scale using the ramp load scratch test in a single cycle via nanoindentation in ductile materials.

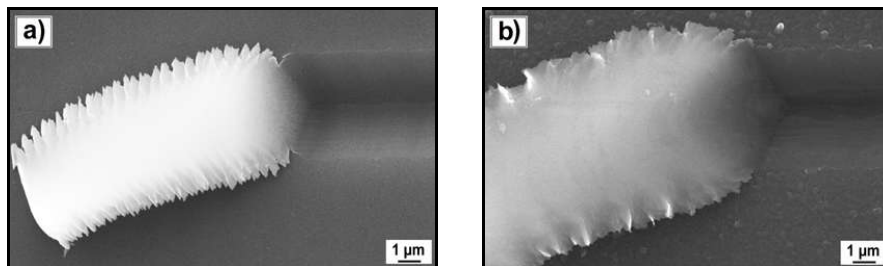


Figure 5.39 SEM micrographs in scratched end for: a) Al-4B film and, b) aluminum film.

Using our nanoindenter we developed another tribological experiment with the ramp load scratch test. In this experiment the material wear was defined similarly to the wear test of bulk materials using pin-on-disk apparatus; in this case the wear is the removed material volume in mm^3 on the sample surface by means of a hard pin according to ASTM G99-17. In this test, the maximum applied force and the scratched distance

remained constant. For the films, we calculated the material volume of the track that produces the scratch curve (Figure 3.9) applying equation 3.20 (Section 3.3.1). The wear results in the samples are presented in Figure 5.40, which reveals that the aluminum film underwent more material removal than the Al-4B film samples. This means that the Al-4B composite films had larger resistance to material loss (wear) upon the test due to its higher elastic modulus and hardness compared to the pure aluminum films. This same behavior was observed in wear studies on aluminum composite coatings reinforced with carbon nano-tubes (CNTs), where the samples that had more CNT amount presented a smaller wear volume removal [125], [131], [132]. Hence, the CNT reinforcement of the aluminum matrix improved wear performance of these coatings at the nanoscale. One can therefore infer that the strengthening of the nanoscaled coatings resembles the strengthening of metallic matrices by means of reinforcing particles. Wear literature concerning aluminum matrices reinforced with particles, e.g. Al_3Ti , AlB_2 , Al_3Ni and SiC , found that the volume of removed material in the wear test was smaller than in the pure material, i.e. without reinforcement. These composites were harder indicating that the particles in the matrix material affected the wear results [6], [9], [10], [133], [134]

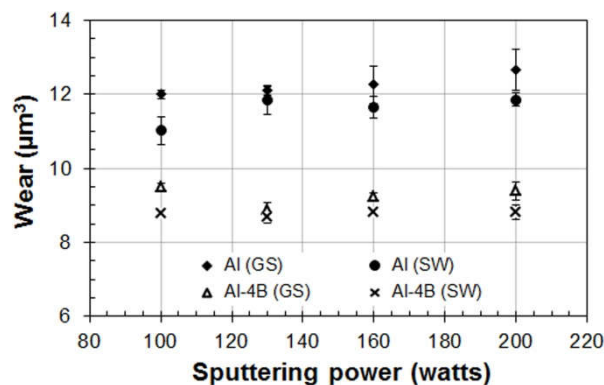


Figure 5.40 Wear volume in film samples.

In closing this segment on the films mechanical characterization, the continuous stiffness measurement (CSM) and ramp load scratch test via nanoindentation demonstrated how the properties of the Al-4B composite deposition target were effectively transferred to the sputtered material that formed the films.

Also, one should note that at all studied sputtering powers the Al-4B films displayed higher coefficients of friction and adhesion strength than the aluminum film (Figure 5.38). The highest values were reached in the sputtering power levels of 160 and 200 watts. The modulus of elasticity and hardness showed a slight increase as sputtering power increased (Figure 5.27 and 5.28). Therefore, these findings suggest that the sputtering power and the target material may be having an effect in the film material film leading to changes in its mechanical properties. In order to understand this behavior in the film materials we analyzed the microstructure morphology and the crystal structure of the films using atomic force microscope (AFM) and x-ray diffraction, respectively.

5.2.3 Surface Morphology

Microstructure morphology of the films surface was studied using AFM and the SPIP™ software from Image Metrology [Ref]. This technique allowed us to evaluate the root mean square (RMS) roughness and grain size in the samples manufactured by sputtering.

5.2.3.1 Roughness Study

The measurement of surface roughness in the metallic films allows determining the degree of smoothness, as a result of the manufacturing process. The importance of this

measure is that the roughness of film can affect the film conductivity; it reduces the film reflectivity and induces the electromigration phenomenon reducing the operation effectiveness and the useful lifetime of MEMs [19], [31], [38], [135], [136].

The RMS roughness is a measurement that is normally used to characterize the surface smoothness in thin films research. The roughness is calculated with the 5-3 equation where M and N are the points of the scan area and $z(x_k, y_l)$ is the height of the peaks or valleys for each point k and l .

$$RMS\ roughness = \sqrt{\frac{1}{MN} \sum_{k=0}^{M-1} \sum_{l=0}^{N-1} (z(x_k, y_l))^2} \quad (5-3)$$

The AFM images were captured in the films with 500 nm thickness and processed with the SPIP™ software that uses equation 5-1. The samples were scanned using 2.25, 9, 25, 100 and 625 μm^2 ranges. These results are summarized in Table 5.3 and 5.4, and the average values, graphed as a function to the film material in Figure 5.41. The average RMS results on both substrates reveals that the roughness in Al-4B films was lower compared to the aluminum film. The values were 3.05 nm on the silicon wafer and 3.41 nm on the glass slide (Table 5.3). Aluminum produced RMS' of 25.23 and 23.43 nm, respectively (Table 5.4).

Table 5.3 RMS roughness summary of Al-4B films.

| Substrate | Silicon wafer (SW) | | | | | Glass slide (GS) | | | | |
|--------------------------|-------------------------------|------|------|------|------|-------------------------------|------|------|------|------|
| | Scan area (μm^2) | | | | | Scan area (μm^2) | | | | |
| Sputtering power (watts) | 2.25 | 9 | 25 | 100 | 625 | 2.25 | 9 | 25 | 100 | 625 |
| 100 | 3.11 | 3.21 | 3.63 | 3.48 | 4.31 | 3.11 | 2.63 | 2.57 | 2.75 | 4.45 |
| 130 | 2.14 | 2.17 | 2.51 | 2.48 | 4.12 | 1.75 | 2.11 | 2.26 | 2.74 | 5.03 |
| 160 | 2.82 | 2.96 | 3.16 | 3.09 | 3.36 | 2.92 | 3.09 | 3.29 | 3.51 | 6.01 |
| 200 | 2.91 | 2.74 | 2.66 | 2.93 | 3.14 | 3.20 | 3.62 | 3.95 | 3.96 | 5.28 |
| Average | 3.05 | | | | | 3.41 | | | | |

Table 5.4 RMS roughness summary of Al films.

| Substrate | Silicon wafer (SW) | | | | | Glass slide (GS) | | | | | |
|--------------------------|-------------------------------|-------|-------|-------|-------|-------------------------------|-------|-------|-------|-------|--|
| Sputtering power (watts) | Scan area (μm^2) | | | | | Scan area (μm^2) | | | | | |
| | 2.25 | 9 | 25 | 100 | 625 | 2.25 | 9 | 25 | 100 | 625 | |
| 100 | 20.35 | 21.20 | 46.13 | 19.27 | 27.86 | 14.52 | 17.34 | 23.12 | 33.53 | 29.36 | |
| 130 | 15.94 | 14.75 | 25.66 | 33.71 | 33.39 | 17.43 | 15.94 | 17.99 | 31.90 | 35.91 | |
| 160 | 9.39 | 13.93 | 32.35 | 29.60 | 28.48 | 11.90 | 12.85 | 16.24 | 26.32 | 31.99 | |
| 200 | 17.68 | 27.29 | 31.57 | 30.47 | 25.49 | 18.50 | 23.93 | 29.09 | 31.45 | 29.93 | |
| Average | | | | | | 25.23 | | | | | |

In Figure 5.41, the error bars evince the dispersion of the roughness. This dispersion is best visualized in the three-dimensional bar chart in Figures 5.42 and 5.43 where the roughness was plotted as a function of the scan area and the deposition power. As one can see in the aluminum films, the dispersion was remarkable for each analysis point (Figure 5.42b and 5.43b), unlike in the Al-4B films (Figure 5.42a and 5.43a). Consequently, we decided to analyze the films surface from the AFM captured images across the scan areas of 625, 100 and 25 μm^2 , in order to find a possible cause of such dispersion (Figure 5.44 and 5.45).

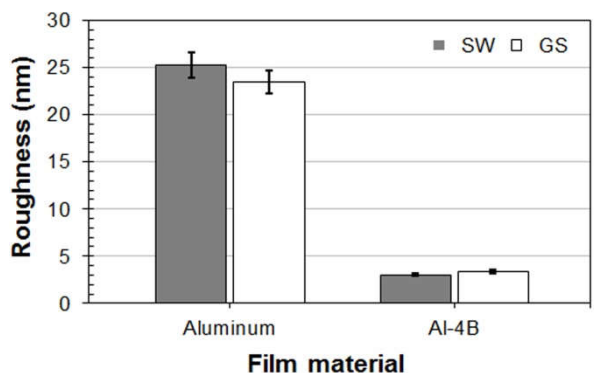


Figure 5.41 Average RMS roughness in the film material.

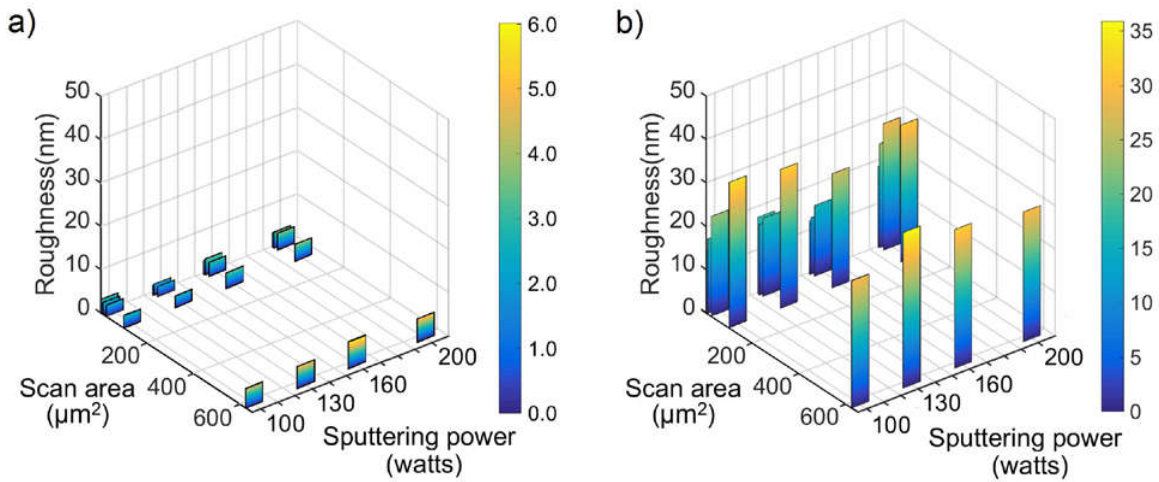


Figure 5.42 RMS roughness: a) Al-4B films and, b) aluminum films deposited on glass slide.

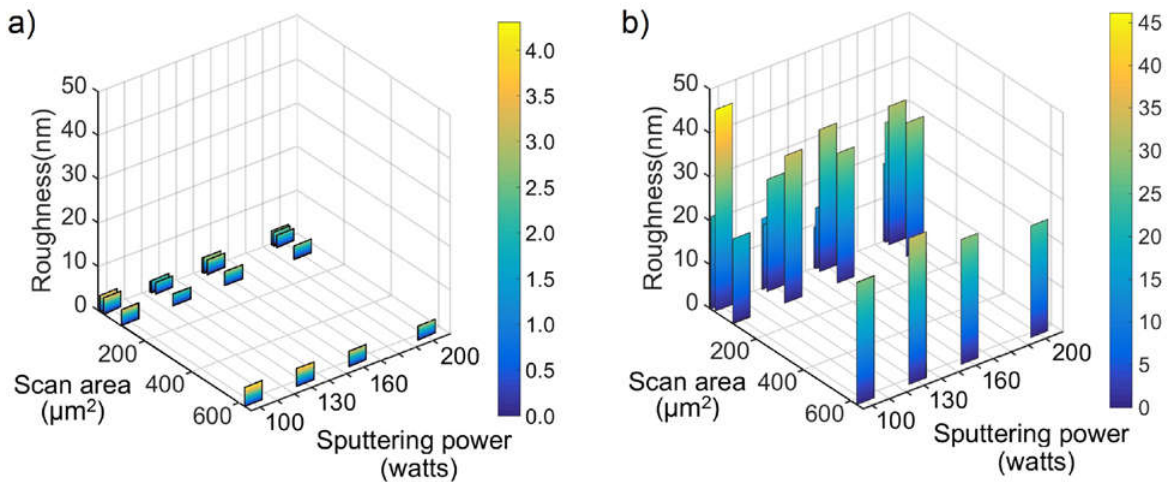


Figure 5.43 RMS roughness: a) Al-4B films and, b) aluminum films deposited on silicon wafer.

The aluminum images in Figure 5.44 revealed bright spots of different sizes in the material matrix. Previously, these bright spots were also observed in the micrographs of Figure 5.35b in section 5.2.2 of this thesis. In that section, we attributed to the hillock formation the bigger roughness of the films surface [33], [36], [38], [117]–[120]. Taking this into consideration, it is worth it to assert that the roughness in the aluminum films,

as measured on the AFM images, depends on the scan area, as well as the density and size of the hillocks.

This analysis was carried out in the Al-4B films produced under similar conditions. In the AFM image at $625 \mu\text{m}^2$, we can see two small bright spots on the Al-4B film surface (Figure 5.45a), whereas in other smaller scan areas (100 and $25 \mu\text{m}^2$) the surface is smooth and uniform, without significant bright spots (Figures 5.45b, c). Therefore, the low roughness of these films differs from aluminum films due to the reduction of hillocks during sputtering.

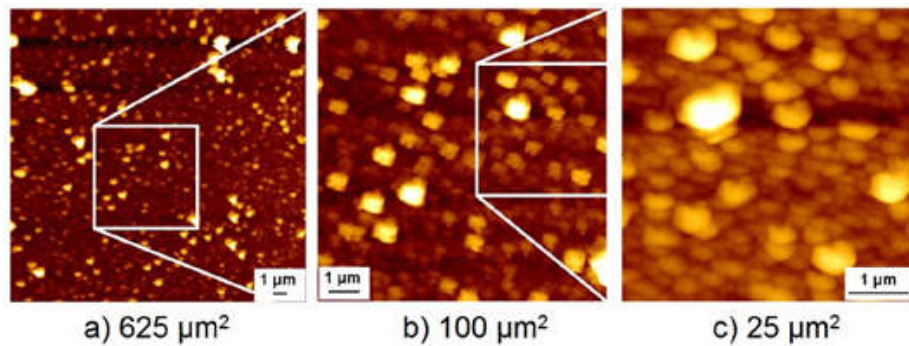


Figure 5.44 AFM images of aluminum film fabricated to 130 watts.

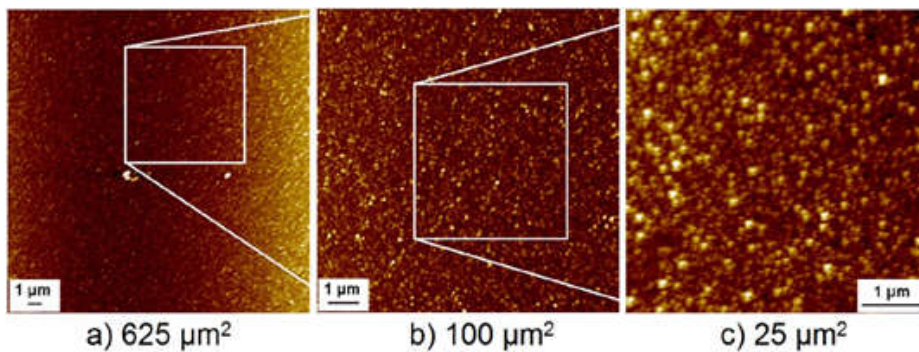


Figure 5.45 AFM images of Al-4B film fabricated to 130 watts.

5.2.3.1.1 Roughness - Substrate Effects

The overall roughness results found in Al-4B films and aluminum films do not show a substrate-related effect. Both materials tend to have the same behavior in the glass slide and the silicon wafer (Figure 5.41). Apparently, the thick 500nm film masked any effect of the substrate on the surface roughness of the material. Therefore, we decided to measure the roughness on films deposited at 200 watts with thicknesses of 500 and 100 nm in order to observe any substrate effect. The films were analyzed with scan AFM areas of 0.25, 1.0, 2.25, 9.0 and 25 μm^2 .

The results found were recorded in Table 5.5 and graphed in Figure 5.46. As one can see, the roughness values of Al-4B films measured on silicon wafer and glass slide tend to overlap for each scanning area for the 500 and 100 nm thicknesses (Figure 5.46a). The average RMS ranged from 2.05 to 3.02 nm (Table 5.5). Therefore, we believe that this material roughness was not considerably affected by the two parameters, i.e. thickness and substrate nature.

In contrast, the roughness in the aluminum films displayed variation, especially in the 500 nm sample. Therefore, the thickness of the films is playing an important role in this surface property, because the roughness increased with the thickness of the film (Figure 5.46b). The average roughness changed from 8.65 nm and 9.02 nm in films of 100 nm thick at 19.56 nm and 15.81 nm for the thickness of 500 nm over the two substrates (Table 5.5). Some aluminum films studies have reported via AFM technique a particular increase in the roughness as the thickness increases, due to grain size growth by coalescence among grains and the hillock phenomenon [20], [137]–[140].

In the Figures 5.47 and 5.48, the AFM images show the surface of deposited samples to 100 and 500 nanometers for the aluminum and Al-4B films, respectively. The aluminum samples exhibit a grain size difference in relation to the film thickness, where some grains are more prominent than others (Figure 5.47b). In Al-4B samples the surface displays small grains, in overall (Figure 5.47a). Therefore, these images allowed us to observe the changes in the surface of the films material with the thickness that affects to roughness.

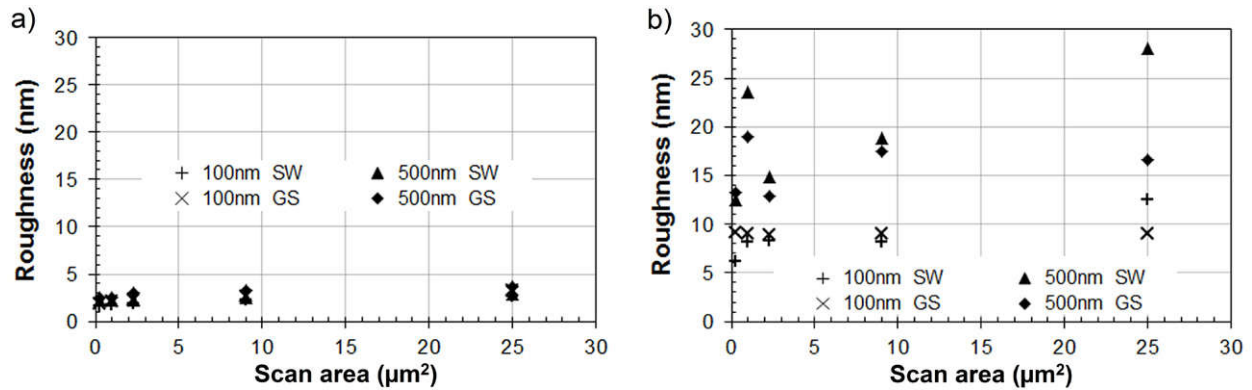


Figure 5.46 RMS roughness results in a) Al-4B and, b) aluminum film as function scan area.

Table 5.5 RMS roughness summary

| Film | Al-4B | | | | Aluminum | | | |
|-----------------|--------------------|------|------------------|------|--------------------|-------|------------------|-------|
| | Silicon wafer (SW) | | Glass slide (GS) | | Silicon wafer (SW) | | Glass slide (GS) | |
| Substrate | Thickness (nm) | | Thickness (nm) | | Thickness (nm) | | Thickness (nm) | |
| Scan area (µm²) | 100 | 500 | 100 | 500 | 100 | 500 | 100 | 500 |
| 0.25 | 1.67 | 2.27 | 1.89 | 2.47 | 6.13 | 12.51 | 9.20 | 13.26 |
| 1.00 | 1.80 | 2.19 | 2.15 | 2.53 | 8.12 | 23.60 | 8.98 | 18.94 |
| 2.25 | 1.92 | 2.27 | 2.31 | 3.07 | 8.33 | 14.85 | 8.96 | 12.83 |
| 9.00 | 2.21 | 2.48 | 2.67 | 3.34 | 8.13 | 18.81 | 8.98 | 17.47 |
| 25.00 | 2.64 | 2.93 | 3.30 | 3.68 | 12.55 | 28.02 | 9.00 | 16.56 |
| Average | 2.05 | 2.43 | 2.47 | 3.02 | 8.65 | 19.56 | 9.02 | 15.81 |

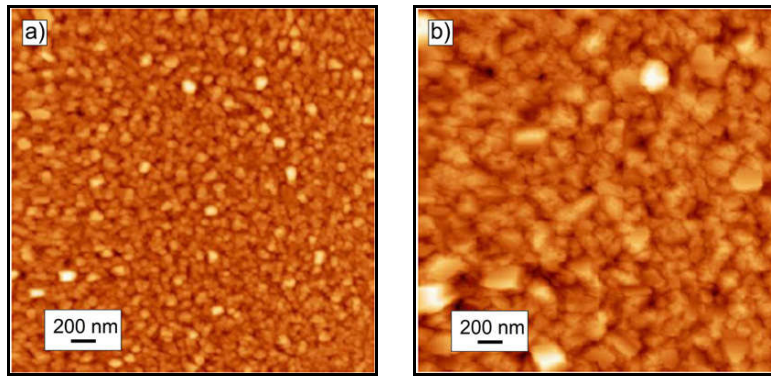


Figure 5.47 Aluminum film surface for a) 100 nm and, b) 500 nm of thickness

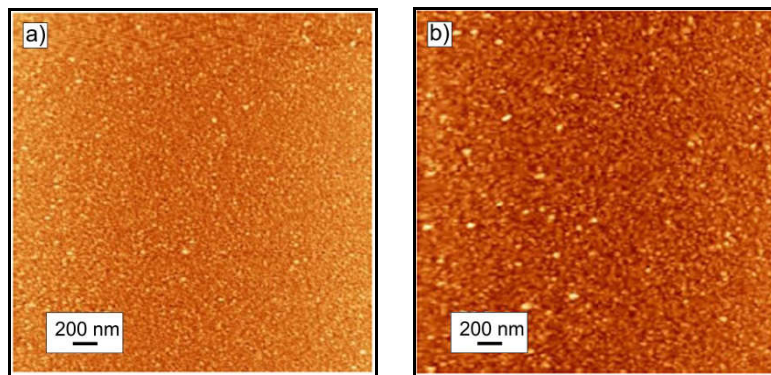


Figure 5.48 Al-4B film surface for a) 100 nm and, b) 500 nm of thickness

5.2.3.2 Hillock Formation

In SEM images (Figure 5.35) and via AFM (Figure 5.44 and 5.47) we detected bright spots in the aluminum films. In the AFM images of Figure 5.45 for the Al-4B films bright spots were also found. These points were identified in these two dimensional images as a hillock and it was compared with the reported by the metallic films researchers.

Hillocks on films are produced by compression stresses generated during the film fabrication particularly when metallic soft materials are used. Also, it is the mechanism of stress relaxation where the material moves by diffusion in the grain boundaries [32], [53]. As proven in this thesis, the phenomenon can be observed with greater clarity via three-dimensional AFM images on the films with 500 nm thickness for levels of sputtering power that were studied (Figure 5.49 and 5.50). The scanning area used for this analysis was $25 \mu\text{m}^2$.

The aluminum films images presented in Figure 5.49 reveal the presence of hillocks on the material surface. These protuberances (hillocks) stand out on the film matrix surface.

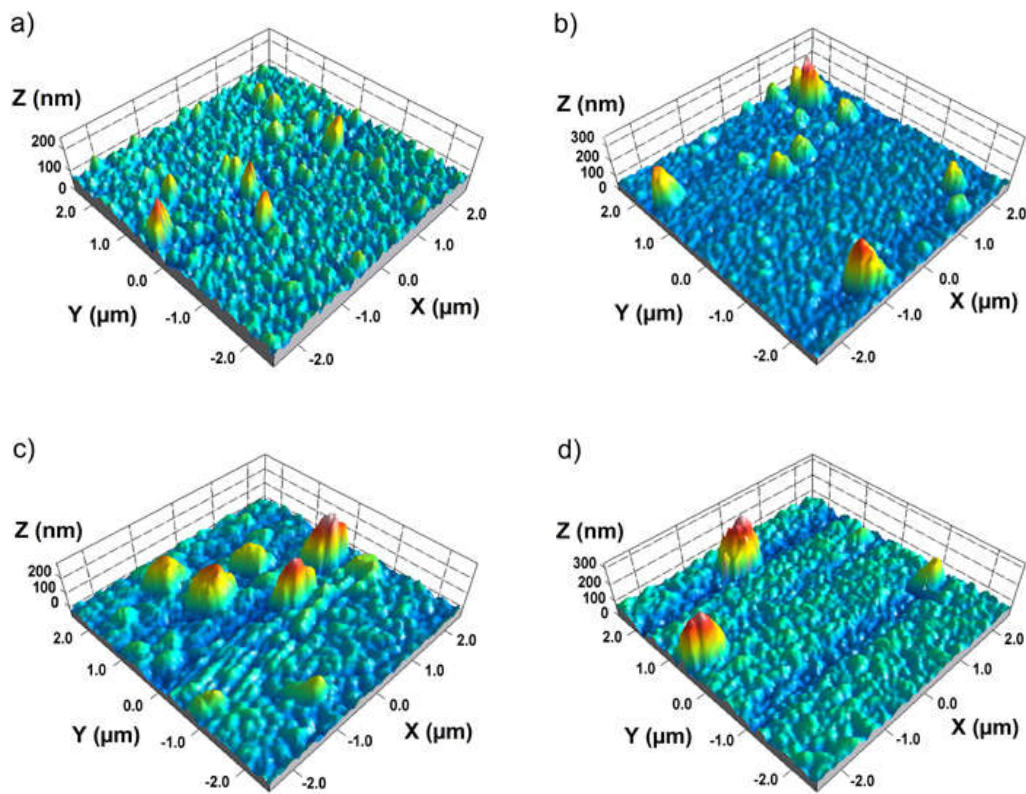


Figure 5.49 Hillock growth at the aluminum films for sputtering power of: a) 100, b) 130, c) 160 and, d) 200 watts.

Conversely, the Al-4B films images did not show these protrusions and the resulting surface was uniform without much difference, as one can see in Figure 5.50.

The hillocks height was measured using the z-range parameter of the metrology image software (SPIP™) and compared between both materials as a function of the sputtering power. In Figure 5.51 one can observe a significant difference between the hillocks height between both materials. In the Al-4B films a 90% decrease was achieved in this study (Table 5.6). The composite material (Al-4B) produced larger resistance to hillock formation, which is supported by the literature [34], [38], [134], [140].

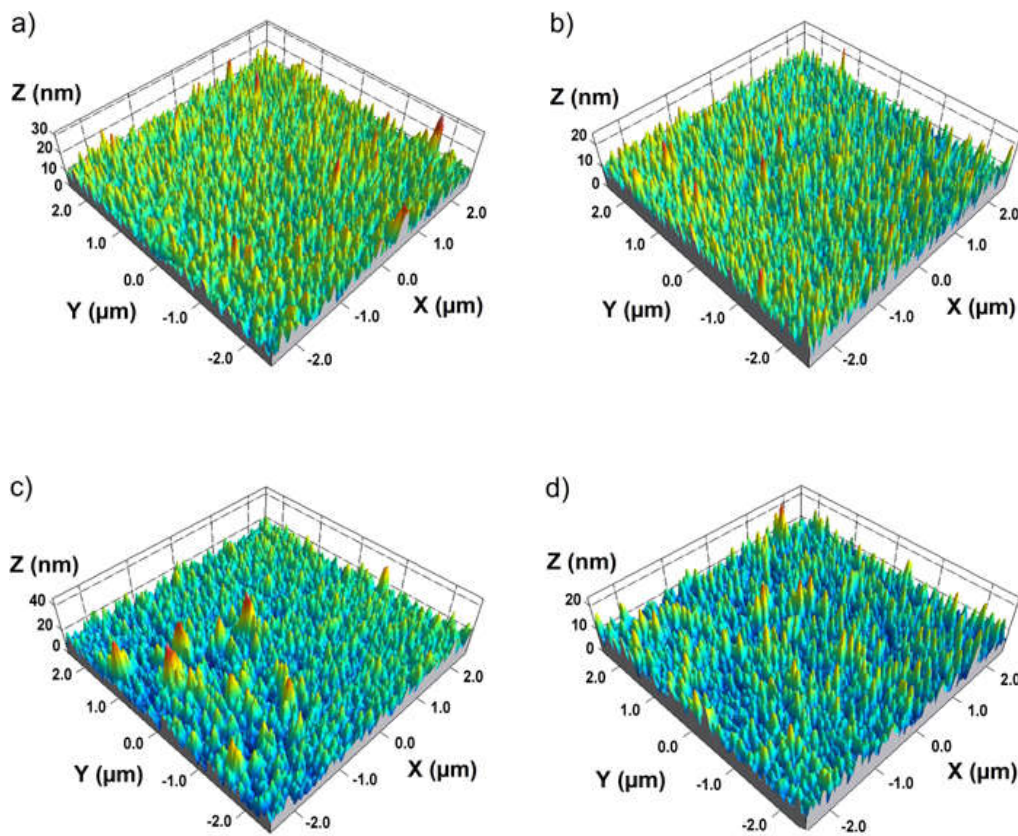


Figure 5.50 Suppression of growth hillock in Al-4B films for sputtering power of: a) 100, b) 130, c) 160 and, d) 200 watts.

Table 5.6 z-range at samples

| Sputtering power (watts) | Aluminum (nm) | Al-4B (nm) | Reduction % |
|--------------------------|---------------|------------|-------------|
| 100 | 159.97 | 18.76 | 88.27 |
| 130 | 225.65 | 16.92 | 92.50 |
| 160 | 233.92 | 33.43 | 85.71 |
| 200 | 207.91 | 15.62 | 92.49 |

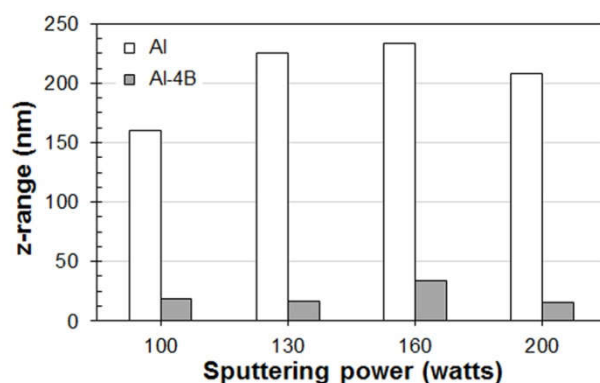


Figure 5.51 High hillock in the samples

5.2.3.3 Average Grain Size

The average grain size (grain diameter) measurement of films was performed on the AFM images with a scanning area of $2.25 \mu\text{m}^2$. Figures 5.52 and 5.53 exemplify how the grain boundaries were outlined in the pure aluminum and Al-4B films, respectively. Afterwards, the diameter was estimated from the area of each grain using the SPIP™ software. Moreover, the sputtering power was also considered in this analysis.

At first, Figure 5.52 shows the aluminum film grains as delimited, displaying variability in size and shape. In the sample deposited at 200 W the average grain size is 152.14 nanometers (Table 5.7). Conversely, the Al-4B films contain grains that are smaller and

more uniform (Figure 5.53). Also, higher deposition power reduced the average grain size. At 200 W the size reduces to 79.20 nm (Table 5.7).

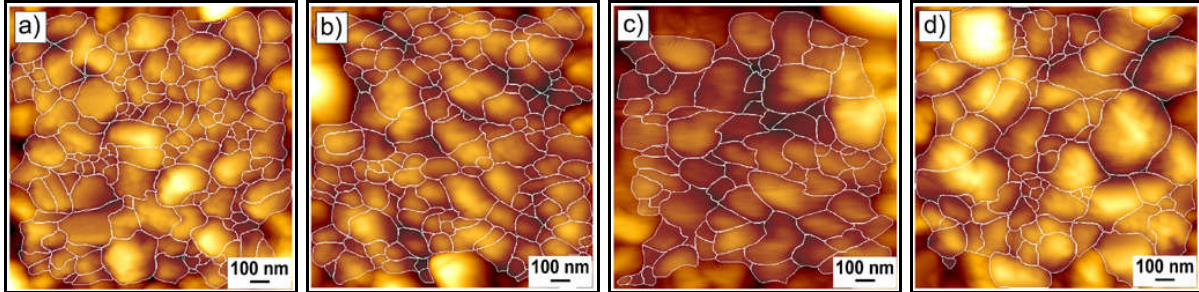


Figure 5.52 Aluminum films grain boundary outline for each sputtering power a) 100 W, b) 130 W, c) 160 W and, d) 200 W.

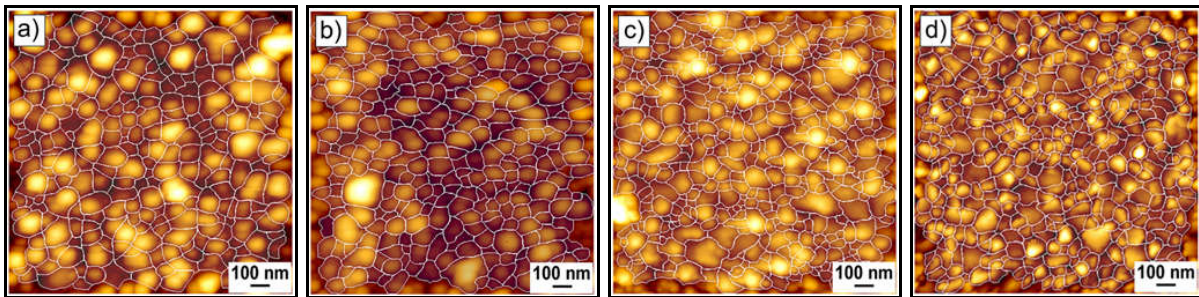


Figure 5.53 Al-4B films grain boundary outline for each sputtering power a) 100 W, b) 130 W, c) 160 W and, d) 200 W.

The films showed heterogeneity in grain size, as evidenced by the coefficient of variation C_v presented in Table 5.7. Since this coefficient indicates how homogeneous or heterogeneous a data series is [111], [112], [141].

Table 5.7 Average grain size results.

| Material Sputtering power (watts) | Al | | | Al-4B | | |
|---|------------------|-------|-------|------------------|-------|-------|
| | Diameter (nm) | STD | C_v | Diameter (nm) | STD | C_v |
| 100 | 117.24 | 57.40 | 0.49 | 97.12 | 31.37 | 0.32 |
| 130 | 118.98 | 46.87 | 0.39 | 90.21 | 24.80 | 0.27 |
| 160 | 150.34 | 66.26 | 0.44 | 75.66 | 29.05 | 0.38 |
| 200 | 152.14 | 86.59 | 0.57 | 79.20 | 20.69 | 0.26 |

Subsequently, a box and whisker diagram allowed observing such grain size dispersion with respect to the median and the average value of grain size (Figure 5.55). This statistical tool allows us to see how the data is not only dispersed from the median (Q_2) but also how such data are distributed around the lower quartile (Q_1), upper quartile (Q_3) and the extremes (X_{min} , X_{max}) or whiskers, as shown in Figure 5.54 [111], [141]. Quartiles Q_1 , Q_2 , and Q_3 represent 25%, 50% and 75% of the ordered data, respectively. The X_{min} is $Q_1 - 1.5 \cdot (Q_3 - Q_1)$ and X_{max} , $Q_3 + 1.5 \cdot (Q_3 - Q_1)$. Also, this plot allows the identification of outliers (x) lying outside the limits $X_{min,max}$.

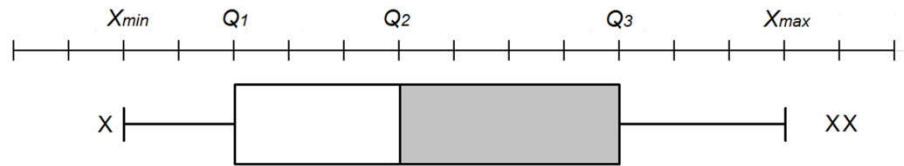


Figure 5.54 Box and whisker plot sketch.

For the aluminum samples, the box size in Figure 5.55 was larger than for the Al-4B specimens, even more for larger sputtering power. It can also be seen that in those aluminum samples the lengths of the upper boxes and whiskers extend more toward the top of the diagram from the median value (Q_2). This indicates graphically that the grain size of these specimens (aluminum) does not display symmetry with respect to the median value and tend to disperse more toward the larger grains. In the case of Al-4B samples, the lengths of the upper and lower boxes in the diagram were smaller and around the same size. Such that, the median (Q_2) lays near the box plot center, which is a feature of the symmetry or homogeneity of the data, in this case, the grain size.

Also, it should be noted that in these films there is a match among the median (Q_2) and the average, which could suggest the homogeneity tends towards in average grain size, unlike aluminum films (Figure 5.55).

Therefore, the diagram boxes enabled us to confirm more effectively the films uniformity of grain size further evinced by the coefficients of variations (C_v) previously calculated in Table 5.7.

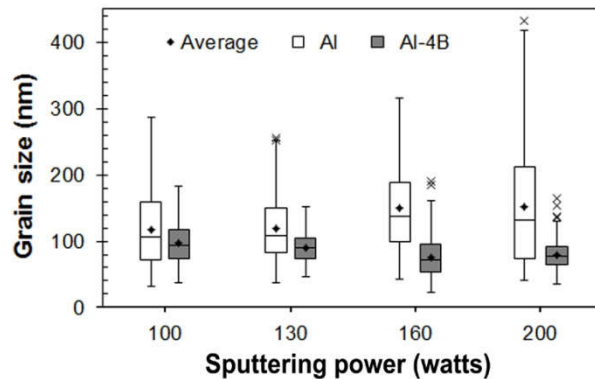


Figure 5.55 Box plots of film grain size.

5.2.3.4 Summary

AFM enabled the study of the films surface morphology, which -according to the results obtained was affected by the manufacturing features, i.e. the material, the film thickness, and the sputtering power. The roughness found in the aluminum films had a relationship with the size of the grain and the hillocks that could be observed in the three dimensional images in Figure 5.49.

Aluminum is a soft material that, when deposited by sputtering, generates diffusion processes between the grains due to the stress relaxation during the film manufacture and the grains junction when the thickness increases, which leads to larger grain size in the films [20], [137], [139], [140]. Also, the sputtering power had an effect on the films grain size, as high power levels yield high sputtered atoms density bearing high energy that reach the substrate, generating high nucleation density which result in to bigger grains [36], [137], [142]–[144]. These aluminum films characteristics were assessed in the AFM images (Figures 5.49 and 5.52) and in the resulting C_v due to the low uniformity in grain size (Table 5.7, Figure 5.55).

On the other hand, the Al-4B films presented an RMS roughness reduction, as well as smaller hillocks and grain size. One must recall that these films were made of a composite (Al-4wt.% B) deposition target where an aluminum matrix reinforced with aluminum diboride particles (AlB_2). The particles embedded in the Al matrix induced changes on the surface morphology of the sputtered film. The film growth depended on the sputtering process affected by the transfer rate of target material onto the substrate (affected by vacuum, pressure, sputtering power) and the surface events such as nucleation, adsorption, reaction, and desorption [53], [110], [145]. Similar findings were reported by Ramos and Suárez in a study of metallic films fabricated with composites target of Al-B-Si deposited on silicon wafer via magnetron sputtering [18]. These composite targets contained AlB_2 and AlB_{12} particles embedded in an aluminum-silicon matrix and, upon pulverization, they generated a smooth film surface compared to the aluminum films surface deposited under the same deposition parameters. However,

their results did not reveal the presence of AlB_2 or AlB_{12} particles or nanoparticles within the thin films.

Other works on metallic films manufactured with aluminum alloys have reported similar results with respect to the surface morphology. Kylner and Mattsson studied aluminum and Al-Cu films deposited on silicon wafer via co-evaporation (two targets) technique [146]. They found that the Al-Cu films grain size had a 50% reduction relative to pure aluminum films grains. The presence of copper solute atoms in the co-evaporated Al-Cu films enabled the formation of small grains. Similarly, another study by Draissilia et al. focused on an aluminum-copper composite target to manufacture Al-Cu films by sputtering; the authors observed via XRD the formation of αAl solution and intermetallic compounds (Cu_3Al , $\theta(\text{Al}_2\text{Cu})$) in the films [147]. Draissilia's results revealed that these combinations promoted the grain refinement in the sputtered films.

Subsequently, another research by Barron introduced alloying elements to the Al-Cu alloy films, namely titanium and chromium [38]. Using AFM images the author observed smaller grain sizes and hillock suppression in the films containing Al-Cu-Ti and Al-Cu-Cr with respect to films made of pure aluminum and Al-Cu. Again, the Cu, Ti or Cr impurities exhibited positive changes in the films morphology resulting in a noticeable decrease in roughness.

In addition, nitrogen and argon atmospheres used in aluminum films sputtering can affect the film nature. For instance, Ishiguro and Miyamura investigated the N_2 effect on the films surface roughness and the substrate temperature [138]. Their AFM image analysis revealed that the films deposited under N_2 atmosphere held a high content of N

(13%) and the substrate at a temperature of 373K showed a flat surface with few protuberances (hillocks). X-ray diffraction results confirmed that these films contained in addition to aluminum, incompletely-formed aluminum nitride.

Previous works demonstrated that impurities present in the target material upon sputtering deposition (of an alloy or composite) and different atmospheres (e.g. nitrogen) can affect the surface morphology of the sputtered films. The films show refinement of grains and a smooth surface reflected in a low roughness. Therefore, the low roughness and grain size of our samples performed to the Al-4B material could be associated with the AlB_2 particles present in the sputtering material, that apparently are causing this effect in the film surface.

5.2.4 Structural Evaluation

The structural evaluation of the films material was studied via x-ray diffraction (XRD) in the samples deposited over glass slide and silicon wafer (100) substrates and for the studied sputtering power (100, 130, 160 and 200 watts). All films studied had a 500 nm thickness.

XRD characterization allowed identifying the constituents and the crystalline grade of the films material from of the interplanar distance (d) and the lattice parameter (a). A Rigaku ULTIMA III diffractometer permitted to collect the diffraction patterns for a 2θ range from 30° to 70° with a step of $2^\circ/\text{minute}$.

The resulting diffractograms are plotted in Figure 5.56 and 5.57 (2θ versus intensity). Aluminum films diffraction patterns present two peaks with weak intensity corresponding to the positions of the (111) and (200) crystallographic planes of aluminum, according to the JCPDS 04-0787 powder diffraction standards (Figure 5.56). The low intensity of the peaks in these films may be indicative of low crystallinity of the film. The aluminum may have amorphization due to high crystalline defect density generated during film formation upon deposition [16], [134], [135].

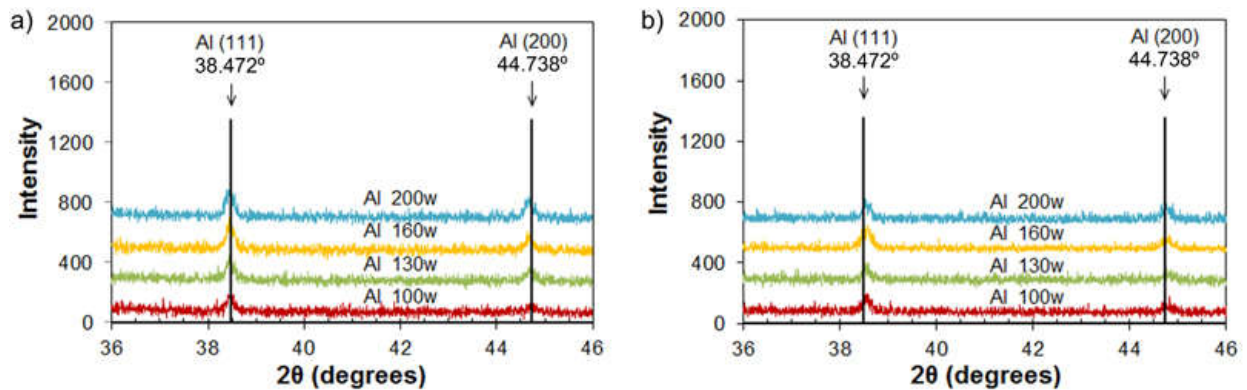


Figure 5.56 X-ray pattern of aluminum films deposited on: a) glass slide and, b) silicon wafer substrates.

In the composite films patterns (Al-4B), only the (111) peak was identified, as the (200) one was not detected, according to Figure 5.57. This could be caused by a preferential orientation (during growth) in the film structure (texture) [32], [93], [110], [148]. In addition, the diffractometer recorded this (111) peak with greater sharpness and intensity (Figure 5.57), compared with the aluminum film (Figure 5.56). Apparently, the Al-4B material during the sputtering by radio frequency (RF) and subsequent deposition on the substrates can have improved the film structure causing this difference.

The sputtering process via RF uses radio waves along with high voltage to generate the electrical field in the vacuum chamber of the deposition system. The high voltage in the RF mode produces high energy ions; thus, such momentum is transferred to the pulverized atoms to be deposited onto the substrate to form the film [53], [109]. The high energy of these sputtered atoms improves the film material crystallinity, which would then be reflected in the diffraction peak intensities [38], [117], [135], [143], [149].

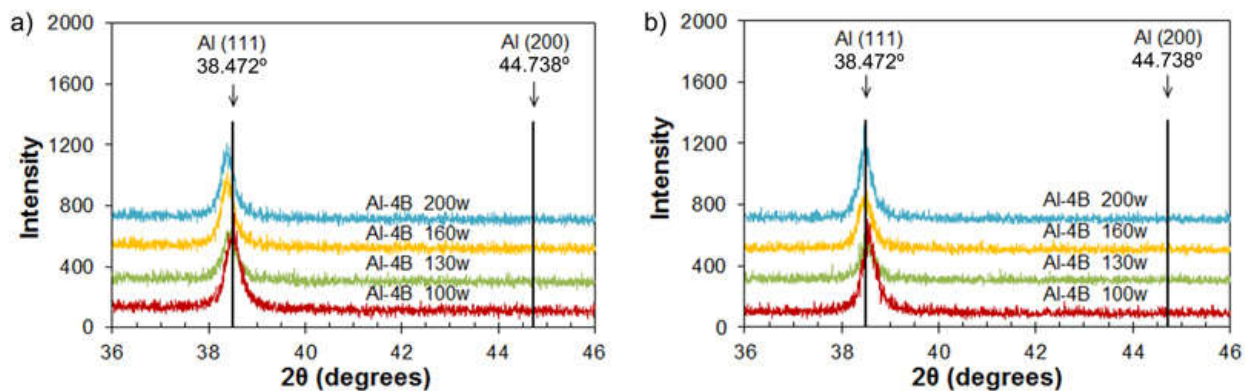


Figure 5.57 X-ray patterns of Al-4B films deposited on: a) glass slide and, b) silicon wafer substrates.

The low crystallinity of the films is manifest in the (111) peak of Figures 5.56 and 5.57. We computed the interplanar distance (d) and the lattice parameter (a) for the cubic structure, according to equations 3-23 and 3-24, respectively. The 2θ value position of the (111) peak was determined using the centroid method (Appendix D).

The results of the (111) peak analysis are summarized in Table 5.8. These were compared with a sample of aluminum powder analyzed with the same Rigaku ULTIMA III diffractometer, using the same $\text{CuK}\alpha$ radiation ($\lambda = 0.15418 \text{ nm}$). The pure aluminum sample represented a reference value of the lattice parameter a , when only the (111) plane position was considered. Normally, the a value indicated by the literature for

aluminum uses more crystallographic planes for its calculation, as the reported in the JCPDS 04-0787.

The pure aluminum powder pattern of Figure 5.58 clearly displays the (111) and (200) peaks in agreement with the diffraction standard JCPDS 04-0787. For this sample, the 2θ position of the (111) peak computed by the centroid method of Appendix D was 38.480° and the subsequent lattice parameter was $a = 0.4052$ nm, using Equation 3-24.

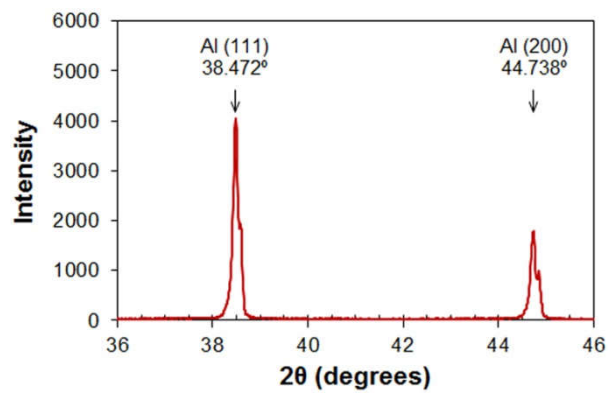


Figure 5.58 Pure aluminum x-ray pattern.

Table 5.8 Lattice parameters measured in the sputtered films.

| Material | Al-4B | | | Al | | |
|-----------------------------|------------------------|-------------|-------------|------------------------|-------------|-------------|
| | 2θ (degrees) | d (nm) | a (nm) | 2θ (degrees) | d (nm) | a (nm) |
| Sputtering power (watts) | | | | | | |
| 100 | 38.568 | 0.2334 | 0.4043 | 38.567 | 0.2334 | 0.4043 |
| 130 | 38.518 | 0.2337 | 0.4048 | 38.556 | 0.2335 | 0.4044 |
| 160 | 38.487 | 0.2339 | 0.4051 | 38.555 | 0.2335 | 0.4044 |
| 200 | 38.489 | 0.2339 | 0.4051 | 38.566 | 0.2334 | 0.4043 |

Figure 5.59 shows the trend of the computed lattice parameter a as a function of the sputtering power. In this figure, the dotted line indicates the lattice parameter value of

the aluminum structure with a high crystallinity obtained from the powder aluminum sample.

In the aluminum films, the lattice parameter was smaller than in the aluminum powder standard, and remained constant for all the sputtering power levels studied. This trend may be an indication that the crystals of these films are strained, with lower crystallinity. This deformation is the result of internal or residual stresses that occurred during the deposition process of the film, affecting the material crystalline structure [18], [120], [149], [151]. In addition, the lattice parameter reduction in these aluminum films suggests the formation of small crystals, which led to the weak intensity of the (111) peak in the diffraction patterns (Figure 5.56) [16].

The lattice parameter of the films made with the Al-4B target displayed a different behavior than the sputtered pure aluminum films (Figure 5.59). As the sputtering power increased, the lattice parameter neared the one in the pure aluminum powder, i.e. 0.4052 nm. At 200 watts deposition power, the lattice parameter in this film reached 0.4051 nm (Table 5.8). Hence, the Al-4B film sputtered at that sputtering power showed less crystal strain as a result of residual stresses. Further, at lower sputtering power this phenomenon was not observed.

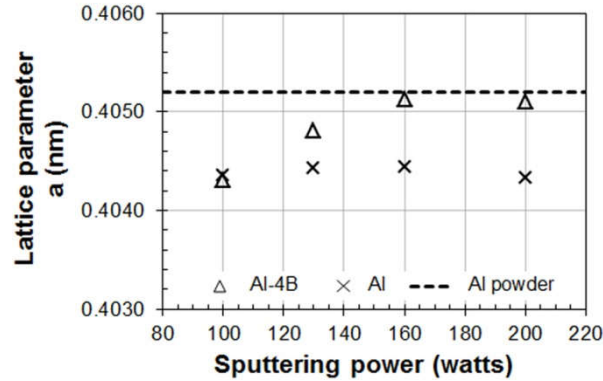


Figure 5.59 Lattice parameter a as function of sputtering power.

5.2.4.1 Summary

The results obtained in the evaluation of the structure of the films using XRD revealed that the Al-4B composite target had a better performance under the sputtering parameters used in this study when compared with the films prepared with pure Al targets. In particular, the sample deposited at 200 watts possessed less strain, as revealed by the computed parameter value, which was close to that of pure aluminum. Consequently, the morphological surface texture, i.e. (111) plane, of the material would present grains with smaller defect density [18], [98]. Therefore, we can assume that the mechanical properties and surface morphology improvement found in Al-4B film deposited at 200 watts in the sections 5.2.2 and 5.2.3 of this thesis may also be associated to the crystalline structure produced in the material during the film growth on the substrate via RF sputtering.

5.2.5 Study of Temperature Effect

The temperature effects study in the thin films was carried out in a sample made of the Al-4wt. %B (Al-4B) target material deposited on the silicon substrate via a 200 watts sputtering power and with a 500 nm film thickness. As presented in the previous

sections, this material was selected because it displayed the best mechanical behavior with a good surface morphology and structural performance (sections 5.2.2, 5.2.3 and 5.2.4).

This research segment focused on the mechanical properties and structural evaluation of the film material using nanoindentation and x-ray diffraction, respectively.

In parallel, a reference sample was manufactured with pure aluminum under the same deposition parameters.

5.2.5.1 Mechanical Properties

The mechanical properties on the films were examined with the G200 nanoindenter. The instrument permitted to determine elastic modulus (E) and hardness (H) using its *hot stage hardness and modulus* method (HS-HM) provided by its proprietary software (NanoSuite®), using the load control mode for a temperatures sequence of 28°, 75°, 100°, 150°, and 180°C. After the heating cycle, a measurement was performed at room temperature (28°C). The properties were measured at an approximate indentation depth of 300 nm.

The analysis via load control mode considers the substrate effect. Hence, the resulting mechanical properties are the result of the combined action and interaction between the film material and the substrate [57], [59].

Table 5.9 shows the average results of the indentation load peak (P_{\max}) and depth (h_{\max}) values recorded on each sample for the temperature levels considered at the test.

In the aluminum sample, the temperature reduced the load capacity registered at the aforementioned indentation depth. The load fell from 6.23 mN at 28°C to 2.59 mN at 180°C. In addition, after the heating cycle, the sample attained a load capacity of 6.23 mN measured at room temperature. This could suggest that the sample material did not experience any annealing, as no significant load capacity change was recorded. It is known that annealing can affect the microstructure, hence the mechanical strength [153], which apparently was not the case in this specimen.

In contrast, the loading results in Al-4B sample showed a rather different behavior than the aluminum specimen in this hot stage nanoindentation test (Table 5.9). The load capacity values remained high 12.5 mN for each temperature level tested. Therefore, one could infer that in this material, the load capacity was not affected significantly by heating.

Figures 5.60, 5.61, and 5.62 show three instances of the nanoindentation characteristic curves (load versus displacement) captured on the Al-4B and aluminum samples at 28°C (start of the test), 180°C (peak heating) and at end of the test, when the sample was cooled to room temperature (28°C), respectively. Al-4B curves are qualitatively similar, with small differences. Instead, the aluminum curves are remarkably different, as a result of the higher temperature.

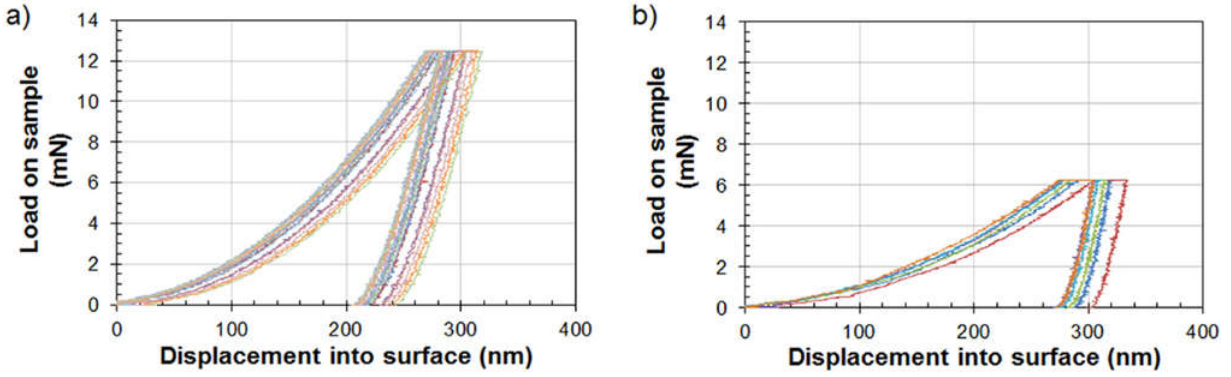


Figure 5.60 Characteristic nanoindentation curve at 28°C in: a) Al-4B and, b) aluminum film samples.

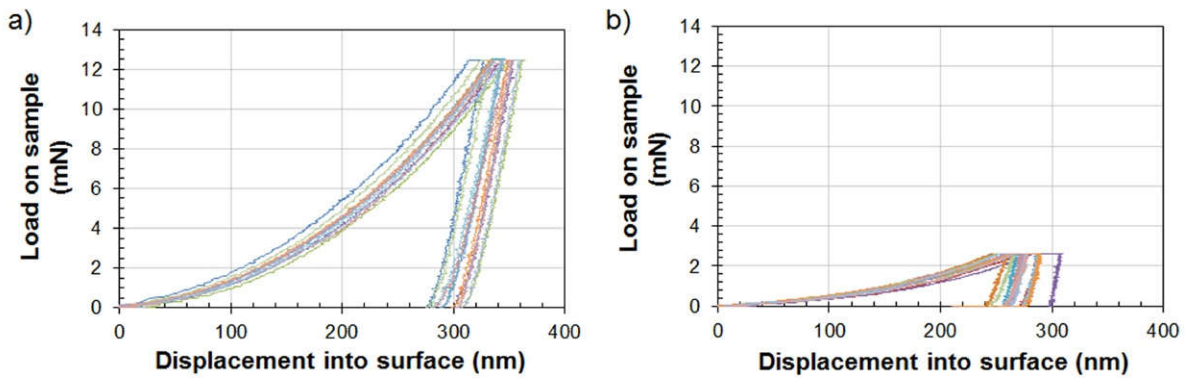


Figure 5.61 Characteristic nanoindentation curves at 180°C in: a) Al-4B and, b) aluminum film samples.

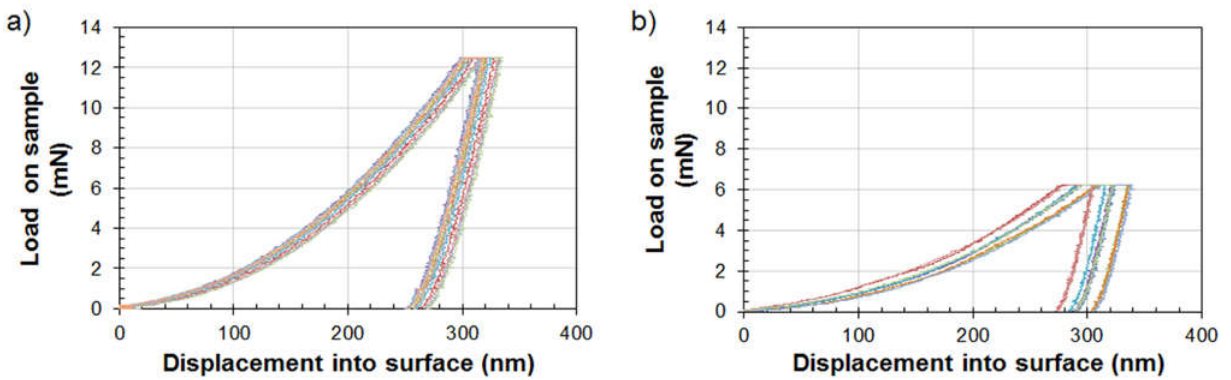


Figure 5.62 Characteristic nanoindentation curve at 28°C after heating cycle: a) Al-4B and, b) aluminum film samples.

Table 5.9 Summary average results of load and displacement measured on the heated samples using the G200 nanoindenter.

| Sample | Al-4B | | | | Al | | | |
|---------------------|--------------------------|------|--------------------------|-------|--------------------------|------|--------------------------|-------|
| Property | Load | | Displacement | | Load | | Displacement | |
| Temperature (°C) | P _{max} (mN) | STD | h _{max} (nm) | STD | P _{max} (mN) | STD | h _{max} (nm) | STD |
| 28 | 12.47 | 0.02 | 290.31 | 14.22 | 6.23 | 0.01 | 317.97 | 11.85 |
| 75 | 12.47 | 0.02 | 290.84 | 17.60 | 5.19 | 0.01 | 321.55 | 13.95 |
| 100 | 12.48 | 0.02 | 324.36 | 13.94 | 4.15 | 0.01 | 307.02 | 22.54 |
| 150 | 12.48 | 0.01 | 345.76 | 15.81 | 2.90 | 0.00 | 285.14 | 17.65 |
| 180 | 12.40 | 0.16 | 345.76 | 15.81 | 2.59 | 0.00 | 287.38 | 21.71 |
| *28 | 12.48 | 0.02 | 322.20 | 8.94 | 6.23 | 0.01 | 328.54 | 38.68 |

*Temperature after the heating cycle, STD:standard deviation,

The loading capacity of the specimens is linked to the elastic modulus of the material. Figure 5.63 presents the trend of this module under the temperature effects upon the experiment.

The elastic modulus of the aluminum sample decreased with increasing temperature (Figure 5.63b): from 217.23 GPa at room temperature to 115.62 GPa at 180°C (Table 5.10). This modulus cutback was also noted by Rathinam et al. in the single crystal aluminum (100) study using the HS-HM technique in nanoindentation [154]. They found that under the same indentation load, the modulus degraded at elevated temperature due to the material softening, which reflected in one larger penetration depth. In our case, the softening was manifest in the lower load capacity recorded upon the same indentation (Table 5.9). As the sample heats, thermal expansion occurs accompanied by a material softening [153]–[156]. Additionally, at the end of the test (room temperature) the heated sample reached a modulus of 190.69 GPa (Table 5.10). This value was lower than the one at the beginning of the experiment. Consequently, this slight reduction in the elastic modulus might connote an annealing effect due to the

increase in temperature (heat treatment) [153]–[156], although the load capacity results indicated otherwise. This possible annealing effect was analyzed in the following section of this thesis (section 5.2.5.2), which is related to the structural evaluation of sample material using the high temperature x-ray diffraction technique. As mentioned above, annealing may affect the microstructure of the material.

In the Al-4B sample, the measurement of the elastic modulus revealed an unexpected behavior, which had been previously perceived in the load capacity results. The modulus was slightly affected by the temperature (Figure 5.63a). For each temperature level, the modulus was approximately 185 GPa (Table 5.10).

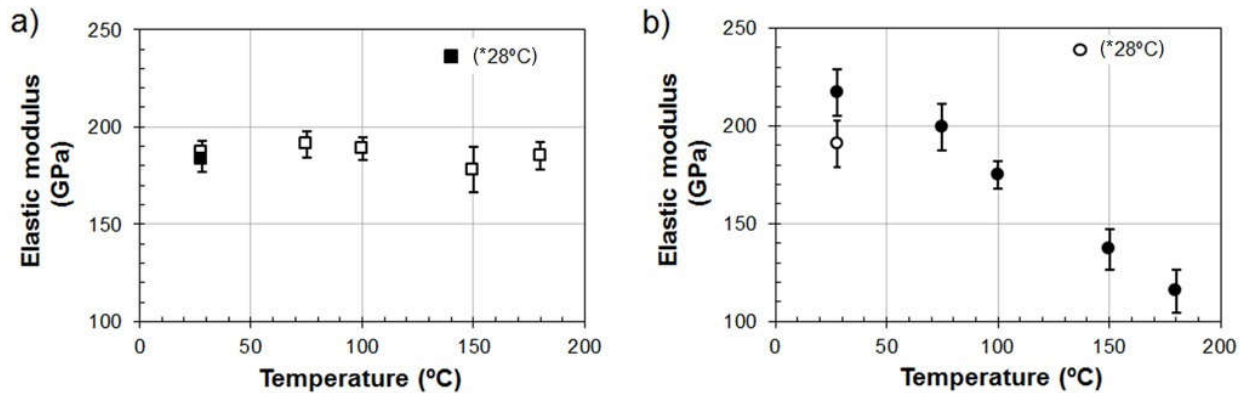


Figure 5.63 Temperature effects in elastic modulus to nanoscale on: a) Al-4B and, b) aluminum films.

Table 5.10 Mechanical properties measured in the sputtered films subjected to heating cycle by nanoindentation.

| Material | Al-4B | | | | Al | | | |
|------------------|-----------------|-------|----------|------|-----------------|-------|----------|------|
| | Elastic modulus | | Hardness | | Elastic modulus | | Hardness | |
| Property | Avg E | STD | Avg H | STD | Avg E | STD | Avg H | STD |
| Temperature (°C) | GPa | | GPa | | GPa | | GPa | |
| 28 | 187.13 | 17.21 | 7.81 | 0.85 | 217.23 | 22.44 | 2.70 | 0.22 |
| 75 | 191.11 | 13.96 | 7.80 | 1.18 | 199.24 | 32.76 | 2.18 | 0.21 |
| 100 | 188.80 | 12.51 | 7.30 | 0.75 | 174.98 | 22.84 | 1.93 | 0.32 |
| 150 | 177.90 | 24.86 | 5.96 | 0.58 | 136.85 | 23.13 | 1.56 | 0.09 |
| 180 | 186.85 | 19.70 | 4.92 | 0.20 | 115.62 | 10.93 | 1.38 | 0.20 |
| *28 | 183.21 | 14.14 | 5.97 | 0.34 | 190.69 | 29.12 | 2.61 | 0.44 |

*Temperature after the heating cycle, Avg: average, STD: standard deviation.

The nanoindentation technique calculates the elastic modulus from the load versus displacement curve at the beginning of the unloading stage as the indenter starts withdrawing from the sample surface (Figure 3.4a). Upon unloading the nanoindenter apparatus records the elastic recovery of the material, which regulates the contact depth (h_c) and unloading stiffness (S). These parameters are used for the calculation of this elastic modulus (Section 3.3.1).

Accordingly, an elastic recovery analysis was conducted at the temperature levels shown in Figures 5.60, 5.61, and 5.62 (extreme points). The analysis used the normalized data of these curves as a function of the load and maximum displacement values reached for each indentation (relative elastic recovery) [26].

Figures 5.64, 5.65 and 5.66 display characteristic normalized curves for those temperatures, where the black dots on the x-axis (h/h_{\max}) identify the relative elastic recovery and are plotted in Figure 5.67. Here, we can observe the tendency of the relative elastic recovery as a result of the temperature change. In both materials, as expected, the temperature reduced the relative elastic recovery [26].

The aluminum sample showed lower relative elastic recovery compared to the Al-4B sample. This performance is associated to the hardness and stiffness of the film material [124], [125]. Accordingly, the smaller elastic modulus in the aluminum sample occurred as the contact depth (h_c) and the unloading stiffness (S) were increased, i.e. there was greater plastic deformation. In the Al-4B sample, despite smaller elastic recovery (Figure 5.67), the elastic modulus was slightly affected (Figure 5.63).

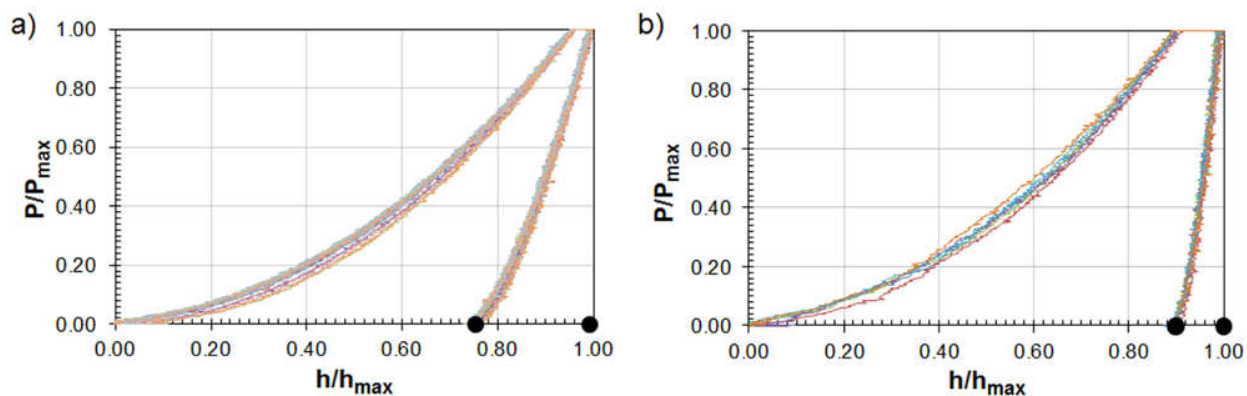


Figure 5.64 Characteristic normalized nanoindentation curve at 28°C in: a) Al-4B and, b) aluminum film samples.

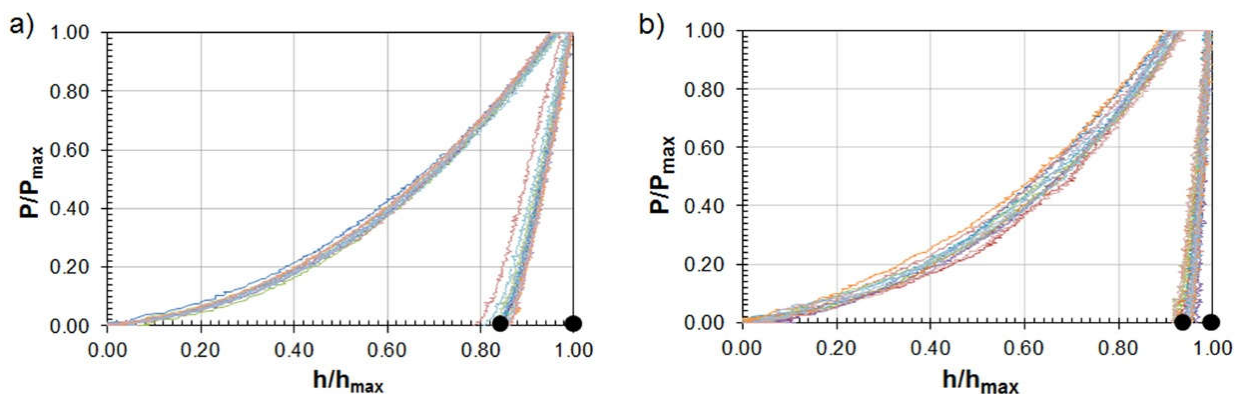


Figure 5.65 Characteristic normalized nanoindentation curve at 180°C in: a) Al-4B and, b) aluminum film sample

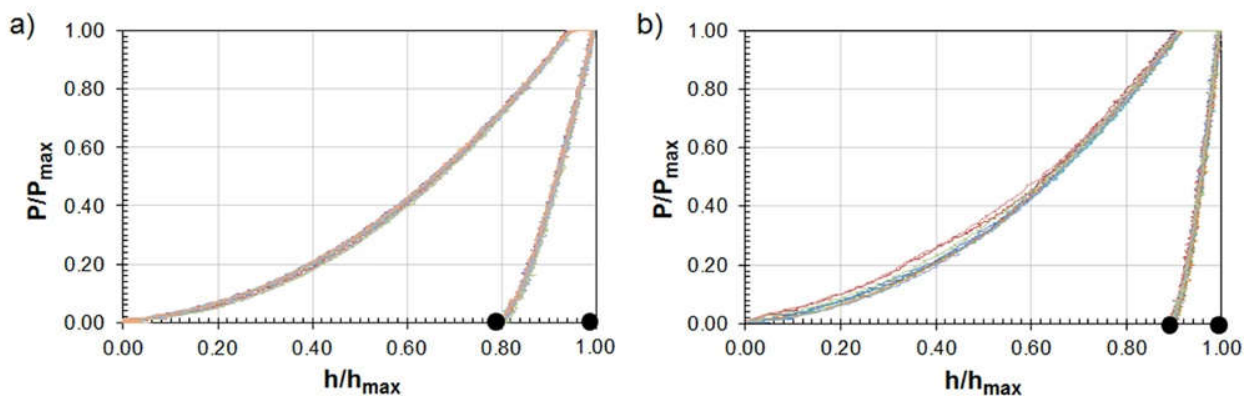


Figure 5.66 Characteristic normalized nanoindentation curve after heating cycle (at 28°C): a) Al-4B and, b) aluminum film samples.

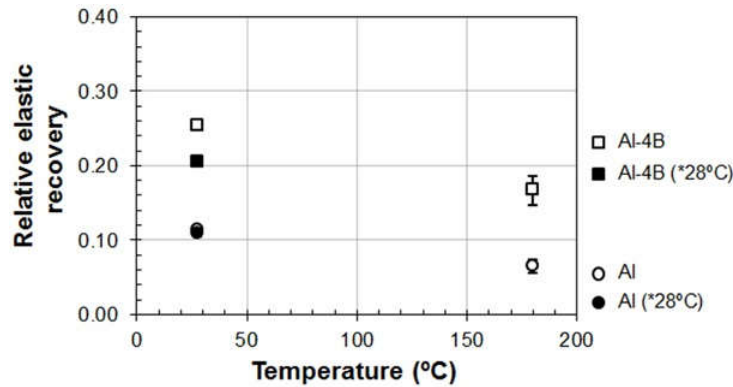


Figure 5.67 Relative elastic recovery for the temperature extreme points.

Hardness was calculated as the ratio between the indentation load peak (P_{max}) obtained in the loading process at the experiment and the contact area (A_c), as a function of h_c (equation 3-2). The results shown in Figure 5.68 depict how the hardness decreases as a function of temperature. As previously mentioned, h_c depends on the elastic recovery of the material during the unloading stage of the indentation. For the aluminum sample, the trend observed in hardness was directly related to the load cutback (Table 5.9) and relative elastic recovery.

Similarly, the Al-4B sample showed a similar hardness behavior, although in this case the result did not depend on the load, since this was kept constant at each temperature level analyzed in the experiment (Table 5.9). The load peak (P_{max}) recorded reflects the elastic modulus behavior, which was slightly affected by the temperature (Figure 5.63). Thus, the loss in hardness is attributed to the reduction of the relative elastic recovery in this sample, which increases the h_c and S , leading to a greater A_c .

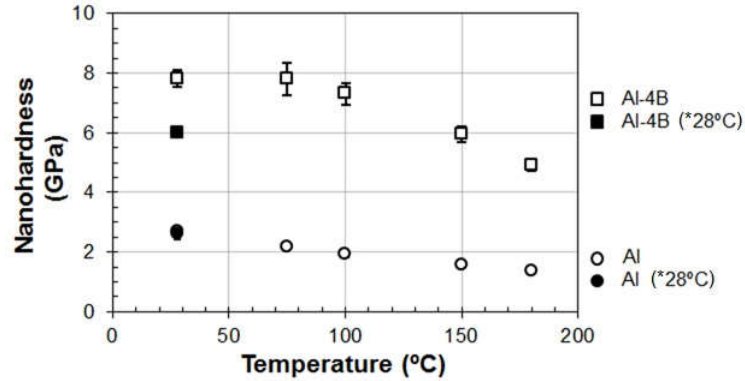


Figure 5.68 Temperature effect on the hardness measured via nanoindentation.

The mechanical behavior of the Al-4B material in the hot stage nanoindentation experiment showed a discrepancy related to the trend of the elastic modulus and hardness results. It was expected that these two properties decrease with increasing temperature, as was observed in the aluminum sample findings [153], [154], [156]. The discrepancy between these two properties as a function of temperature effect in the Al-4B sample can be explained from the standpoint of the effective modulus (E_{eff}), which is used to determine the modulus of elasticity from the nanoindentation methodology (section 3.3.1). E_{eff} is calculated by equation 3-4, which involves the $S \cdot A_c^{-0.5}$ ratio. The unloading stiffness (S) and the contact area ($A_c = F(h_c)$) values are obtained upon the unloading stage of the nanoindentation curve (Figure 3.4). As observed in Figure 5.65, the elastic recovery decreased at 180°C. Consequently, the parameters h_c , S and A_c augmented. This increase in S and A_c possibly caused a slight change in the $S/A_c^{0.5}$ ratio, leading to an E_{eff} relatively invariant with little effect on the elastic modulus. At 180°C, the elastic modulus was 186.85 GPa nearing the 187.13 GPa value obtained at room temperature (28°C) (Table 5.10). All things considered, the results of the elastic

modulus at other temperatures apparently exhibited this same invariant behavior of the E_{eff} , which led to a similar elastic modulus outcome (Table 5.10).

In closing this temperature analysis by nanoindentation, it could be noticed that the properties of the samples were affected to a greater or lesser extent by the temperature cycle used in the experiment.

5.2.5.2 Structural Evaluation

The structural evaluation of the samples was studied on the temperature effect on the interplanar distance (d) and the lattice parameter (a) of the unit cell of the material structure (Al-4B and aluminum film). In situ high temperature x-ray diffraction (HT-XRD) was used for this aim. Both parameters were calculated from the equations 3-20 and 3-21, respectively.

The scanning for 2θ at the diffractometer Rigaku ULTIMA III using Reactor X module was carry out between the 30 and 70 degrees with a step of 2° /minute for the temperature sequence of 28° and 200°C , and 28°C after the heating cycle ($*28^\circ\text{C}$).

The structural analysis of the samples was performed considering only the peak of the crystallographic plane (111), being consistent with the structural evaluation of the films in section 5.2.4 of this thesis. Accordingly, Figure 5.69 shows only the 2θ range where this peak is located. For each temperature level and sample, the 2θ value of peak was computed by the centroid method (Appendix D).

Figure 5.69 shows the in situ high temperature x-ray diffraction patterns collected in the studied samples. In this figure, the intensity of peak in the diffractograms in both

samples did not show significant differences as consequence of the temperature sequence used in the test. Apparently the material crystallinity was unaffected by the temperature increasing, since the intensity of the diffracted rays may vary because of crystallographic defects in the sample material [38], [135], [143], [149], [157]. Also, in the figure can be seen as this peak shifts to the left when the temperature increases of 28° up 200°C. This displacement suppose there is an endothermic process in which the structure of the material expands due heating [158], [159]. After heating, the peak was shifted to the right in the test carried out at room temperature (*28°C), it shown in the curve corresponding to the third pattern of the stack in Figure 5.69.

The lattice parameter (a) was calculated for each temperature levels used in the x-ray diffraction test with hot stage (HT-XRD). The results are summarized in Table 5.11 and were plotted as function of temperature in Figure 5.70.

In the aluminum sample, the a parameter changed from 0.4050 nm at 28°C to 0.4067 nm at 200°C (Table 5.9). It is expanded 0.41%. For this same temperature range, the a parameter in the Al-4B sample raised from 0.4065 up 0.4086 nm. The expansion percentage was 0.50%. The results revealed that the Al-4B material has shown a higher susceptibility to thermal expansion related with lattice parameter (a) calculated regarding at (111) peak.

After of heating, the lattice parameter result to room temperature (*28°C) for the aluminum and Al-4B sample was of 0.4047nm and 0.4058 nm, respectively. These values were lowers to lattice parameter outcomes obtained at test before temperature cycle (Table 5.11). Therefore, the crystalline structure of the Al-4B and aluminum

material in the samples was affected by the increase of the temperature, which means that the sample was subjected to an annealing process (heat treatment).

In addition, the heat treatment may cause residual stresses relaxation produced in the film material when it was manufactured by sputtering. As mentioned in the literature, the residual stresses generate crystallographic defect in the structure of the film material [18], [121], [149], [152], [160]. In 2009, Matsue et al. reported that the temperature relieved the thin film residual stresses of TiN using the Synchrotron radiation technique [161]. Considering this, the contraction exhibited by the lattice parameter in the studied samples by the x-ray diffraction with hot stage may be associated to a possible structural rearrangement of material, as a result of the relaxation of residual stresses.

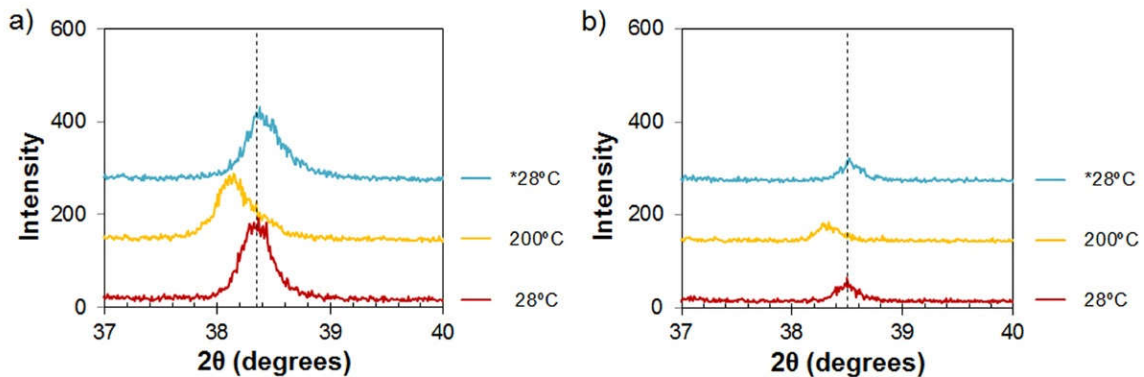


Figure 5.69 In-situ high temperature x-ray diffraction pattern of the samples: a) Al-4B and, b) aluminum

Table 5.11 Lattice parameters measured in the sputtered films for the heating cycle at HT-XRD.

| Material Temperature (°C) | Al-4B | | | Al | | |
|---------------------------------|------------------------|-------------|-------------|------------------------|-------------|-------------|
| | 2θ (degrees) | d (nm) | a (nm) | 2θ (degrees) | d (nm) | a (nm) |
| 28 | 38.351 | 0.2347 | 0.4065 | 38.500 | 0.2338 | 0.4050 |
| 200 | 38.176 | 0.2357 | 0.4083 | 38.315 | 0.2349 | 0.4069 |
| *28 | 38.422 | 0.2343 | 0.4058 | 38.530 | 0.2336 | 0.4047 |

*Temperature after of heating cycle

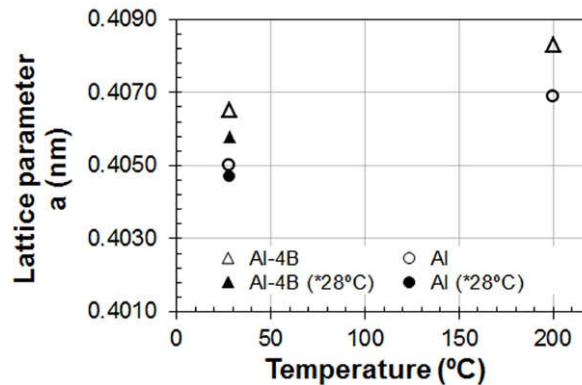


Figure 5.70 Film lattice parameter (a) at different temperatures.

5.2.5.3 Summary

The results found in the lattice parameter (a) in the samples for each temperature level studied in the HTXRD test revealed expansion and contraction processes in the crystalline structure of specimens material during heating and subsequent cooling at room temperature, respectively (Table 5.9). Furthermore, the expansion of the lattice parameter obtained from the HT-XRD technique data demonstrated that the samples soften during the heating process. This was reflected in the reduction of elastic recovery and mechanical properties determined via nanoindentation with HS-HM method.

At the end of the experiment, the materials of the samples exhibited a reduction of the lattice parameter; the crystalline structures were affected by the increasing temperature (annealed sample). Notwithstanding, the annealing of the material possibly caused the decrease of the mechanical properties of the samples due to the contraction of the structure of the material. In relation to this, Beak and Smith found that the temperature increase applied on a gold sample during the hot stage nanoindentation reduced the

hardness and elastic modulus obtained in the sample, when was tested at room temperature again. The material changed from work-hardened to annealed [155].

Therefore, the results obtained in the hot phase tests via nanoindentation and x-ray diffraction in the studied samples (aluminum and Al-4B) evidenced that the temperature cycle affected the mechanical behavior associated with changes in the material structure.

6 CONCLUSIONS

The fabrication and characterization carried out in this research from an aluminum matrix reinforced with AlB_2 particles (Al-4wt. % B) in bulk samples and thin films manufactured by centrifugal casting and magnetron sputtering, respectively, revealed that the reinforcement particles embedded in the aluminum matrix of the deposition target and the sputtering power significantly influenced the thin films overall performance. Concerning this, the outstanding conclusions are presented as follows:

The hardness experiment, i.e. Brinell hardness and nanoindentation tests using continuous stiffness measurement method (on the bulk samples), demonstrated the reinforcing effect of the boride particles embedded pure aluminum matrix as result of particle / matrix interaction.

Nanoindentation also revealed that the aluminum matrix in the composite did not undergo any hardening and strengthening as a consequence of the AlB_2 particles or due to the amount of particles present in the composite.

The centrifugal casting process use in the fabrication of the sputtering targets favored the segregation of the reinforcing, denser particles, reduced the porosity of the casting, and improved the material hardness compared to gravity cast specimens.

The magnetron sputtering unit operated in radio frequency mode enabled the manufacturing of thin films of the Al-4wt. % B composite material (Al-4B) on two substrates (silicon wafer and glass slide) from the centrifugally-cast deposition target.

Nanoindentation experiments revealed that the Al-4B composite thin films were harder and stiffer, with greater scratch strength than pure aluminum thin films for the same processing conditions.

The methodology proposed related to the adhesion strength determination used on thin films of aluminum and Al-4B subjected to scratching by nanoindentation was suitable, considering the mechanism involved as the chip-shaped material was separated from the film, which is a characteristic of ductile materials.

The films deposited with the composite material (Al-4wt. % B) presented smaller grains, less RMS roughness and hillock suppression. These findings were reached at the highest level of sputtering power used in the manufacturing of the samples.

The samples structural evaluation via x-ray diffraction revealed a film growth preferred orientation along the (111) crystallographic plane of the pure aluminum in specimens deposited using the composite target (Al-4B). Additionally, the samples presented a less crystal strain as the sputtering power increased compared with pure aluminum films.

Hot stage nanoindentation and high temperature x-ray diffraction revealed that the material of the studied samples was softened due the temperature increase that expands the material structure affecting the mechanical behavior. Additionally, the samples exhibited annealing leading to a reduction in the mechanical strength and to less lattice strain.

The characterization carried out in the samples studied in this research revealed that the Al-4B composite in the thin film deposited by sputtering at a power of 200 watts, presented the best mechanical, morphological and structural performance compared to the aluminum samples, and even under the temperature effects in the hot stage tests, as a result associated to the AlB_2 particles present in the deposition target. Considering these cumulative discoveries, one can confidently propose that this material be considered as an alternative to aluminum in the microelectromechanical systems applications.

7 FUTURE WORK

The Al-4B material was proposed in this dissertation as an appealing alternative to aluminum for electrical interconnection of layers in microelectromechanical systems. To this end, the material should be electrically characterized in thin films manufactured at 200 watts of sputtering power using radio frequency.

In addition, the samples characterization could include a finite element analysis of the nanoindentation process, which would allow to predict the stresses distribution during loading and unloading in the indentation on the material considering the indenter shape and the nature of the substrate.

8 REFERENCES

- [1] K. U. Kainer, *Metal Matrix Composites: Custom-made Materials for Automotive and Aerospace Engineering*. Wiley, 2006.
- [2] H. E. Calderón, “Efectos de la Deformación Mecánica sobre Compuestos de Matriz de Aluminio Tratados Térmicamente,” M.S. tesis, Depto. Ing. Mec., Univ. Puerto Rico, Mayagüez, PR, 2004.
- [3] Y. Fukui, “Fundamental Investigation of Functionally Gradient Material Manufacturing System using Centrifugal Force,” *Japan Soc. Mech. Eng.*, vol. 34, no. 1, pp. 144–148, 1991.
- [4] M. Schwartz, *New Materials, Processes, and Methods Technology*. CRC Press, 2005.
- [5] C. G. Kang and P. K. Rohatgi, “Transient thermal analysis of solidification in a centrifugal casting for composite materials containing particle segregation,” *Metall. Mater. Trans. B*, vol. 27, no. 2, pp. 277–285, 1996.
- [6] Z. H. Melgarejo, O. M. Suárez, and K. Sridharan, “Microstructure and properties of functionally graded Al-Mg-B composites fabricated by centrifugal casting,” *Compos. Part A Appl. Sci. Manuf.*, vol. 39, pp. 1150–1158, 2008.
- [7] T. K. Adelakin and O. M. Suárez, “Study of Boride-Reinforced Aluminum Matrix Composites Produced via Centrifugal Casting,” *Mater. Manuf. Process.*, vol. 26, pp. 338–345, 2011.
- [8] W. Kai, X. U. E. Han-song, Z. O. U. Mao-hua, and L. I. U. Chang-ming, “Microstructural characteristics and properties in centrifugal casting of SiCp/Zr104 composite,” *Trans. Nonferrous Met. Soc. China*, vol. 6326, no. 9, pp. 2–7, 2009.
- [9] J. R. Gomes, L. A. Rocha, S. J. Crnkovic, R. F. Silva, and A. S. Miranda, “Friction and Wear Properties of Functionally Graded Aluminum Matrix Composites,” *Mater. Sci. Forum*, vol. 423–425, pp. 91–96, 2003.
- [10] Y. Watanabe, H. Sato, and Y. Fukui, “Wear Properties of Intermetallic Compound Reinforced Functionally Graded Materials Fabricated by Centrifugal Solid-particle and In-Situ Methods,” *J. Solid Mech. Mater. Eng.*, vol. 2, no. 7, pp. 842–853, 2008.
- [11] G. Ramos, R. Manzano, and O. M. Suárez, “A comparative hardness study of Al-Si/AIB₂ and Al-Si/AIB₁₂ composites,” *Sci. Eng. Compos. Mater.*, vol. 19, no. 1, pp. 67–73, Jan. 2012.
- [12] J. Rodríguez, M. a. Garrido-Maneiro, P. Poza, and M. T. Gómez-del Río, “Determination of mechanical properties of aluminium matrix composites constituents,” *Mater. Sci. Eng. A*, vol. 437, no. 2, pp. 406–412, Nov. 2006.

- [13] Z. H. Melgarejo, P. J. Resto, D. S. Stone, and O. M. Suárez, "Study of particle-matrix interaction in Al/AlB₂ composite via nanoindentation," *Mater. Charact.*, vol. 61, no. 2, pp. 135–140, Feb. 2010.
- [14] E. R. Olivas, J. G. Swadener, and Y.-L. Shen, "Nanoindentation measurement of surface residual stresses in particle-reinforced metal matrix composites," *Scr. Mater.*, vol. 54, pp. 263–268, 2006.
- [15] M. Farooq and Z. H. Lee, "Optimization of the Sputtering Process for Depositing Composite Thin Films," *J. Korean Phys. Soc.*, vol. 40, no. 3, pp. 511–515, 2002.
- [16] S. H. Jeong, S. Kho, D. Jung, S. B. Lee, and J. Boo, "Deposition of aluminum-doped zinc oxide films by RF magnetron sputtering and study of their surface characteristics," *Surf. Coat. Technol.*, vol. 175, no. 3, pp. 187–192, 2003.
- [17] Z. Wu *et al.*, "Al-Mg-B thin films prepared by Magnetron Sputtering," *Vacuum*, vol. 85, pp. 541–545, 2010.
- [18] G. Ramos and O. M. Suárez, "Characterization of sputtered Al-B-Si thin films produced with composite targets for device applications," *Sci. Eng. Compos. Mater.*, vol. 19, no. 2, pp. 93–99, Jan. 2012.
- [19] Z. Xin, L. Qian, W. Zijng, W. Xiaojing, S. Weidian, and J. Bin, "Nanoindentation study of a Cu/Ta/SiO₂/Si multilayer system," *J. Semicond.*, vol. 33, no. 4, pp. 1–6, 2012.
- [20] P. Quintana, A. I. Oliva, O. Ceh, and J. E. Corona, "Thickness effects on aluminum thin films," *Superf. y Vacío*, vol. 9, pp. 280–282, 1999.
- [21] J. E. Jakes and D. S. Stone, "The edge effect in nanoindentation," *Philos. Mag.*, pp. 1–13, 2010.
- [22] J. E. Jakes *et al.*, "Nanoindentation near the edge," *J. Mater. Res.*, vol. 24, no. 3, pp. 1016–1031, 2009.
- [23] D. Beegan, S. Chowdhury, and M. T. Laugier, "Comparison between nanoindentation and scratch test hardness (scratch hardness) values of copper thin films on oxidised silicon substrates," *Surf. Coat. Technol.*, vol. 201, pp. 5804–5808, 2007.
- [24] X. Li, B. Bhushan, K. Takashima, C. Baek, and Y. Kim, "Mechanical characterization of micro/nanoscale structures for MEMS/NEMS applications using nanoindentation techniques," *Ultramicroscopy*, vol. 97, pp. 481–494, 2003.
- [25] A. S. Bhattacharyya and S. K. Mishra, "Micro/nanomechanical behavior of magnetron sputtered Si-C-N coatings through nanoindentation and scratch tests," *Micromechanics and Microengineering*, vol. 21, pp. 1–8, 2011.
- [26] Y. Zhang, Y. Cheng, and D. S. Grummon, "Indentation stress dependence of the temperature range of microscopic superelastic behavior of nickel-titanium thin

- films,” *J. Appl. Phys.*, vol. 98, pp. 1–4, 2005.
- [27] A. J. Muir Wood and T. W. Clyne, “Measurement and modelling of the nanoindentation response of shape memory alloys,” *Acta Mater.*, vol. 54, pp. 5607–5615, 2006.
- [28] S. J. Krumbein, “Metallic electromigration phenomena,” in *IEEE Transactions on Components, Hybrids, and Manufacturing Technology*, 1988, vol. 11, no. 1, pp. 5–15.
- [29] J. R. Black, “Mass transport of aluminum by momentum exchange with conducting electrons,” in *6th International Reliability Physics Symposium*, 1967, no. 7, pp. 148–159.
- [30] C. Witt, “Electromigration in Bamboo Aluminum Interconnects,” Ph.D dissertation, Univ. Stuttgart, Dept. Chem., Stuttgart, Germany, 2000.
- [31] C. Basaran and M. Lin, “Damage mechanics of electromigration induced failure,” *Mech. Mater.*, vol. 40, pp. 66–79, 2008.
- [32] D. Smith, *Thin-Film Deposition: Principles and Practice*. McGraw-Hill Education, 1995.
- [33] B. C. Martin, C. J. Tracy, J. W. Mayer, and L. E. Hendrickson, “A comparative study of hillock formation in aluminum films,” *Thin Solid Films*, vol. 271, no. 1, pp. 64–68, 1995.
- [34] S. Aceto, C. Y. Chang, and R. W. Vook, “Hillock growth on aluminum and aluminum alloy films,” *Thin Solid Films*, vol. 219, no. 1, pp. 80–86, 1992.
- [35] D. S. Herman, M. A. Schuster, and R. M. Gerber, “Hillock Growth on Vacuum Deposited Aluminum Films,” *J. Vac. Sci. Technol.*, vol. 9, no. 1, pp. 515–519, 1972.
- [36] K. Bordo and H. Rubahn, “Effect of Deposition Rate on Structure and Surface Morphology of Thin Evaporated Al Films on Dielectrics and Semiconductors,” *Mater. Sci.*, vol. 18, no. 4, pp. 313–317, 2012.
- [37] T. Onishi, E. Iwamura, K. Takagi, and T. Watanabe, “Effects of Nd content in Al thin films on hillock formation,” *J. Vac. Sci. Technol. A*, vol. 15, no. 4, pp. 2339–2348, Jul. 1997.
- [38] L. W. Barron, “High-Reflectance , Sputter-Deposited Aluminum Alloy Thin Films for Micro-Electro-Mechanical Systems,” M.S. thesis, Dept. Mat. Sci. Eng., Rochester Institute of Technology, Rochester, NY, 2005.
- [39] M. Balasubramanian, *Composite Materials and Processing*. CRC Press, 2013.
- [40] W. O. Soboyejo, T. S. Srivatsan, and J. Lewandowski, *Advanced Structural Materials: Properties, Design Optimization, and Applications.*, CRC Press. 2006.

- [41] N. Chawla and K. K. Chawla, *Metal Matrix Composites*. Springer, New York, 2013.
- [42] L. H. Hihara, R. P. I. Adler, and R. M. Latanision, *Environmental Degradation of Advanced and Traditional Engineering Materials*. Taylor & Francis, 2013.
- [43] G. E. Totten and D. S. MacKenzie, *Handbook of Aluminum: Vol. 1: Physical Metallurgy and Processes*. CRC Press, 2003.
- [44] H. J. McQueen, S. Spigarelli, M. E. Kassner, and E. Evangelista, *Hot Deformation and Processing of Aluminum Alloys*. CRC Press, 2016.
- [45] O. M. Suarez, "Mechanical Properties of a Novel Aluminum Matrix Composite Containing Boron," *J. Mech. Behav. Mater.*, vol. 12, no. 4, pp. 225–238, 2001.
- [46] X. Wang, "The formation of AlB₂ in an Al-B master alloy," *J. Alloys Compd.*, vol. 403, no. April, pp. 283–287, 2005.
- [47] Y. Birol, "Production of Al-B alloy by heating Al/KBF₄ powder blends," *J. Alloys Compd.*, vol. 481, pp. 195–198, 2009.
- [48] I. R. Shein and A. L. Ivanovskii, "Elastic properties of mono- and polycrystalline hexagonal AlB₂-like diborides of s, p and d metals from first-principles calculations," *J. Phys. Condens. Matter*, vol. 20, pp. 1–9, 2008.
- [49] I. Loa, K. Kunc, K. Syassen, P. Bouvier, and T. Alb, "Crystal structure and lattice dynamics of AlB₂ under pressure and implications for MgB₂," *Phys. Rev. B*, vol. 66, pp. 1–8, 2002.
- [50] S. Nafisi and R. Ghomashchi, "Boron-based refiners : Implications in conventional casting of Al – Si alloys," *Mater. Sci. Eng. A*, vol. 453, pp. 445–453, 2007.
- [51] T. K. Adelakin, "An Experimental Study of Aluminum Boride Particles Distribution in Centrifugally Cast Al/AlB_x Composites," M.S. thesis, Dept. Mech. Eng., Univ. Puerto Rico, Mayagüez, PR, 2009.
- [52] Y. H. Duan, Y. Sun, Z. Z. Guo, M. J. Peng, P. X. Zhu, and J. H. He, "Elastic constants of AlB₂ -type compounds from first-principles calculations," *Compos. Part A Appl. Sci. Manuf.*, vol. 51, pp. 112–116, 2012.
- [53] M. Ohring, *Materials Science of Thin Films*. Elsevier Science, 2001.
- [54] G. C. Shwartz, G. C. Schwartz, and K. V Srikrishnan, *Handbook of Semiconductor Interconnection Technology, Second Edition*. CRC Press, 2006.
- [55] A. A. Tracton, *Coatings Technology: Fundamentals, Testing, and Processing Techniques*. CRC Press, 2006.
- [56] A. S. M. I. H. Committee, *ASM Handbook*, no. V.18. ASM International, 1992.
- [57] W. C. Oliver and G. M. Pharr, "An improved technique for determining hardness

- and elastic modulus using load and displacement sensing indentation experiments,” *J. Mater. Res.*, vol. 7, no. 6, pp. 1564–1583, 1992.
- [58] J. Hay, “Introduction to Instrumented Indentation Testing,” *Exp. Tech.*, vol. 33, no. 6, pp. 66–72, 2009.
- [59] W. C. Oliver and G. M. Pharr, “Measurement of hardness and elastic modulus by instrumented indentation: Advances in understanding and refinements to methodology,” *J. Mater. Res.*, vol. 19, no. 1, pp. 3–20, Mar. 2004.
- [60] R. Saha and W. D. Nix, “Effects of the substrate on the determination of thin film mechanical properties by nanoindentation,” *Acta Mater.*, vol. 50, pp. 23–38, 2002.
- [61] S. Chen, L. Liu, and T. Wang, “Size dependent nanoindentation of a soft film on a hard substrate,” *Acta Mater.*, vol. 52, no. 15, pp. 1089–1095, 2004.
- [62] S. M. Han, R. Saha, W. D. Nix, and H. Op, “Determining hardness of thin films in elastically mismatched film-on-substrate systems using nanoindentation,” *Acta Mater.*, vol. 54, pp. 1571–1581, 2006.
- [63] J. Hay and B. Crawford, “Measuring substrate-independent modulus of thin films,” *J. Mater. Res.*, vol. 26, no. 6, pp. 727–738, 2011.
- [64] A. Rar, H. Song, and G. M. Pharr, “Assessment of New Relation for the Elastic Compliance of a Film-Substrate System,” in *Materials Research Society Symposium Proceedings*, 2002, vol. 695, no. 1, pp. 1–6.
- [65] H. Song, “Selected Mechanical Problems Load-Depth-Sensing Indentation Testing,” Ph.D. dissertation, Dept. Mater. Sci., Rice University, Houston, TX, 1999.
- [66] G. Huajian, C. Cheng-Hsin, and L. Jin, “Elastic Contact -Indentation modeling Multi-layer Material,” *Int. J. Solids Struct.*, vol. 29, no. 20, pp. 2471–2492, 1992.
- [67] K. L. Mittal, “Adhesion Measurement of Thin Films,” *Electrocompon. Sci. Technol.*, vol. 3, pp. 21–42, 1976.
- [68] C. Weaver, “Adhesion of thin films,” *J. Vac. Sci. Technol.*, vol. 12, no. 1, pp. 18–25, 1975.
- [69] P. Benjamin and C. Weaver, “The Adhesion of Metals to Crystal Faces,” *Proc. R. Soc. London A*, vol. 274, pp. 267–273, 1963.
- [70] B. Bhushan and X. Li, “Nanomechanical characterisation of solid surfaces and thin films,” *Int. Mater. Rev.*, vol. 48, no. 3, pp. 125–164, Jun. 2003.
- [71] K. M. Dyrda, “Adhesion Characterization of Hard Ceramic Coatings by the Scratch Test,” M.S. thesis, Dept. Phys., Queen’s University at Kingston, Ontario, Canada, 1999.
- [72] B. Bhushan, *Handbook of Micro/Nano Tribology, Second Edition*. Taylor &

Francis, 1998.

- [73] J. L. Hay, R. L. White, B. N. Lucas, and W. C. Oliver, "Scratch Testing and Depth-sensing Indentation," in *MRS Symposium Proceeding*, 1997, vol. 505, pp. 325–330.
- [74] H. Deng, T. W. Scharf, and J. A. Barnard, "Determining Critical Loads for Ultrathin Overcoats Using a Depth Sensing Nanoindentation Multiple Sliding Technique," *IEEE Transactions Magn.*, vol. 33, no. 5, pp. 3151–3153, 1997.
- [75] W. Deguo, Z. Siwei, and G. A. O. Manglai, "Nano-scratch study of molecular deposition (MD) films on silicon wafer using nanoindentation 1," *Sci. China*, vol. 44, pp. 326–329, 2001.
- [76] T. H. Zhang, D. X. Liu, Y. Huan, Y. Y. M, and W. X. L., "Micro/Nanomechanical and Tribological Properties of Thin Diamond-Like Carbon Coatings," *Chinese J. Aeronaut.*, vol. 16, no. 1, pp. 47–51, 2003.
- [77] R. Chang, J. Chen, and C. Sun, "Nanoindentation and Nanoscratch Behaviors of Evaporation Thin Films," in *The 29th National Conference on Theoretical and Applied Mechanics*, 2005, pp. 1–8.
- [78] J. Goddard and H. Wilman, "A theory of friction and wear during the abrasion of metals," *Wear*, vol. 5, no. 2, pp. 114–135, 1962.
- [79] N. P. Suh and H.-C. Sin, "The genesis of friction," *Wear*, vol. 69, no. 1, pp. 91–114, 1981.
- [80] K. Komvopoulos, N. Saka, and N. P. Suh, "Plowing Friction in Dry and Lubricated Metal Sliding," *J. Tribol.*, vol. 108, no. 3, pp. 301–312, Jul. 1986.
- [81] X. Ma, K. Komvopoulos, D. Wan, D. B. Bogy, and Y. Kim, "Effects of film thickness and contact load on nanotribological properties of sputtered amorphous carbon thin films," *Wear*, vol. 254, pp. 1010–1018, 2003.
- [82] P. Larsson and F. Wredenberg, "On indentation and scratching of thin films on hard substrates," *J. Phys. D. Appl. Phys.*, vol. 41, pp. 1–9, 2008.
- [83] S. Lafaye, C. Ñ. Gauthier, and R. Schirrer, "A surface flow line model of a scratching tip : apparent and true local friction coefficients," *Tribol. Int.*, vol. 38, pp. 113–127, 2005.
- [84] C. Gauthier, A. Durier, C. Fond, and R. Schirrer, "Scratching of a coated polymer and mechanical analysis of a scratch resistance solution," *Tribol. Int.*, vol. 39, pp. 88–98, 2006.
- [85] J. Malzbender, J. M. J. Den Toonder, A. R. Balkenende, and G. De With, "Measuring mechanical properties of coatings : a methodology applied to nanoparticle-filled sol-gel coatings on glass," *Mater. Sci. Eng.*, vol. 36, pp. 47–103, 2002.

- [86] K. Komvopoulos, "Sliding Friction Mechanisms of Boundary-Lubricated Layered Surfaces: Part II- Theoretical Analysis," *Tribol. Trans.*, vol. 34, no. 2, pp. 281–291, 1991.
- [87] Z. Liu and R. L. Reuben, "A Numerical Calculation of the Contact Area and Pressure of Real Surfaces in Sliding Wear," *J. Tribol.*, vol. 123, no. January, pp. 27–35, 2001.
- [88] Z. Liu, J. Sun, and W. Shen, "Study of plowing and friction at the surfaces of plastic deformed metals," *Tribol. Int.*, vol. 35, pp. 511–522, 2002.
- [89] P. Benjamin and C. Weaver, "The Adhesion of Metals to Crystal Faces," *Proc. R. Soc. London A*, vol. 274, pp. 267–273, 1963.
- [90] R. G. Bayer, *Mechanical Wear Fundamentals and Testing, Revised and Expanded*. CRC Press, 2004.
- [91] A. S. M. I. H. Committee, *ASM Handbook: Mechanical testing and evaluation*. ASM International, 2000.
- [92] A. C. Fischer-Cripps, *Nanoindentation*. Springer New York, 2013.
- [93] B. D. Cullity and S. R. Stock, *Elements of X-ray Diffraction*. Prentice Hall, 2001.
- [94] Y. Kucuk, "Determination of temperature effect on mechanical properties of templated mesoporous silica aerogels by nanoindentation method," *Int. J. Phys. Sci.*, vol. 6, no. 23, pp. 5369–5375, 2011.
- [95] T. Wang, Z. Chen, H. Fu, J. Xu, Y. Fu, and T. Li, "Grain refining potency of Al-B master alloy on pure aluminum," *Scr. Mater.*, vol. 64, no. 12, pp. 1121–1124, 2011.
- [96] J. Fjellstedt, A. E. W. Jarfors, and L. Svendsen, "Experimental analysis of the intermediary phases AIB₂, AIB₁₂ and TiB₂ in the Al-B and Al-Ti-B systems," *J. Alloys Compd.*, vol. 283, pp. 192–197, 1999.
- [97] W. O. Soboyejo and T. S. Srivatsan, *Advanced Structural Materials: Properties, Design Optimization, and Applications*. CRC Press, 2006.
- [98] A. Loizaga and J. Sertucha, "Defectos metalúrgicos generados por la presencia de gases en el metal fundido," *An. Química*, vol. 2, pp. 111–119, 2008.
- [99] S. N. Aqida, M. I. Ghazali, and J. Hashim, "Effects of porosity on mechanical properties of metal matrix composite: an overview," *J. Teknol.*, vol. 40, pp. 17–32, 2004.
- [100] N. Kurgan, "Effect of porosity and density on the mechanical and microstructural properties of sintered 316L stainless steel implant materials," *Mater. Des.*, vol. 55, pp. 235–241, 2014.
- [101] G. Ramos, O. M. Suarez, and Z. H. Melgarejo, "Fabrication of Functionally graded

- Al-Si Composites reinforced with Boride Particles,” *Sci. Eng. Compos. Mater.*, vol. 17, no. 2, pp. 79–92, 2010.
- [102] R. J. Arsenault and N. Shi, “Dislocation generation due to differences between the coefficients of thermal expansion,” *Mater. Sci. Eng.*, vol. 81, pp. 175–187, 1986.
- [103] N. Ramakrishnan, “An analytical study on strengthening of particulate reinforced metal matrix composites,” *Acta Mater.*, vol. 44, no. 1, pp. 69–77, 1996.
- [104] Y. Watanabe, N. Yamanaka, Y. Oya-Seimiya, and Y. Fukui, “Micro-hardness measurements to evaluate composition gradients in metal-based functionally graded materials,” *Zeitschrift fuer Met.*, vol. 92, no. 1, pp. 53–37, 2001.
- [105] Z. Yuan, F. Li, P. Zhang, B. Chen, and F. Xue, “Mechanical properties study of particles reinforced aluminum matrix composites by micro-indentation experiments,” *Chinese J. Aeronaut.*, vol. 27, no. 2, pp. 397–406, 2014.
- [106] A. Mahato, A. K. Sachdev, and S. K. Biswas, “Effect of particle morphology on resistance to permanent sinking by normal loading of silicon particle in aluminium matrix of a cast aluminium silicon alloy,” *Wear*, vol. 265, pp. 849–855, 2008.
- [107] R. Lacombe, *Adhesion Measurement Methods: Theory and Practice*. CRC Press, 2005.
- [108] D. M. Mattox, *Handbook of Physical Vapor Deposition (PVD) Processing*. Elsevier Science, 2014.
- [109] K. Seshan, *Handbook of Thin Film Deposition: Techniques, Processes, and Technologies*. Elsevier, 2012.
- [110] S. Franssila, *Introduction to Microfabrication*. Wiley, 2005.
- [111] T. T. Soong, *Fundamentals of Probability and Statistics for Engineers*. Wiley, 2004.
- [112] K. Black, *Business Statistics: Contemporary Decision Making*. John Wiley & Sons, 2009.
- [113] S. J. Vachhani, R. D. Doherty, and S. R. Kalidindi, “Effect of the continuous stiffness measurement on the mechanical properties extracted using spherical nanoindentation,” *Acta Mater.*, vol. 61, no. 10, pp. 3744–3751, 2013.
- [114] O. A. Movil-Cabrera, “Thin Film Processing and the Morphological and Mechanical Characterization of Sulfinated Poly (Styrene-isobutylene-styrene) (SIBS),” Ph.D dissertation, Dept. Chem. Eng., Univ. Puerto Rico, Mayagüez, PR, 2013.
- [115] M. A. G. Maneiro and J. Rodríguez, “Pile-up effect on nanoindentation tests with spherical-conical tips,” *Scr. Mater.*, vol. 52, pp. 593–598, 2005.
- [116] S. Chen, L. Liu, and T. Wang, “Investigation of the mechanical properties of thin

- films by nanoindentation, considering the effects of thickness and different coating-substrate combinations,” *Surf. Coat. Technol.*, vol. 191, pp. 25–32, 2005.
- [117] K.-H. Jang, S.-J. Hwang, and Y.-C. Joo, “Effect of capping layer on hillock formation in thin Al films,” *Met. Mater. Int.*, vol. 14, no. 2, pp. 147–150, 2008.
- [118] S. Hwang, J. Lee, C. Jeong, and Y. Joo, “Effect of film thickness and annealing temperature on hillock distributions in pure Al films,” *Scr. Mater.*, vol. 56, pp. 17–20, 2007.
- [119] D. Kim, B. Heiland, W. D. Nix, E. Arzt, M. D. Deal, and J. D. Plummer, “Microstructure of thermal hillocks on blanket Al thin films,” *Thin Solid Films*, pp. 278–282, 2000.
- [120] T. Onishi, E. Iwamura, and K. Takagi, “Morphology of sputter deposited Al alloy films,” *Thin Solid Films*, vol. 340, pp. 306–316, 1999.
- [121] Agilent Technologies, “Scratch Testing of Low-k Dielectric Films and a Correlation Study of the Results.” Agilent Technologies Inc., Application note, pp. 1–8, 2010.
- [122] G. Wei, M. L. Weaver, and J. A. Barnard, “Nanotribological Studies of Chromium Thin Films,” *Tribol. Lett.*, vol. 13, no. 4, pp. 255–261, 2002.
- [123] S. Trinkle and M. Al-haik, “Tribological reliability of MEMS multilayered thin films,” *Int. J. Materials Struct. Integr.*, vol. 3, no. 2–3, pp. 201–216, 2009.
- [124] Y. W. Bao, W. Wang, and Y. C. Zhou, “Investigation of the relationship between elastic modulus and hardness based on depth-sensing indentation measurements,” *Acta Mater.*, vol. 52, pp. 5397–5404, 2004.
- [125] Y. Chen, S. R. Bakshi, and A. Agarwal, “Surface & Coatings Technology Correlation between nanoindentation and nanoscratch properties of carbon nanotube reinforced aluminum composite coatings,” *Surf. Coat. Technol.*, vol. 204, no. 16–17, pp. 2709–2715, 2010.
- [126] W. Tang, X. Weng, L. Deng, K. Xu, and J. Lu, “Nano-scratch experiments of Au/NiCr multi-layered films for microwave integrated circuits,” *Surf. Coat. Technol.*, vol. 201, pp. 5664–5666, 2007.
- [127] R. C. Chang, F. Y. Chen, and C. E. Sun, “Using Nanoindentation and Nanoscratch to Determine Thin Film Mechanical Properties,” *Key Eng. Mater.*, vol. 326–328, pp. 357–360, 2006.
- [128] T. H. Zhang and Y. Huan, “Substrate Effects on the Micro/Nanomechanical Properties of TiN Coatings,” *Tribol. Lett.*, vol. 17, no. 4, pp. 911–916, 2004.
- [129] C. Y. Huang, C. H. Hsieh, J. J. J. Wang, and C. T. Hsu, “Investigation of Scratching Nano Grooves on Aluminum Film,” in *IEEE 3rd International Conference on Nano/Molecular Medicine and Engineering*, 2009, pp. 146–149.

- [130] P. J. Blau, Ed., *ASM Handbook: Friction, Lubrication and Wear Technology*. ASM International, 1992.
- [131] S. R. Bakshi, D. Lahiri, R. R. Patel, and A. Agarwal, "Nanoscratch behavior of carbon nanotube reinforced aluminum coatings," *Thin Solid Films*, vol. 518, no. 6, pp. 1703–1711, 2010.
- [132] S. R. Bakshi, A. K. Keshri, and A. Agarwal, "A comparison of mechanical and wear properties of plasma sprayed carbon nanotube reinforced aluminum composites at nano and macro scale," *Mater. Sci. Eng. A*, vol. 528, no. 9, pp. 3375–3384, 2011.
- [133] R. Carrasquillo, R. Rivera, Y. Martínez, and O. M. Suárez, "Tribological Comparative Study of the Effect of Boride and Silicon Particles on Aluminum Matrix Composites," *Sci. Eng. Compos. Mater.*, vol. 16, no. 4, pp. 259–266, 2009.
- [134] T. Onishi *et al.*, "Effects of Nd content in Al thin films on hillock formation," *J. Vac. Sci. Technol. A*, vol. 15, no. 4, pp. 2339–2348, 1997.
- [135] G. Ramos-Rivera, "Fabrication, Characterization and Testing of Functionally Graded Aluminum-based Targets for Sputtering Deposition of Hybrid Composites," M.S. thesis, Dept. Mech. Eng., Univ. Puerto Rico, Mayagüez, PR, 2011.
- [136] H. Onoda *et al.*, "Effects of insulator surface roughness on Al-alloy film properties and electromigration performance in Al-alloy/Ti insulator layered interconnects," *J. Vac. Sci. Technol. B*, vol. 14, no. 4, pp. 2645–2655, 1996.
- [137] C. Ottone, M. Laurenti, K. Bejtka, A. Sanginario, and V. Cauda, "The Effects of the Film Thickness and Roughness in the Anodization Process of Very Thin Aluminum Films," *Journals Mater. Sci. Nanotechnol.*, vol. 1, no. 1, pp. 1–9, 2014.
- [138] T. Ishiguro and K. Miyamura, "Controllability of Mesoscopic Surface Roughness of Sputtered Al and Al-N Films," *Mater. Trans.*, vol. 46, no. 12, pp. 3037–3043, 2005.
- [139] D. Aurongzeb, E. Washington, M. Basavaraj, J. M. Berg, H. Temkin, and M. Holtz, "Nanoscale surface roughening in ultrathin aluminum films," *Appl. Phys.*, vol. 100, no. 11, pp. 11–14, 2006.
- [140] T. J. Kang *et al.*, "Modification of optical and mechanical surface properties of sputter-deposited aluminum thin films through ion implantation," *Int. J. Precis. Eng. Manuf.*, vol. 15, no. 5, pp. 889–894, 2014.
- [141] D. C. Montgomery and G. C. Runger, *Applied Statistics and Probability for Engineers*. John Wiley & Sons, 2005.
- [142] A. Paul and J. Wingbermu, "Surface morphology for ion-beam sputtered Al layer with varying sputtering conditions," *Appl. Surf. Sci.*, vol. 252, pp. 8151–8155, 2006.

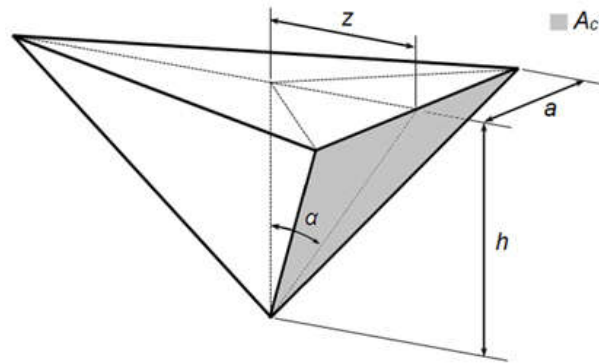
- [143] M.-T. Le, Y.-U. Sohn, J.-W. Lim, and G.-S. Choi, "Effect of Sputtering Power on the Nucleation and Growth of Cu Films Deposited by Magnetron Sputtering," *Mater. Trans.*, vol. 51, no. 1, pp. 116–120, 2010.
- [144] Z. Zhang, C. Bao, S. Ma, L. Zhang, and S. Hou, "Effects of deposition power and pressure on the crystallinity of Al-doped ZnO thin films at glass substrates by low temperature RF magnetron sputtering," *J. Aust. Ceram. Soc.*, vol. 48, no. 2, pp. 214–222, 2012.
- [145] J. Venables, G. Spiller, and M. Hanbucken, "Nucleation and growth of thin films," *Reports Prog. Physic*, vol. 47, pp. 399–459, 1984.
- [146] C. Kylner and L. Mattsson, "Enhanced optical performance of aluminum films by copper inclusion," *Thin Solid Films*, vol. 348, pp. 222–226, 1999.
- [147] M. Draissia, H. Boudemagh, and M. Y. Debili, "Structure and Hardness of the Sputtered Al-Cu Thin Films System," *Phys. Scr.*, vol. 69, pp. 348–350, 2004.
- [148] C. V. Thompson and R. Carel, "Texture development in polycrystalline thin films," *Mater. Sci. Eng. B*, vol. 32, no. 3, pp. 211–219, 1995.
- [149] A. Chaoumead, Y. Sung, and D. Kwak, "The Effects of RF Sputtering Power and Gas Pressure on Structural and Electrical Properties of ITiO Thin Film," *Adv. Condens. Matte Phys.*, vol. 2012, no. 4, p. 7, 2012.
- [150] G. Ramos and O. M. Suárez, "Characterization of sputtered Al-B-Si thin films produced with composite targets for device applications," *Sci. Eng. Compos. Mater.*, vol. 19, pp. 93–99, 2012.
- [151] L. W. Barron, J. Neidrich, and S. K. Kurinec, "Optical , electrical , and structural properties of sputtered aluminum alloy thin films with copper , titanium and chromium additions," *Thin Solid Films*, vol. 515, pp. 3363–3372, 2007.
- [152] P. Waters, "Stress analysis and mechanical characterization of thin films for microelectronics and MEMS applications by," Ph.D. dissertation, Dept. Mech. Eng., Univ. South Florida, FL, 2008.
- [153] A. A. Volinsky, N. R. Moody, and W. W. Gerberich, "Nanoindentation of Au and Pt/Cu thin films at elevated temperatures," *J. Mater. Res.*, vol. 19, no. 9, pp. 2650–2657, 2004.
- [154] M. Rathinam, R. Thillaigovindan, and P. Paramasivam, "Nanoindentation of aluminum (100) at various temperatures," *J. Mech. Sci. Technol.*, vol. 23, pp. 2652–2657, 2009.
- [155] B. D. Beake and J. F. Smith, "High-temperature nanoindentation testing of fused silica and other materials," *Philos. Mag.*, vol. 82, no. 10, pp. 2179–2186, 2002.
- [156] J. F. Smith and S. Zheng, "High temperature nanoscale mechanical property measurements," *Surf. Eng.*, vol. 16, no. 2, pp. 143–146, 2000.

- [157] Kwak, Dong-joo, B.-W. Park, Y.-M. Sung, and M.-W. Park, "Effects of Gas Pressure and Discharge Power on Electrical and Optical Properties of ZnO: Al Thin Film Deposited on Polymer Substrate," *J. Plasma Fusion Res.*, vol. 8, pp. 1427–1430, 2009.
- [158] X.-C. Chen, J.-P. Zhou, and W. Hau-Yang, "In situ high temperature X-ray diffraction studies of ZnO thin film," *Chinese Phys. B*, vol. 20, no. 9, pp. 1–3, 2011.
- [159] J. Wang, J. Wang, A. Li, J. Li, and Y. Zhou, "Theoretical Study on the Mechanism of Anisotropic Thermal Properties of Ti₂AlC and Cr₂AlC," *J. Am. Ceram. Soc.*, vol. 94, no. 4, pp. 1202–1208, 2014.
- [160] A. Moridi, H. Ruan, L. C. Zhang, and M. Liu, "Residual stresses in thin film systems: Effects of lattice mismatch, thermal mismatch and interface dislocations," *Int. J. Solids Struct.*, vol. 50, no. 22–23, pp. 3562–3569, 2013.
- [161] T. Matsue, T. Hanabusa, K. Kusaka, and O. Sakata, "Relaxation of Residual Stresses in Thin Films Investigated Using Synchrotron Radiation," in *The 58th Annual Denver X-ray Conference (DXC)*, 2009, pp. 233–239.

APPENDIX A

Scratch contact area (A_c)-Berkovich tip indenter

$$A_c = a \cdot H$$



height of A_c triangle is:

$$H = \frac{h}{\cos \alpha}$$

$$a = \frac{z}{\tan 30^\circ} = \sqrt{3} \cdot z$$

$$z = h \cdot \tan \alpha$$

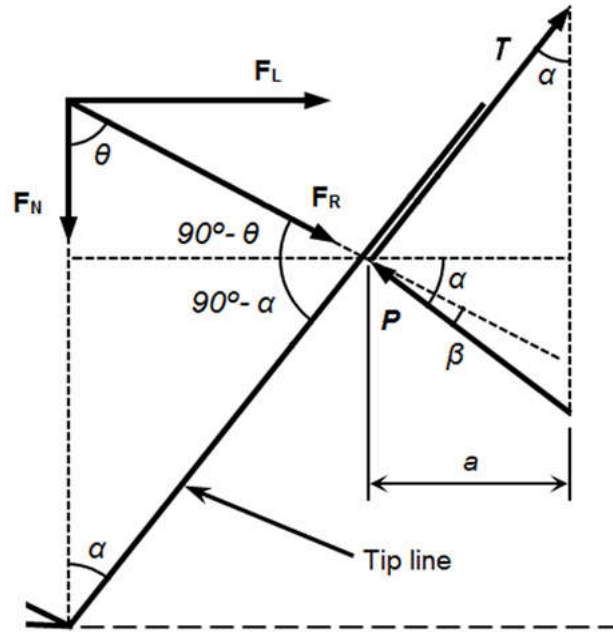
$$a = \sqrt{3} \cdot h \cdot \tan \alpha$$

Finally:

$$A_c = \frac{\sqrt{3} \cdot h^2 \cdot \tan \alpha}{\cos \alpha} \quad (\text{A - 1})$$

APPENDIX B

Solution 1: Analysis for adhesion strength formulation



$$\beta = \alpha + \theta - 90^\circ \quad \therefore \quad \theta = \arctan\left(\frac{F_L}{F_N}\right)$$

Resultant force:

$$F_R = \sqrt{F_L^2 + F_N^2} \quad (\text{B-1})$$

Reaction force is perpendicular to tip line:

$$R = F_R \cdot \cos\beta \quad (\text{B-2})$$

In terms of stress, using the contact area (equation A-1):

$$P = \frac{R}{A_c} = \frac{F_R \cdot \cos \beta}{\sqrt{3} \cdot h^2 \cdot \tan \alpha} = \frac{\sqrt{3} \cdot F_R \cdot \cos \beta \cdot \cos \alpha}{3 \cdot h^2 \cdot \tan \alpha}$$

$$P = \frac{\sqrt{3} \cdot F_R \cdot \cos \beta \cdot \cos \alpha}{3 \cdot h^2 \cdot \tan \alpha}$$

Now, for the adhesion strength (τ):

$$\sin \alpha = \frac{a}{\tau} \Rightarrow a = \tau \cdot \sin \alpha$$

$$\cos \alpha = \frac{a}{P} \Rightarrow a = P \cdot \cos \alpha$$

Equating for a : $\tau \cdot \sin \alpha = P \cdot \cos \alpha$

$$\tau = \frac{P \cdot \cos \alpha}{\sin \alpha} = \frac{P}{\tan \alpha}$$

Replacing the value of P in this expression:

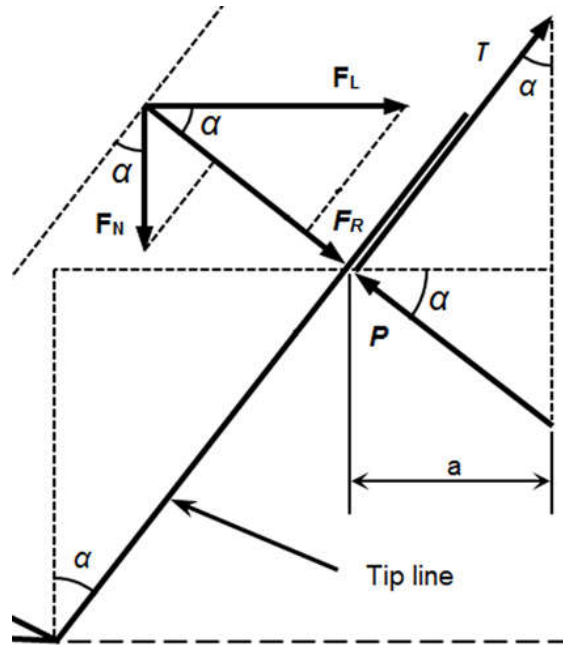
$$\tau = \frac{\frac{\sqrt{3} \cdot F_R \cdot \cos \beta \cdot \cos \alpha}{3 \cdot h^2 \cdot \tan \alpha}}{\tan \alpha}$$

Finally:

$$\tau = \frac{\sqrt{3} \cdot F_R \cdot \cos \beta \cdot \cos \alpha}{3 \cdot h^2 \cdot \tan^2 \alpha}$$

APPENDIX C

Solution 2: Analysis for adhesion strength formulation



Resultant force:

$$F_R = F_L \cdot \cos \alpha + F_N \cdot \sin \alpha$$

For action-reaction:

$$R = F_R$$

In terms of stress, using the contact area (equation A-1):

$$P = \frac{R}{A_c} = \frac{F_L \cdot \cos \alpha + F_N \cdot \sin \alpha}{\frac{\sqrt{3} \cdot h^2 \cdot \tan \alpha}{\cos \alpha}}$$

$$P = \frac{\sqrt{3} \cdot (F_T \cdot \cos \alpha + F_N \cdot \sin \alpha) \cdot \cos \alpha}{3 \cdot h^2 \cdot \tan \alpha}$$

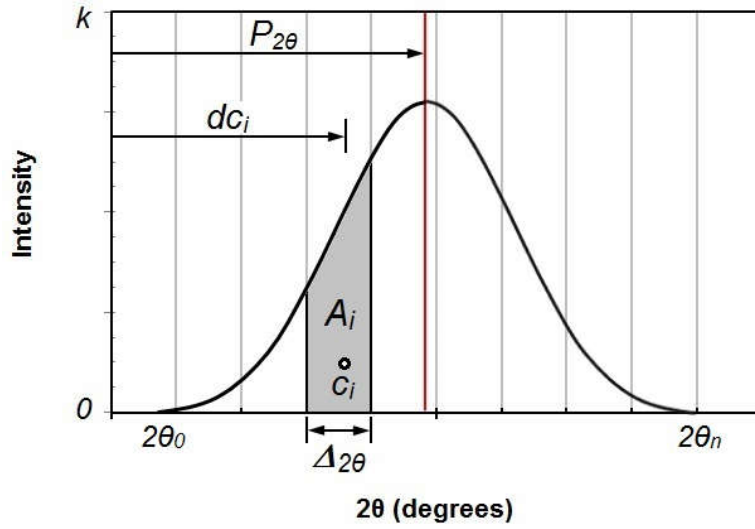
Replacing the value of P in this expression of equation B-4:

$$T = \frac{\frac{\sqrt{3} \cdot (F_T \cdot \cos \alpha + F_N \cdot \sin \alpha) \cdot \cos \alpha}{3 \cdot h^2 \cdot \tan \alpha}}{\tan \alpha}$$

$$T = \frac{\sqrt{3} \cdot (F_T \cdot \cos \alpha + F_N \cdot \sin \alpha) \cdot \cos \alpha}{3 \cdot h^2 \cdot \tan^2 \alpha}$$

APPENDIX D

Calculation peak position from centroid method of the peak



$$P_{2\theta} = \frac{\sum_{i=1}^n A_i \cdot dc_i}{\sum_{i=1}^n A_i}$$

where $P_{2\theta}$ is the value of peak position distance in degrees, A_i is of section area and , dc_i is the centroid distance in degrees, for the i point. The A_i is the parallelogram area.